5-2012

A High-Energy Neutron Flux Spectra Measurement Method for the Spallation Neutron Source

Nicholas Patrick Luciano
nluciano@utk.edu

To the Graduate Council:

I am submitting herewith a thesis written by Nicholas Patrick Luciano entitled "A High-Energy Neutron Flux Spectra Measurement Method for the Spallation Neutron Source." I have examined the final electronic copy of this thesis for form and content and recommend that it be accepted in partial fulfillment of the requirements for the degree of Master of Science, with a major in Nuclear Engineering.

<div align="right">Lawrence F. Miller, Major Professor</div>

We have read this thesis and recommend its acceptance:

Erik B. Iverson, Ronald E. Pevey

<div align="right">Accepted for the Council:</div>

<div align="right"><u>Carolyn R. Hodges</u></div>

<div align="right">Vice Provost and Dean of the Graduate School</div>

(Original signatures are on file with official student records.)

A High-Energy Neutron Flux Spectra Measurement Method for the Spallation Neutron Source

A Thesis Presented for the

Master of Science

Degree

The University of Tennessee, Knoxville

Nicholas Patrick Luciano

May 2012

Dedication

What we call the beginning is often the end
And to make an end is to make a beginning.
The end is where we start from...

We shall not cease from exploration
And the end of all our exploring
Will be to arrive where we started
And know the place for the first time.

–T.S. Eliot, *Little Gidding*

Acknowledgments

This work would not have been possible without the support of many. I must thank Dr. Erik Iverson, my advisor and mentor, for dedicating innumerable hours to my education. Erik, I will consider myself quite accomplished if someday I possess even a fraction of your knowledge, experience, and skill. Also, I would like to thank my committee members Dr. Larry Miller and Dr. Ron Pevey, who both have taught me much.

The staff members of the Spallation Neutron Source are too many to name, but I will try to list a few: the neutronics group - Phil Ferguson, Franz Gallmeier, Wei Lu, Ceris Hamilton, and Wendy Brooks; the beamline staff - Doug Abernathy, Matt Stone, Ashfia Huq, and Jason Hodges; David Freeman; Pedro Gonzalez, David Craft, Jim Treen, and the RCTs; the instrument support staff - especially David Dunning, Ray Wilson, and Jack Frye; George Dodson, Larry Longcoy, and the accelerator operations staff. To those that I've neglected to list here, you have my apologies and my sincere thanks.

Mom, Dad, Jessi, and Dustin are the constants in my life that enable me to explore the variables. I can only offer you my love and thanks in return.

Finally, to my fiancée Jennifer Niedziela, words cannot express how much I appreciate you. You are my best friend... and while doing this work, it was especially nice to have a best friend who knew a little something about neutrons. Thank you, I love you, and I'm looking forward to our life together.

Abstract

The goal of this work was to develop a foil activation method to measure high-energy (1–120 MeV) neutron flux spectra at the Spallation Neutron Source by researching the scientific literature, assembling an experimental apparatus, performing experiments, analyzing the results, and refining the technique based on experience. The primary motivation for this work is to provide a benchmark for the neutron source term used in target station and shielding simulations

Two sets of foil irradiations were performed, one at the ARCS beamline and one at the POWGEN beamline. The gamma radiation of the foil activation products was measured with a high purity germanium gamma-ray spectrometer, and the product reaction rates during irradiation were quantified. Corrections, such as self-shielding factors, were applied to the measurements to account for particular effects. The corrected measurement data, along with calculated response functions and an initial guess spectrum, were input to the MAXED neutron spectrum unfolding computer code. MAXED uses the maximum entropy method to unfold an output spectrum that is the minimally modified guess spectrum consistent with the measurement data.

The foil irradiation and subsequent analysis from the ARCS spectrum produced a reasonable neutron spectrum, which noticeably differed from the initial guess spectrum. This measurement is regarded as consistent, but yet unverified. The gamma-ray spectrum of the foil irradiation at the POWGEN beamline showed no high-energy activation. This is regarded as an experimental error, and no conclusions can be drawn about the high-energy neutron spectrum. Future foil irradiations are planned to verify and expand the neutron spectrum measurements.

Contents

List of Tables

List of Figures

xi

List of Abbreviations

ASCII American Standard Code for Information Interchange

ASTM American Society for Testing and Materials International

ARCS (Wide) Angular-Range Chopper Spectrometer

CDF cumulative distribution function

DIM Detector Interface Module

EAF European Activation File

ENDF Evaluated Nuclear Data File

FWHM full-width half-max

HPGe High Purity Germanium

HV high voltage

IQU Integral Quantities Utility

JENDL Japanese Evaluated Nuclear Data Library

LN2 liquid nitrogen

MCA Multi-Chanel Analyzer

MCNPX Monte Carlo N-Particle eXtended

ORNL Oak Ridge National Laboratory

RSE Relative Standard Error

SA Simulated Annealing

SAC Sample Activation Calculator

SciPy Scientific Python

SNS Spallation Neutron Source

TENDL TALYS-based Evaluated Nuclear Data Library

TCS True Coincidence Summing

UMG Unfolding with Maxed and Gravel

Chapter 1

Introduction

1.1 Foundational Concepts

The Spallation Neutron Source (SNS) at Oak Ridge National Laboratory (ORNL) produces neutron beams for scientific use. The SNS is an accelerator-driven neutron source that directs an intense high-energy proton beam into a liquid mercury target to produce spallation neutrons. The neutrons pass through cryogenic or ambient temperature moderators and then down one of twenty-four beam transport lines to an instrument area. Materials placed in the sample position of an instrument scatter the incident neutrons into a surrounding detector array. Currently, the SNS has 14 such instruments in operation with 5 more under construction and several more planned. Each neutron instrument has been designed using a unique combination of beamline components and detectors to measure various material properties by collecting data from the scattered neutrons. Neutrons in the cold and thermal energy regimes ($\sim$1 meV–2 eV) are the most useful to the scattering experiments, but higher energy neutrons (up to $\sim$1 GeV) are also present in the beams. Neutrons in several energy ranges, including thermal and high-energy, can be measured through foil activation techniques.

Foil activation techniques involve the insertion of material probes into a neutron radiation field for the purpose of characterizing the radiation's energy distribution (spectrum) or intensity. Neutrons interact with the foil causing its constituent nuclei to undergo nuclear transmutations producing product nuclides. Some of these newly created

products will be unstable against nuclear decay and spontaneously disintegrate over time, often producing gamma radiation. The number of product nuclei is a function of the foil's propensity for a nuclear reaction (reaction cross section) and the speed-weighted energy distribution of the incident neutron radiation (neutron scalar flux spectrum). If the reaction cross section and foil composition are well characterized, and the number of product nuclei are measured, unknown properties of the incident neutron flux can be deduced.

Both the reaction cross section and the neutron energy spectrum are functions of the incident neutron energy. Unless the reaction cross section exhibits an unambiguous energy feature like a precipitous decrease or increase in magnitude at some energy, the energy dependence of the neutron flux cannot be extracted from the measurement. To reveal the energy dependence of the flux, several foils of differing material can be used, each foil having one or more reactions with distinct responses over ranges of energies. This is the multiple foil activation technique, and it uses threshold reactions, those with a zero cross section value below a threshold energy, to accomplish the required energy discrimination.

To measure the quantity of radionuclides produced in the foil, the decay gamma radiation can be used. Gamma radiation can carry away the energy due to a nucleus's transition between discrete nuclear energy levels during the decay process. The structure of the nuclear levels is typically complex, but it is also unique to each nuclide. The relative proportion of the discrete energies of the gamma-rays is contained in the gamma-ray spectrum, and measured spectrometric data have long been catalogued along with their parent nuclides. Using this catalogued data, a measured gamma-ray spectrum acts as a signature that identifies the decaying nuclide in an activated foil. While the exact energies and relative abundance of the resulting gamma-rays identify the decaying nuclide, the total gamma-ray intensity quantifies the number of decays present in an activated foil during a particular time interval.

The energy and intensity of gamma radiation is measured with a gamma-ray spectrometer. While several varieties exist, the HPGe gamma-ray spectrometer is the standard instrument due to its high energy resolution. When a gamma-ray interacts with the atoms in the spectrometer's single crystal of germanium, it transfers some or all of its energy to the atomic electrons via one of several possible physical mechanisms. The

spectrometer records the number of displaced electrons and holes due to the incident gamma radiation during a brief (μs) time interval. The number of displaced electrons and holes produced is proportional to the total energy imparted by the incident gamma photon. If all of the gamma photon's energy is deposited in the germanium, the number of displaced holes and electrons is proportional to the total energy of the incident gamma photon.

The activity is defined as the magnitude of the nuclear decay rate. For gamma-ray emitting decays, the activity is proportional to the rate of gamma radiation emission. While measuring a single gamma-ray's energy may only require a single event in the spectrometer, activity measurements require measuring many gamma-rays over a time interval. Because the process of radioactive decay is a random occurrence, measuring more gamma-rays over a longer period of time reduces the statistical uncertainty associated with the activity measurement.

Once the activity due to a particular product nuclide has been measured, the neutron flux spectrum that induced the activity remains to be determined. Given the foils' material properties, if the neutron flux spectrum is known, the resulting activity can be computed easily. The converse situation, computing the neutron flux spectrum from the resulting activity given the foils' material properties, is more difficult. Generally, when a model and its output are known, but the model input is unknown, the problem is called an *inverse problem*. To determine the neutron flux spectrum from foil activity measurements is to an solve inverse problem through a process known as *unfolding*. Mathematically, unfolding is deconvolution, the process of distinguishing the contributing components of a combined function.

Because a finite number of measurements are used in the unfolding, a continuous neutron flux spectrum cannot be determined, rather the flux spectrum consists of group flux values over many discrete energy groups. Factors influencing the selection of energy group structure may include the expected behavior of the flux over the entire energy range and the energy detail required in a subsequent calculation. Often these issues dictate that the number of energy groups exceeds the number of activity measurements used to determine the group flux values. When this occurs, solving for the neutron flux is an underdetermined inverse problem which cannot be computed by direct calculation. A specialized iterative algorithm can be employed to find a solution flux spectrum that is consistent with the foil

activity measurements.

By irradiating multiple foils at the SNS instruments, measuring their induced gamma-ray activity, and then using computational unfolding methods, the high-energy neutron flux spectra at the SNS can be measured.

1.2 Purpose

The purpose of this work has been to develop a foil activation method to measure the high-energy (1–120 MeV) neutron flux spectra at the SNS. This method has been developed by researching the scientific literature, assembling experimental apparatus, performing measurements, analyzing their results, and refining the technique based on experience. Measuring the high-energy neutron flux spectrum provides further empirical data to validate the SNS shielding design and sample activation calculations.

Consideration of the high-energy neutrons was an important component of the beamline and target monolith shielding design at the SNS. The SNS currently produces neutrons with energies to nearly 1 GeV, and after future upgrades, may produce neutrons with energies to nearly 1.4 GeV. An abundance of data exist for shielding neutrons in the energy range typical of reactors, but considerably less data exist beyond this range. High-energy neutrons produced at the SNS have a much greater penetrating power and require regular concrete[1] shielding up to 2 m thick [1]. For high-energy neutron transport, the SNS shielding design employed nuclear collision models and multigroup transport libraries derived from nuclear collision models [2]. Nuclear models are less accurate than evaluated cross section data, but relatively few evaluated data exist above 20 MeV. Therefore, standard cross section libraries such as Evaluated Nuclear Data File (ENDF)/B mostly rely on nuclear models above 20 MeV [3]. Because the SNS produces neutrons in this unconventional energy regime, and because radiation shielding is essential for personnel protection, the shielding design required validation with measurements. Many safety and operational measurements were completed during SNS commissioning in 2006, but until this work, neutrons in the high-energy range had not yet been measured.

Characterizing the large number of activated user samples at the SNS provides

---

[1]The shielding implemented at SNS includes both regular and high-density concrete.

another motivation for measuring the high-energy flux spectra. Accurate measurements of post-irradiated samples is difficult and time consuming, so prior to irradiation, SNS staff estimate the expected dose rate and isotopic inventory of each sample by using the Sample Activation Calculator (SAC) developed at the SNS [4]. Should the activated user samples exceed administrative dose-rate or isotope levels, the samples may be retained at the facility indefinitely or until the activity has decayed below release levels. Measurement of the high-energy neutron flux spectra will provide validated flux spectra, and the foil activity measurements serve as an empirical benchmark for the activation code's estimates. Improved sample activation estimates will reduce the number of samples conservatively retained on site, allowing users greater flexibility and reducing the sample stewardship burden to the facility.

Finally, high-energy neutron flux spectra measurements may serve some yet unanticipated purpose. The measurements could serve a diagnostic purpose for beamlines or be incorporated into future beamline shielding models. The utility of these measurements are likely to broaden once they become routinely available. But before they can be used for any of these purposes, a method of measurement must be developed. Developing that method has been the goal of this work.

Chapter 2

Theory

This chapter describes the necessary theoretical foundation for developing a method of high-energy neutron flux spectrum measurement at the Spallation Neutron Source (SNS).

2.1 Spallation Neutron Production and Transport

Neutrons can be produced by several means including nuclear reactors, (α,n) sources, and radioactive isotopes (*e.g.* ^{252}Cf). The SNS generates neutrons through a different mechanism than these sources. Nuclear spallation is analogous to the eponymous mechanical spallation process, the ejection of fragments from a object when impacted by another object.

Nuclear spallation occurs when energetic (> 100 MeV) subatomic particles (protons, neutrons, pions, *etc.*) collide with a nucleus to eject subatomic particles. At neutron scattering facilities, spallation is designed to occur within a material target. Unlike (n,xn) reactions, spallation reactions are not considered to form an intermediate compound nucleus. The high energies of the projectile particles means their de Broglie wavelength is short enough to interact with individual nucleons inside the nucleus. The projectile particle undergoes a series of direct reactions with the nucleons to create an "intranuclear cascade" whereby several nucleons may be ejected and the nucleus is left in an energetically excited state. The primary projectile and the secondary spallation particles may have enough kinetic energy to induce further spallation reactions in other nuclei. The
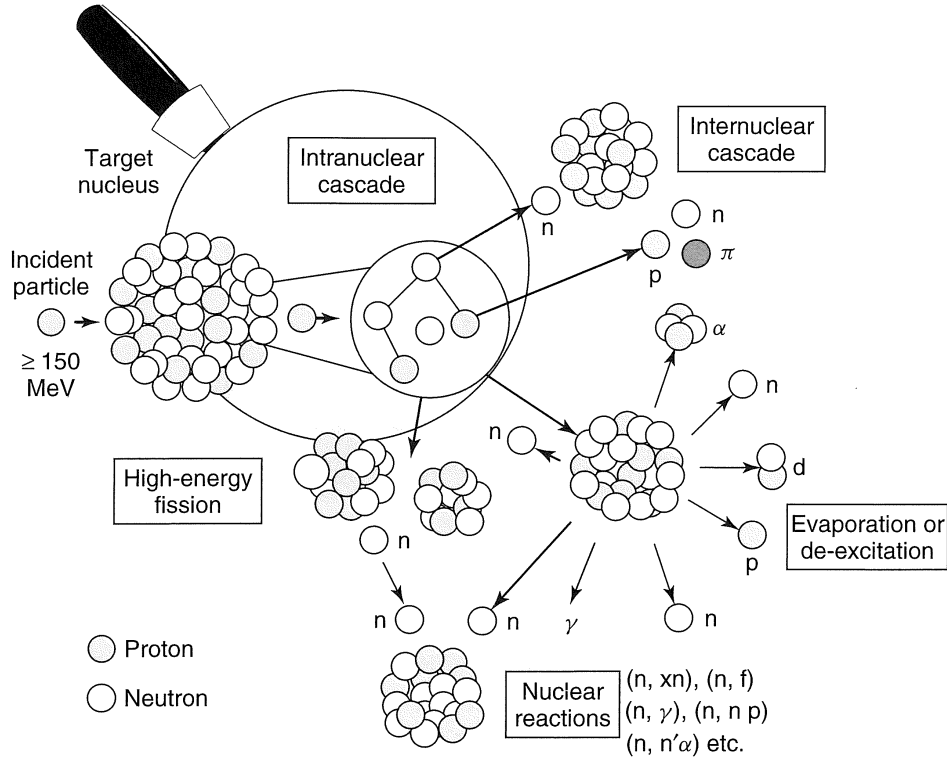
Figure 2.1: Illustration of the spallation process showing the intranuclear cascade followed by evaporation and high-energy fission of highly excited nuclei [6].

highly-excited nucleus relaxes to its ground state by subsequently "evaporating" nucleons, primarily neutrons. In heavy nuclei such as tantalum, tungsten, and lead, high-energy fission also competes with nuclear evaporation in the excited nucleus [5] (Figure 2.1).

The spallation and evaporation neutrons created during and after the collision span the range of energies up to nearly[1] the incident particle energy (Figure 2.2). Before most of these neutrons can be useful to neutron scattering experiments, they must be cooled to cold and thermal neutron energies. This is accomplished with a dedicated moderator, typically composed of hydrogenous material, which reduces the mean neutron energy through scattering collisions. An ideal gas of neutrons at thermal equilibrium have a Maxwellian distribution of energies E

$$M(E) = \frac{2\pi}{(\pi kT)^{3/2}}\sqrt{E}e^{-\frac{E}{kT}} \tag{2.1}$$

---

[1]The nuclear binding energy is typically a small fraction of the incident particle energy.
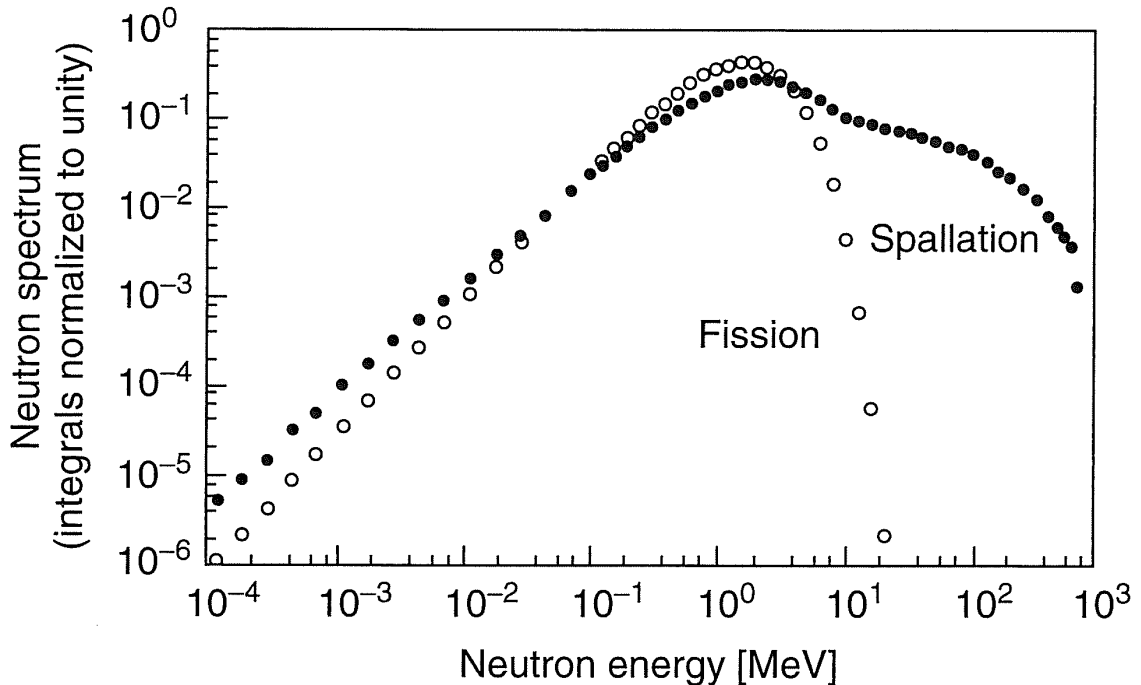
Figure 2.2: Calculated spallation neutron spectrum (before moderation) from a tungsten target bombarded by 800 MeV protons compared to a typical neutron spectrum from thermal neutron fission of ^{235}U. Note the spallation spectrum extends up to nearly the incident particle energy [6].

at temperatures T, where k is the Boltzmann constant. Although neutrons transiting the moderator will not be precisely in thermal equilibrium, a Maxwellian distribution of energies is usually a reasonable approximation for neutron energies near kT, where T is the moderator temperature. Neutrons leaving the target and the moderator travel in a distribution of directions. Neutronically reflecting material may surround the target to increase the probability that errant neutrons will enter the moderator. Liners, decouplers, and other forms of neutron poisons also may be used to alter the time and energy characteristics of neutrons used in scattering experiments.

Once neutrons have been quasi-thermalized in the moderator, they propagate through surrounding material such as shielding. The neutron beamlines are essentially pathways in the shielding through which neutrons can travel virtually unimpeded. Most beamlines at scattering facilities make use of supermirror neutron guides. These guides propagate wavelike low-energy neutrons with small incident scattering angles by reflec-

tion. Neutron guides can increase the low-energy neutron flux delivered to the end of the transport line by a few orders of magnitude. Higher energy neutrons are unaffected by neutron guides, so slightly curving a guide along a beamline filters the high-energy component. Unguided neutron flux decreases over the length of the beamline with the typical $1/r^2$ relationship, where r is the distance from a point source. Because this work is concerned with high-energy neutrons, guide propagation of low-energy neutrons will be of little consequence, but the mechanism is mentioned here for completeness.

The transport of non-wavelike neutrons in non-multiplying media with a time-independent external source q_{ext} is described by this form of the Boltzmann neutron transport equation:

$$
\left(\hat{\Omega} \cdot \vec{\nabla} + \Sigma_t(\vec{r}, E)\right) \psi(\vec{r}, \hat{\Omega}, E) = q_{\text{ext}}(\vec{r}, \hat{\Omega}, E)
$$
$$
+ \int_0^\infty dE' \int_{4\pi} d\Omega' \Sigma_s(\vec{r}, \hat{\Omega}' \cdot \hat{\Omega}, E' \to E)\psi(\vec{r}, \hat{\Omega}, E) \quad (2.2)
$$

where $\psi(\vec{r}, \hat{\Omega}, E)$ is the angular flux at position $\vec{r}$ traveling in direction $\hat{\Omega}$ of energy E, Σ_t is the macroscopic total cross section, and Σ_s is the macroscopic scattering cross section from direction Ω' to Ω and from energy E' to E. The spallation process of neutron production will be considered an external source, and the materials used are non-multiplying, so equation 2.2 is sufficient to describe most neutron transport in this work.

2.2 Foils

2.2.1 Multiple Foil Activation Technique

Foil activation can be used as a measurement of neutron flux and flux spectra over a wide range of energies. Some materials exhibit large reaction cross sections in the thermal energy range (*e.g.* ^{197}Au(n,γ)^{198}Au), and others have large reaction cross section resonance peaks in the epithermal range (*e.g.* ^{115}In(n,γ)$^{116\text{m}}$In). Reactions of these types have cross section values typically ranging from 10–10^4 b. The energy features of these reaction cross sections allow the reaction products to be mostly attributed to neutrons in those energy ranges. Thus, measurement of the reaction products in the foils can be related to the neutron flux in these energy ranges.
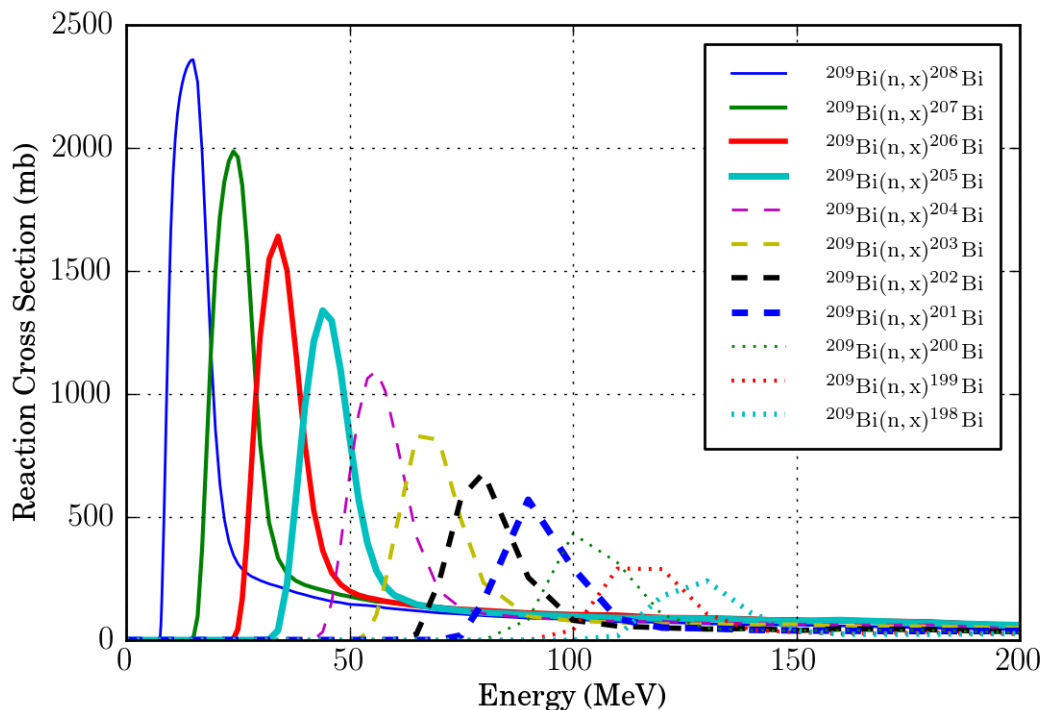
Figure 2.3: Reaction cross sections for several ^{209}Bi(n,xn) threshold reactions. See Appendix D for additional threshold reaction cross sections.

The same principle applies to measuring fast and high-energy neutrons ($E > \sim$ 0.5 MeV) with foil activation, but the reaction cross sections have a different energy feature. Inelastic scattering, (n,xn), and some (n,p) and (n,α) reactions only occur when the incident neutrons exceed a threshold energy [7]. These threshold reactions have effectively a zero cross section below the threshold, but some finite value above the threshold (Figure 2.3). Therefore, activation from these reactions are only due to neutrons with energies above the threshold. Threshold reactions have cross section values typically in the range of 10^{-3}–10 b.

When the activation from multiple reactions with differing thresholds are measured, determining the neutron flux spectra with greater energy detail is possible. Multiple threshold reactions may occur with the same nuclide (*e.g.* ^{58}Ni(n,p) and ^{58}Ni(n,2n)), but typically more reactions can be included by irradiating multiple foils. For example, ^{24}Na nuclei from ^{24}Mg(n,p) reactions are due to neutrons with energies greater than the

threshold of 6.0 MeV, and nuclei ^{57}Ni from ^{58}Ni(n,2n) reactions are due to neutrons with energies greater than the threshold of 13.0 MeV [8]. The neutron flux in the energy ranges 6.0 MeV$< E <$13.0 MeV and $E >$13.0 MeV can be determined by measuring the reaction activation. When several reaction thresholds span a broad range of energies, a discrete neutron flux spectra in that range can be determined.

Advantages of the multiple foil activation technique:

1. Because of the relatively low value of the reaction cross sections, foils can be several millimeters thick without disturbing the neutron field.

2. The foils are practically insensitive to gamma radiation, so they may be employed in mixed radiation fields.

3. Foils have a small profile and can fit in many locations.

4. Foils can be placed in high radiation environment that would damage or degrade other kinds of instrumentation.

Disadvantages of the multiple foil activation technique:

1. Because foil activity is measured after irradiation, live measurements are not possible.

2. Activity measurements, and therefore counting statistics, depend on the time between when irradiation ends and counting begins, so measurements are time sensitive.

3. Well-known cross sections and foil material properties are required.

2.2.2 Foil Criteria

Foils selected for irradiation and subsequent gamma spectrometry should possess several useful qualities.

- The foil's composition should be known precisely because unknown contaminants will introduce errors in mass and possibly activity. Foils of non-uniform composition will complicate the activation analysis and should be avoided.

11

- Cross section values for selected reactions should be well known over the incident neutron energy range.

- Preferably, the half-life of product nuclides used for measurements range between several hours and a few years, but those with half-lives outside this range also may be useful. Nuclides with short half-lives will achieve equilibrium faster during irradiation, but will also decay more quickly after irradiation. For short lived nuclides, much of the induced activity may decay during the time interval between irradiation and gamma spectrometry. For long lived nuclides, an insignificant number of decays may occur during gamma spectrometry, leading to poor counting statistics.

- For a selected reaction, the value of the cross-section should be large enough over a range of energies to produce significant activity during the counting time.

- Competing reaction channels should be minimized. This may be achieved in part by selecting foils composed of few nuclides, preferably only one. Foils composed of a naturally monoisotopic element make good candidates. The (n,xn) reactions make good candidate reactions because the reaction products cannot be produced through competing reaction channels. Inelastic scattering reactions (n,n') may be used, provided the reaction cross sections are known.

- Products must emit gamma radiation during decay, and the gamma's energy must be considered. The likelihood of detecting a photon of a particular energy is affected by the foil self-attenuation and the detector efficiency. Harder gammas are more likely to escape the foil, but the High Purity Germanium (HPGe) detector efficiency is maximal around 130 keV.

- A decay channel with greater gamma emission probability will improve counting statistics, all other factors being equal.

- The foil surface area should either be large enough to fully encompass the beam, or should be small enough to be fully immersed in the beam. Non-uniform or partial irradiation of the foil complicates the activation analysis.

- The number of foil nuclei should be great enough to produce significant activity during counting. The number of nuclei can be increased by increasing the density, thickness, or surface area of the foils.

- The foil should be thin enough that the flux is not significantly perturbed as the beam transits it.

- The foil should be thin enough such that the product gamma radiation intensity is not significantly attenuated.

2.2.3 Activity During Irradiation

Radioactive decay for any nuclide i occurs with a constant relative rate λ_i. In any two time intervals of the equal length, the same proportion of decays occur relative to the total number of nuclei N_i. The activity $A_i(t)$ is magnitude of the decay rate:

$$\frac{dN_i(t)}{dt} = -\lambda_i N_i(t) \tag{2.3}$$

$$A_i(t) = \lambda_i N_i(t) \tag{2.4}$$

The solution to the differential equation 2.3 is the familiar exponential-decay equation:

$$N_i(t) = N_i(0)e^{-\lambda_i t} \tag{2.5}$$

During irradiation, the nuclide i can be produced and destroyed by reactions due to a time-independent[2] (constant) neutron flux $\phi(E)$. Three processes determine the net production rate of the N_i nuclei:

$$\frac{dN_i(t)}{dt} = \qquad \text{production} \qquad - \qquad \text{destruction} \qquad - \qquad \text{decay}$$

$$\frac{dN_i(t)}{dt} = \left(N_j(t) \int_0^\infty \sigma_j(E)\phi(E)dE \right) - \left(N_i(t) \int_0^\infty \sigma_i(E)\phi(E)dE \right) - (N_i(t)\lambda_i) \tag{2.6}$$

---

[2]Activity due to a time-dependent flux will be considered in section 4.3.4

The target nuclei N_j have a microscopic reaction cross-section of σ_j, and the N_i nuclei have a cross-section of σ_i. With the initial condition $N_i(0) = 0$ and using

$$\overline{\sigma\phi} = \int_0^\infty \sigma(E)\phi(E)dE \tag{2.7}$$

to simplify the notation, equation (2.6) can be solved:

$$\frac{dN_i(t)}{dt} = \overline{\sigma_j\phi}N_j(t) - N_i(t)\overline{\sigma_i\phi} - N_i(t)\lambda_i$$

$$\frac{dN_i(t)}{dt}e^{(\lambda_i+\overline{\sigma_i\phi})t} + (\lambda_i + \overline{\sigma_i\phi})N_i(t)e^{(\lambda_i+\overline{\sigma_i\phi})t} = \overline{\sigma_j\phi}N_j(t)e^{(\lambda_i+\overline{\sigma_i\phi})t}$$

$$\int_0^t \frac{d}{dt}\left(N_i(t)e^{(\lambda_i+\overline{\sigma_i\phi})t}\right)dt = \int_0^t \overline{\sigma_j\phi}N_j(t)e^{(\lambda_i+\overline{\sigma_i\phi})t}dt$$

$$N_i(t)e^{(\lambda_i+\overline{\sigma_i\phi})t} = \int_0^t \overline{\sigma_j\phi}N_j(0)e^{-\overline{\sigma_j\phi}t}e^{(\lambda_i+\overline{\sigma_i\phi})t}dt$$

$$N_i(t) = \frac{N_j(0)\overline{\sigma_j\phi}}{\lambda_i + \overline{\sigma_i\phi} - \overline{\sigma_j\phi}}\left(e^{-\overline{\sigma_j\phi}t} - e^{-(\lambda_i+\overline{\sigma_i\phi})t}\right) \tag{2.8}$$

The activity can be expressed by combining equations (2.4) and (2.8):

$$A_i(t) = N_i(t)\lambda_i = \frac{N_j(0)\overline{\sigma_j\phi}}{1 + \frac{1}{\lambda_i}(\overline{\sigma_i\phi} - \overline{\sigma_j\phi})}\left(e^{-\overline{\sigma_j\phi}t} - e^{-(\lambda_i+\overline{\sigma_i\phi})t}\right) \tag{2.9}$$

Two practical approximations can be made:

1. Destruction of target nuclide j can be neglected $\overline{\sigma_j\phi} \ll 1$ which implies: $e^{-\overline{\sigma_j\phi}t} \approx 1$ and $\overline{\sigma_i\phi} - \overline{\sigma_j\phi} \approx \overline{\sigma_i\phi}$

2. Product nuclei i will decay much faster than they will be transmuted: $\lambda_i \gg \overline{\sigma_i\phi}$

These approximations are justified for the cross sections and fluxes under consideration for reasonable irradiation times. For example, using conservative estimates of 10 b for an average threshold reaction cross section and an estimated average high-energy flux of $10^9 \frac{n}{cm^2s}$, the microscopic reaction rates are 10^{-14} s^{-1} reactions per atom. This value is much smaller than any decay constant under consideration, and to destroy 1% of the target nuclei would take more than 10^{12} s (3.2×10^4 years).

Using these two approximations, equation (2.8) can be simplified to the foil activity $A_\phi(t)$ during irradiation at time t due to a time independent flux $\phi(E)$:

$$A_\phi(t) = N_j\overline{\sigma_j\phi}(1 - e^{-\lambda_i t}) \qquad (2.10)$$

Written with explicit energy dependence as:

$$A_\phi(t) = N_j(1 - e^{-\lambda_i t}) \int_0^\infty \sigma_j(E)\phi(E)dE \qquad (2.11)$$

Equation (2.10) illustrates the asymptotic behavior of the activity as a function of time. As $t \to \infty$, $e^{-\lambda_i t} \to 0$ and the activity approaches the saturation level A_{sat}.

$$\lim_{t\to\infty} A_\phi(t) = N_j\overline{\sigma_j\phi}$$
$$\lim_{t\to\infty} A_\phi(t) = A_{\text{sat}}$$

$N_j\overline{\sigma_j\phi}$ is the reaction rate, so:

$$\text{Saturation Activity} = \text{Reaction Rate} \qquad (2.12)$$
$$A_{\text{sat}} = N_j\overline{\sigma_j\phi}$$

This is the equilibrium condition, when the rate of decay is equal to the rate of production. As Figure 2.4 illustrates, the activity during irradiation approaches saturation after $\sim$7–8 half-lives.

2.2.4 Activity After Irradiation

The activity $A_i(t)$ due to nuclide i after irradiation follows the exponential decay law:

$$A_i(t) = A_i(t_0)e^{-\lambda_i t} \qquad (2.13)$$

where t_0 is any previous time after irradiation and λ_i is the decay constant. Because activity measurements occur a finite time after irradiation ends, it is convenient to divide the post-irradiation time into two intervals: cooling time and counting time. Cooling time
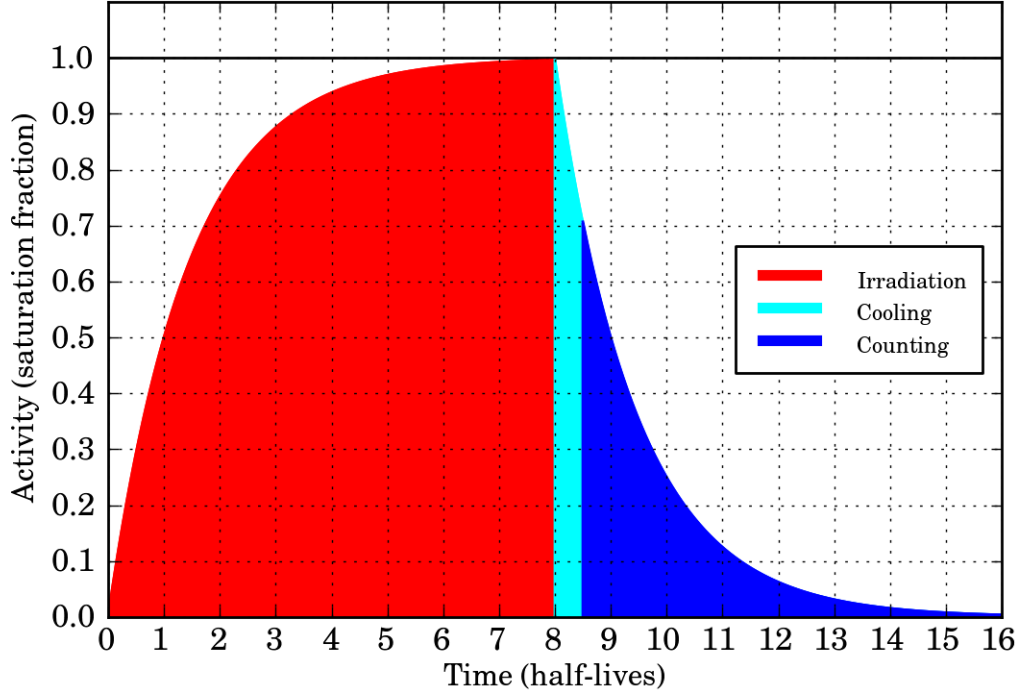
Figure 2.4: Behavior of activity during and after irradiation. After irradiation, the foil activity is measured during the counting time interval. During the short cooling interval, the activity decays but counting does not occur.

is the interval after irradiation ends but before measurement begins. Counting time is the interval during which the activity measurement is occurring. Equation 2.13 describes the activity during both these intervals (Figure 2.4).

2.2.5 Decays and Counts During the Counting Time

The number of nuclear decays D_i of nuclide i that occur during a time interval $[t_a, t_b]$ is the time integral of the activity over the interval:

$$D_i = \int_{t_a}^{t_b} A_i(t)dt = \frac{A_i(t_0)\left(e^{-\lambda t_a} - e^{-\lambda t_b}\right)}{\lambda} \tag{2.14}$$

If the time interval $[t_a, t_b]$ is the counting time, equation 2.14 describes the number of nuclear decays that occur during that interval. The number of decays during the counting time determines the number of counts measured by the HPGe detector.

16

If t_0 is the time at the end of the irradiation, the number of decays during the counting time can be expressed in terms of the saturation activity or the reaction rate. Combining equations 2.10 and 2.14 yields:

$$D_i = \frac{N_j \overline{\sigma_j \phi}(1 - e^{-\lambda_i t_0})}{\lambda} \left(e^{-\lambda t_a} - e^{-\lambda t_b} \right) \tag{2.15}$$

The total number of gamma-rays emitted Γ_i from nuclide i of energy E_γ during the counting period is the gamma emission probability $I_{i,\gamma}(E_\gamma)$ multiplied by the total number of decays.

$$\Gamma_i(E_\gamma) = D_i I_{i,\gamma}(E_\gamma) \tag{2.16}$$

The number of gamma-rays escaping the foil G_i from nuclide i is the number of gamma-rays emitted Γ_i multiplied by a geometry dependent self-shielding[3] factor $F_{\text{self}}(E_\gamma)$

$$G_i(E_\gamma) = F_{\text{self}}(E_\gamma)\Gamma_i(E_\gamma) \tag{2.17}$$

The energy-dependent total detector efficiency ϵ is defined as the the total number of gamma-rays counted C in the detector divided by the total number G of gamma-rays escaping the foil.

$$\epsilon(E_\gamma) \equiv \frac{C(E_\gamma)}{G(E_\gamma)} \tag{2.18}$$

Combining equations 2.15 – 2.18, the number of counts expected in a HPGe detector $\hat{C}_i$ from nuclide i during a time interval $[t_a, t_b]$ is:

$$\hat{C}_i(E_\gamma) = \frac{\epsilon(E_\gamma)F_{\text{self}}(E_\gamma)I_{i,\gamma}(E_\gamma)}{\lambda} N_j \overline{\sigma_j \phi} \left(1 - e^{-\lambda_i t_0} \right) \left(e^{-\lambda t_a} - e^{-\lambda t_b} \right) \tag{2.19}$$

Due to the random nature of radioactive decay the actual number of counts measured in the detector will vary[4] from the value given by equation 2.19.

---

[3]The self-shielding factor is computed in section 4.3.3.

[4]The variance in the number of counts is discussed in Section 2.3.4.

2.3   Gamma Spectrometry

2.3.1   Gamma-ray Physics

Nuclear gamma-rays are electromagnetic radiation in the energy range of $\sim$10 keV–10 MeV. This range overlaps with X-rays ($\sim$120 eV–120 keV), and the distinction between the two lies only in their origin. If radiation in this overlapping energy range originates from electrons, it is considered an X-ray, but if the radiation originates from the nucleus, it is considered a gamma-ray.

Gamma-rays can interact with both the nucleus and the atomic electrons of an atom, but when considering interactions between the gamma-rays and detector in HPGe spectrometry, the photo-atomic interactions are most relevant. A gamma-ray undergoes one of three primary physical processes when it interacts with an atom: photoelectric absorption, Compton scattering, or pair production.

Photoelectric Absorption

Photoelectric absorption occurs when a gamma-ray is absorbed by an atomic electron, and that electron is ejected from the atomic shell with kinetic energy from the gamma-ray. The kinetic energy of the electron E_e is given by the conservation of energy as:

$$E_e = E_\gamma - E_b \tag{2.20}$$

where E_γ is the gamma-ray energy, and E_b is the energy binding the atomic electron to its shell. Gamma-rays have sufficient energy to eject electrons of the inner K, L, and M atomic shells. Sharp absorption edges exist the in the photo-atomic cross sections (Figure 2.5) where energies less than the edge are insufficient to eject electrons from the next inner shell, while energies above the edge are sufficient.

After ejection of the electron, the atom is left in an excited state with excess energy E_b. To release the excess energy, the atom de-excites in one of two ways: the ejection of additional (Auger) electrons, or the redistribution of electron in their shells. When electrons are redistributed, less tightly bound electrons in outer shells fall into the inner shell vacancies, releasing energy through X-ray fluorescence.
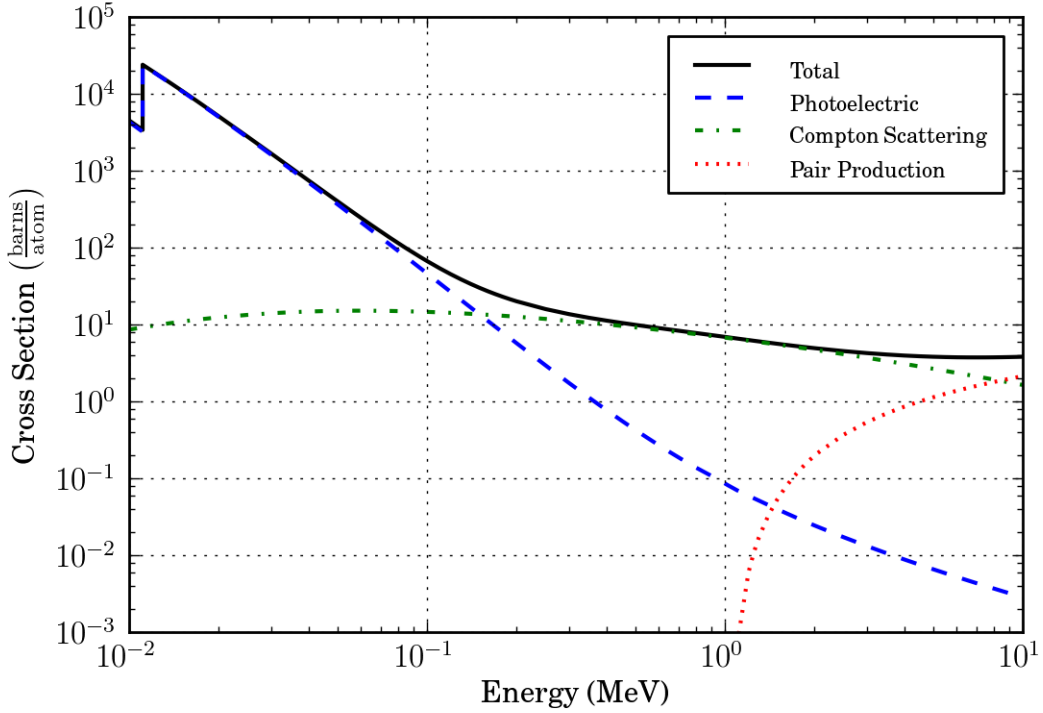
Figure 2.5: The gamma-ray reaction cross sections of germanium [9] illustrate the three primary mechanisms of gamma-ray interaction. Note the K shell absorption edge at 11.1 keV and the threshold of pair production at 1022 keV.

Compton Scattering

When a gamma-ray imparts a fraction of its energy to an atomic electron, the interaction is called Compton scattering. Compton scattering often occurs with loosely bound electrons where $E_\gamma \gg E_b$, so the binding energy can neglected and the electron can be considered free. For the case of a free electron, the kinetic energy imparted to the electron can be derived through conservation of energy and momentum:

$$\text{Conservation of Energy: } E_e = E_\gamma - E'_\gamma \tag{2.21}$$

$$\text{Conservation of Momentum: } E_e = E_\gamma \left(1 - \frac{1}{1 + E_\gamma(1 - cos\theta)/m_e c^2}\right) \tag{2.22}$$

where E'_γ is the energy of the scattered gamma-ray, θ is the scattering angle, and $m_e c^2$ is the rest energy of the electron (~ 511 kev).

By definition, the full energy of the gamma-ray is not transferred to the electron

in Compton scattering, but kinematics prohibit a range of energy loss less than the full energy. From equation 2.21, the energy lost by the gamma-ray is maximal when E_e is maximal, and from equation 2.22, E_e is maximal when $\theta = \pm\pi$. This is the backscattering case where:

$$\text{Backscattering:} \qquad E_e = E_\gamma - \frac{1}{\frac{1}{E_\gamma} + \frac{2}{m_e c^2}} \qquad (2.23)$$

$$\lim_{E_\gamma \to \infty} \left(\frac{1}{\frac{1}{E_\gamma} + \frac{2}{m_e c^2}} \right) = \frac{m_e c^2}{2}$$

$$\text{Therefore:} \qquad E_e < E_\gamma - \frac{m_e c^2}{2} \qquad (2.24)$$

The actual upper limit of energy loss is determined by equation 2.23, and equation 2.24 shows that energy loss will never be within 255.5 keV of E_γ. This prohibited range of energy loss is important to understanding the features of the measured gamma-ray spectrum (Section 2.3.3).

Pair Production

When a particle and its antiparticle collide, the two annihilate in a burst of gamma radiation with equivalent energy. Pair production is the symmetric process to particle annihilation. Pair production occurs within the Coulomb field of the nucleus when a gamma-ray transforms into a particle and its antiparticle.

The case that is relevant for gamma-ray spectrometry is electron-positron pair production. In order for electron-positron production to occur, the gamma-ray must have at least as much energy as the rest energies of the pair $2m_e c^2 = 1022$ keV. Gamma-rays with less than 1022 keV cannot undergo pair production (Figure 2.5). The excess energy during pair production is distributed equally among the particle pair:

$$E_{e-} = E_{e+} = \frac{E_\gamma - 2m_e c^2}{2} \qquad (2.25)$$

where E_{e-} and E_{e+} are the electron and positron energies respectively. Once created, the electron and positron continue to interact with surrounding atoms and nuclei. Inevitably, the positron loses its kinetic energy and collides with an electron, thus releasing

two annihilation gamma-rays of 511 keV.

2.3.2 The High Purity Germanium (HPGe) Detector

The principle underlying all gamma-ray spectrometers is that the number of ionizations due to the gamma-ray that occur within the detector material is proportional to the energy absorbed. If all of the gamma-ray energy is absorbed in the detector, the number of ionizations is proportional to the energy of the gamma-ray. Gamma-ray spectrometers vary in material, which determines the energy per ionization, and the mechanism used to measure the ionization. Scintillator-based spectrometers use photons to measure ionization, and semiconductor-based spectrometers use electron-hole pairs.

The HPGe gamma-ray spectrometer is a semiconductor-based detector. In solid materials, electron energy levels become energy bands. The uppermost occupied energy band, which is responsible for chemical bonding, is known as the valence band. Beyond the valence band, separated (in semiconductors) by a range of prohibited energies called the band gap, lies a conduction band that allows charge to move through the material. In semiconductors, the band gap is small enough that some thermally excited electrons may move from the valence band to the conduction band, allowing some degree of conductivity.

When a gamma-ray enters the germanium, it undergoes a series of photoelectric, Compton scattering, and pair production interactions that ultimately cause the promotion of electrons from the valence band into the conduction band. The absence of an electron in the valence band is called a hole. When an electron is promoted to the conduction band, adjacent valence electrons move to fill the vacancy and a hole effectively propagates in the opposite direction. When an electric potential (voltage) is applied across the germanium, the conduction band electrons propagate toward the cathode and holes propagate toward the anode. By measuring the change in voltage, the number of ionizations, and therefore the absorbed energy, can be measured. Voltage pulses are recorded by an electronics system that includes a Multi-Chanel Analyzer (MCA), which counts and sorts the pulses by height.

To distinguish one gamma-ray's energy from the next, the electrons and holes must propagate through the material quickly. Dislocations and impurities in the semiconductor lattice can reduce the mobility of the charge carriers in the material, so a single

crystal of high purity is used. Germanium has become the standard material of semiconductor gamma-ray spectrometers because of the high mobility of its charge carriers and its large absorption coefficient, which allows for detection of higher energy gamma-rays. Unfortunately, the band gap in germanium is so small that too many electrons move into the conduction band due to mere thermal excitation, rather than promotion due to gamma-ray energy. This "leakage current" is reduced by reducing the thermal excitation of the electrons (cooling the material). For this reason, HPGe systems are operated at liquid nitrogen (LN2) temperatures (77 K).

2.3.3 The Gamma-ray Spectrum

In a hypothetical infinitely large detector, every entering gamma-ray would be unable to exit, so each would transfer all of its energy to the detector material. Ionizations would occur and the voltage pulse heights would be recorded by the MCA. Even in this hypothetical scenario, every voltage pulse would not be recorded identically for gamma-rays of the same energy. Uncertainties in the process cause pulses to be recorded with some variance around a central peak. These uncertainties can be added in quadrature to yield an overall energy measurement uncertainty ω:

$$\omega^2 = \omega_I^2 + \omega_P^2 + \omega_C^2 + \omega_E^2 \tag{2.26}$$

The intrinsic variance ω_I^2 in the actual gamma-ray energy emitted by a nuclide is quite small and can be neglected. The variance in charge production ω_P^2 is an inherent property of the detector material so it cannot be reduced. The variance due to charge collection ω_C^2 is due to crystal defects and geometry. Variance due to electronic noise ω_E^2 can be minimized with properly adjusted electronic components of high-quality and a clean supply of power. The total uncertainty in gamma-ray energy measurement is known as resolution. A spectrometer's resolution, a function of the energy absorbed, is the reason gamma-ray peaks have a finite width.

The peak located at the energy of the incident gamma-ray is known as the full-energy peak or photopeak. When a gamma-ray enters the detector and is absorbed through a photoelectric interaction, the energy of the ejected electron will ultimately lead to the
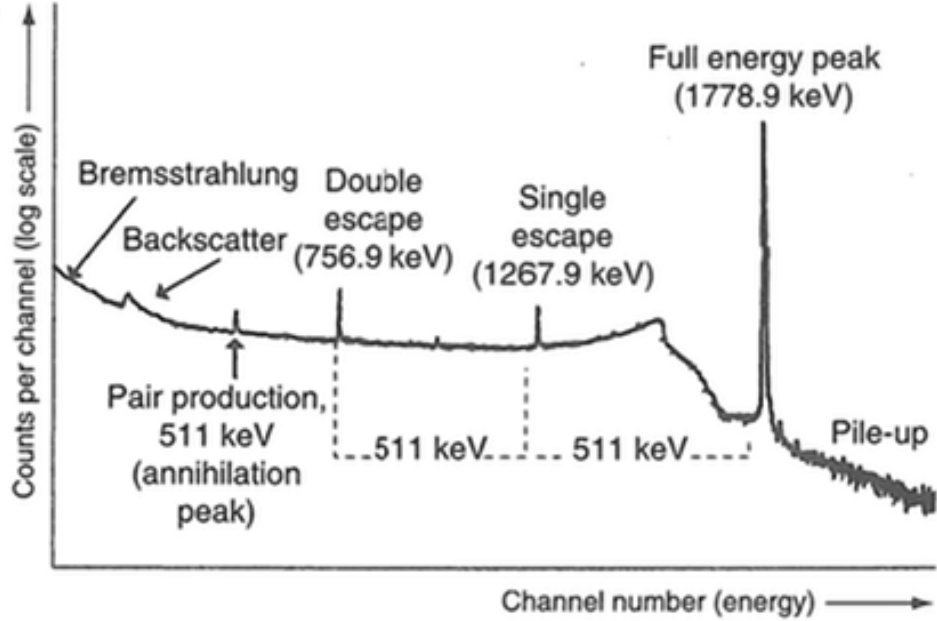
Figure 2.6: The gamma-ray spectrum of ^{28}Al illustrating the major features [10].

promotion of a proportionate number of electrons to the conduction band. When this occurs, the MCA records a count in channels around the full-energy.

Real detectors are not infinitely large, so gamma-rays may exit the detector before fully depositing their energy. For this reason, gamma-ray spectra contain several features in addition to the full-energy peak (Figure 2.6). A gamma-ray that Compton scatters once and then exits the detector transfers some of its energy to a Compton electron. Like the photoelectron, the Compton electron causes an energy proportional number of electrons to be promoted to the conduction band. The energy transferred to the Compton electron is governed by equations 2.21 and 2.22 and ranges between:

$$0 < E_c \leq E_\gamma - \frac{1}{\frac{1}{E_\gamma} + \frac{2}{m_e c^2}} \tag{2.27}$$

For this reason, the MCA will record these events in channels spanning a continuum of energies less than the full-energy peak. This is known as the Compton continuum, and the upper limit is the Compton edge. Atomic binding energies (neglected in equations 2.21 and 2.22) and spectrometer resolution cause the Compton edge to be softened into a Compton shoulder. One figure-of-merit of a gamma spectrometer is the peak-to-Compton

23

ratio, which is the ratio of counts in a ^{60}Co full-energy peak to the average counts in the Compton continuum [10]. Should a once-scattered gamma-ray Compton scatter again before exiting the detector, it may deposit more energy than the Compton edge of its first scattering. Therefore, the energy range between the Compton shoulder and the full-energy peak is called the multiple Compton region.

For gamma-rays with $E_\gamma > 1022$ keV, pair production can occur inside the source material, inside the detector, or in any nearby material. When pair-production occurs in material outside of the detector, the positron quickly loses its kinetic energy and annihilates with an electron producing two $\sim$511 keV gamma-rays[5]. These gamma-rays may then enter the detector and deposit their energy. This is one reason an annihilation peak at 511 keV often appears in spectra along with gamma-rays more energetic than 1022 keV. Another source for annihilation gamma-rays is nuclear decay by positron emission, for example ^{22}Na $\xrightarrow{\beta+}$ ^{22}Ne.

When pair production occurs within the detector material, two annihilation gamma-rays are also created. Annihilation typically occurs within 1 ns of pair production, which is practically instantaneous compared to the detector charge collection time of 100–700 ns [10]. One or both of these 511 keV gamma-rays may escape the detector without depositing their energy. When this occurs, two additional peaks appear in the spectrum:

$$\text{Single Escape Peak: } E_{\text{escape},1} = E_\gamma - 511 \text{ keV} \tag{2.28}$$

$$\text{Double Escape Peak: } E_{\text{escape},2} = E_\gamma - 1022 \text{ keV} \tag{2.29}$$

The full-energy, annihilation, single and double escape peaks along with the Compton continuum form the major features of a gamma-ray spectrum. Additionally, several minor features are also present. A backscattering peak in the range of 200–250 keV may be present [11]. The backscattering peak is due to gamma-rays Compton backscattering off adjacent material before entering to the detector. Fluorescence X-rays resulting from ejected photoelectrons in the source or adjacent materials also may be detected. Finally, sum peaks resulting from contemporaneous gamma-rays both depositing all of their

---

[5]The net momentum during the collision gives rise to small deviations in the energies of the gamma-rays $(511 \pm \delta$ keV). This causes the annihilation peak in the gamma spectrum to be Doppler broadened.

energy also can occur.

2.3.4 Counting Statistics

Counting nuclear decays is a measurement process subject to both the random and systematic errors. Random errors are experimental uncertainties that can be revealed by repeated measurements; those that cannot be revealed by repetition are systematic errors [12]. An important component of the random error of counting measurements is determined by the statistics of radioactive decay.

Radioactive decay is a Bernoulli process that occurs with a binomial distribution. The expected number of decays that occur in a time interval $[0, t]$ is the mean μ of the binomial distribution:

$$\mu = Np(t) \tag{2.30}$$

which is the number of nuclei N multiplied by the probability of a decay during the time interval, the cumulative distribution function (CDF) $p(t)$. The variance, or expected squared error, of the binomial distribution is σ^2:

$$\sigma^2 = Np(t)q(t) \tag{2.31}$$

where $q(t)$ is the probability of a non-decay. Using $p(t) + q(t) = 1$ and equation 2.5:

$$p(t) = 1 - e^{-\lambda t} \tag{2.32}$$

$$q(t) = \quad e^{-\lambda t} \tag{2.33}$$

When $\lambda t \ll 1$, $q(t) \approx 1$ and the binomial distribution can be approximated very well by a Poisson distribution:

$$\mu \approx Np(t) \tag{2.34}$$

$$\sigma \approx \sqrt{\mu} \tag{2.35}$$

where the square-root of the variance is the standard deviation σ. To determine the statistics of counting, two ranges of count times are considered: short count times and long

count times. In both cases, the error in the time measurement is assumed to be negligible.

Short Count Time

During a short count time $\lambda t \ll 1$, Poisson statistics are valid, and $\sigma_C(t) = \sqrt{C(t)}$ where $C(t)$ is the measured[6] number of counts. Assuming a constant background count rate $B(t) = \dot{B}t$, and using equation 2.32 to determine the number of true decays $D(t)$, the count rate $\dot{C}$ is:

$$\dot{C} = \frac{d}{dt}\left(\epsilon D(t) + B(t)\right) = \epsilon N \lambda \,\cancelto{1}{e^{-\lambda t}} + \dot{B}$$

where ϵ is the detector efficiency. $\dot{C}$ is constant, therefore $C(t) = \dot{C}t$ yields $\dot{C} = C(t)/t$. The standard deviation of the decay rate $\sigma_{\dot{C}}$ is:

$$\sigma_{\dot{C}}(t) = \frac{\sigma(t)}{t} = \sqrt{\frac{\dot{C}}{t}} \tag{2.36}$$

The uncertainty in the count rate decreases as the square root of the count time. The net count rate $\dot{C}_n$ is the background count rate $\dot{B}$ subtracted from the total count rate $\dot{C}$:

$$\dot{C}_n = \dot{C} - \dot{B} = \frac{C(t)}{t} - \frac{B(t)}{t_B} \tag{2.37}$$

where the background counts were independently measured over a time t_B. The independent measurements of the background rate and total count rates allows for their uncertainty to be added in quadrature:

$$
\begin{aligned}
\sigma^2_{\dot{C}n}(t) &= \sigma^2_{\dot{C}}(t) + \sigma^2_{\dot{B}}(t) \\
\sigma_{\dot{C}n}(t) &= \sqrt{\frac{\sigma^2_C(t)}{t^2} + \frac{\sigma^2_B(t)}{t_B^2}} = \sqrt{\frac{C(t)}{t^2} - \frac{B(t)}{t_B^2}}
\end{aligned}
\tag{2.38}
$$

The measurement of the net count rate and its uncertainty can be expressed as:

$$\dot{C}_n \pm \sigma_{\dot{C}n}(t) = \frac{C(t)}{t} - \frac{B(t)}{t_B} \pm \sqrt{\frac{C(t)}{t^2} - \frac{B(t)}{t_B^2}} \tag{2.39}$$

---

[6]The measured number of counts is not necessarily equivalent to the expected number of counts, but it is assumed to be the best estimate [8].

Long Count Times

During long count times $\lambda t \gtrsim 1$, Poisson statistics would appear not to be a good approximation and use of the binomial distribution would seem necessary. Fortunately, the background count rates remain Poisson distributed, thus the total count rate is Poisson distributed [10]. Therefore, equation 2.39 remains valid for long count times provided $\dot{C}_n$ is regarded as the measured mean net count rate:

$$\dot{C}_n = \frac{C_n(t)}{t} \tag{2.40}$$

To determine the net count rate at the start of counting time, a unit-less correction that accounts for the decay during acquisition can be applied [13]:

$$\text{Decay During Acquisition Corrrection} = \left(\frac{\lambda t}{1 - e^{-\lambda t}} \right) \tag{2.41}$$

For the net count rate at any time $\tau \in [0, t]$, the additional factor $e^{-\lambda \tau}$ can be applied. The measurement of the net count rate at the start of the counting time and its uncertainty can be expressed as:

$$\dot{C}_n(0) \pm \sigma_{\dot{C}n}(t) = \left(\frac{\lambda t}{1 - e^{-\lambda t}} \right) \left(\frac{C(t)}{t} - \frac{B(t)}{t_B} \right) \pm \sqrt{\frac{C(t)}{t^2} - \frac{B(t)}{t_B^2}} \tag{2.42}$$

2.4   Spectral Unfolding

2.4.1   Response Matrix

To compute the neutron flux spectrum from the activity measurements, unfolding calculations are required. In practice, unfolding is carried out by computer software because using one of several specialized iterative algorithms is required. The matrix form of the response equation will be explained in this section, while the particular software and algorithm chosen to find solutions will be discussed in section 4.2.2.

The response function R is defined as the ratio of the instrument reading $\mathcal{M}$ to the value of the quantity to be measured by the instrument, for a specified type, energy and direction distribution of radiation [14]. In this work, the neutron flux is the desired

quantity to be measured, so all response functions are "flux response functions." Using the above definition, R is the ratio of $\mathcal{M}$ to the neutron flux ϕ:

$$R = \frac{\mathcal{M}}{\phi} \tag{2.43}$$

For the purposes of unfolding, $\mathcal{M}$ can be any convenient quantity based on the gamma spectrometer reading. For example, $\mathcal{M}$ could be the activity or it could be the reaction rate calculated from the activity using equation 2.10.

A single reading $\mathcal{M}_m$ is defined as the integral of the energy dependent response function $R(E)$ and the flux $\phi(E)$ over an energy range.

$$\mathcal{M}_m = \int_{E_{\min}}^{E_{\max}} R(E)\phi(E)dE \tag{2.44}$$

The energy range between $E_{\min}$ and $E_{\max}$ can be divided into N energy groups with $N+1$ group boundaries, and equation (2.44) can be rewritten exactly as:

$$\mathcal{M}_m = \sum_{n=1}^{N} \int_{E_n}^{E_{n+1}} R(E)\phi(E)dE$$

$$\mathcal{M}_m = \sum_{n=1}^{N} \frac{\int_{E_n}^{E_{n+1}} R(E)\phi(E)dE}{\int_{E_n}^{E_{n+1}} \phi(E)dE} \int_{E_n}^{E_{n+1}} \phi(E)dE$$

with

$$R_{mn} = \frac{\int_{E_n}^{E_{n+1}} R(E)\phi(E)dE}{\int_{E_n}^{E_{n+1}} \phi(E)dE} \tag{2.45}$$

$$\phi_n = \int_{E_n}^{E_{n+1}} \phi(E)dE \tag{2.46}$$

$$\mathcal{M}_m = \sum_{n=1}^{N} R_{mn}\ \phi_n \tag{2.47}$$

Equation (2.45) defines the N *group averaged response function values* R_{mn} for a single measurement $\mathcal{M}_m$. The N values of ϕ_n defined by equation (2.46) are the *group fluxes*. A total of M measurements are used in the unfolding, so equation (2.47) can be written in a

matrix form:

$$
\begin{bmatrix} \mathcal{M}_1 \\ \mathcal{M}_2 \\ \vdots \\ \mathcal{M}_M \end{bmatrix} = \begin{bmatrix} R_{11} & R_{12} & \dots & R_{1N} \\ R_{21} & R_{22} & \dots & R_{2N} \\ \vdots & \vdots & \ddots & \vdots \\ R_{M1} & R_{M2} & \dots & R_{MN} \end{bmatrix} \begin{bmatrix} \phi_1 \\ \phi_2 \\ \vdots \\ \phi_N \end{bmatrix}
$$
$$
\vec{\mathcal{M}} \quad = \qquad\qquad \mathbf{R} \qquad\qquad \vec{\phi} \tag{2.48}
$$

In equation 2.48, $\vec{\mathcal{M}}$ comes from the gamma spectrometer readings, $\vec{\phi}$ are solved by using an unfolding algorithm, and the response matrix $\mathbf{R}$ must be known. The response matrix elements R_{mn} are essentially the contribution of the flux ϕ in each energy group n to the overall spectrometer reading $\mathcal{M}$ for a reaction m.

The response matrix $\mathbf{R}$ could be empirically determined through foil measurements with an energy calibrated neutron source. This empirical technique is possible for neutrons at thermal energies [15], but calibrated high-energy neutron sources are generally unavailable. The response matrix also can be computed based on nuclear cross sections, foil composition, and foil geometry. All response matrices used in this work are computed using the Monte Carlo transport code MCNPX.

To compute the response matrix elements R_{mn}, the form of the instrument reading $\mathcal{M}$ must be specified. For practical reasons, $\mathcal{M}$ was selected to be the "reaction rate during irradiation." MCNPX can output reaction rates, but it does not output activity over time due to radioactive decay. Conversion to activity can only be done in post-processing once MCNPX is finished. Considering equation 2.48, it is simpler to convert the activity measured by the gamma spectrometer into reaction rates rather than converting MCNPX's reaction rates into activity. Converting activity to reaction rate in the $\vec{\mathcal{M}}$ vector entails M operations, while converting reaction rates to activity in the $\mathbf{R}$ matrix would entail $M \times N$ operations.

Having specified the instrument reading $\mathcal{M}$ as "reaction rate during irradiation," the form of R_{mn} can be specified as:

$$
R_{mn} = \frac{\int_{E_n}^{E_{n+1}} N_m \sigma_m(E) \phi(E) dE}{\int_{E_n}^{E_{n+1}} \phi(E) dE} \tag{2.49}
$$

29

2.4.2   Monte Carlo Neutron Transport Methods

The Monte Carlo method, or the method of statistical trials, has long been a useful for neutronics computations. By using basic nuclear data combined with problem specific material geometry and composition, many particle histories are simulated mathematically. Individual histories use pseudo-random numbers selected from natural or modified distributions of position, energy, distance, collision type, and reaction products. The method's strength is its accuracy, while its weakness is the long computational times required. The subject is far too vast for a detailed description, but some general features are discussed [16].

Monte Carlo methods are used to calculate the sample mean of some quantity, for example, the scalar flux inside some geometrically defined region. The scalar flux can be defined in several equivalent ways, one of which uses the total track length of all particles traversing a region per unit volume per unit time:

$$\overline{\phi} = \frac{1}{V}\overline{l} \tag{2.50}$$

where $\overline{\phi}$ is the mean scalar flux, V is the volume of the region, and $\overline{l}$ is the mean track length per source particle. The sample mean $\hat{x}_N$ of N histories takes a general form of:

$$\hat{x}_N = \frac{1}{N}\sum_{n=1}^{N} x_n \tag{2.51}$$

where x_n is the result of the trial n. A Monte Carlo estimate of the mean scalar flux can be made by using the sample mean of the scalar flux $\hat{\phi}$:

$$\hat{\phi}_N = \frac{1}{V}\frac{1}{N}\sum_{n=1}^{N} l_n \tag{2.52}$$

where l_n is the track length of trial n.

On average, the sample mean $\hat{x}_N$ deviates from the true mean $\overline{x}$ by some amount. The spread of $\hat{x}_N$ around $\overline{x}$ is characterized by the variance of the mean $\sigma^2_{\hat{x}N}$. The variance

of the mean $\sigma_{\hat{x}N}^2$ is related to the variance of the distribution of all histories σ_x^2:

$$\sigma_{\hat{x}N}^2 = \frac{\sigma_x^2}{N}$$
$$\sigma_{\hat{x}N} = \frac{\sigma_x}{\sqrt{N}} \tag{2.53}$$

Equation 2.53 shows that halving the standard deviation of a Monte Carlo calculation requires four times as many histories. The true variance σ_x^2 is unknown, but it can be estimated from the sample variance S_N^2:

$$S_N^2 = \frac{1}{N-1}\sum_{n=1}^{N}(x_n - \hat{x_N})^2 = \frac{N}{N-1}\left(\sum_{n=1}^{N}\frac{x_i^2}{N} - \left(\sum_{n=1}^{N}\frac{x_i}{N}\right)^2\right) \tag{2.54}$$

From the Law of Large numbers, it is known that:

$$\lim_{N\to\infty} \hat{x}_N = \overline{x} \tag{2.55}$$

From the Central Limit Theorem, it is known that for sufficiently large N, the $\hat{x}_N$ are normally distributed around $\overline{x}$. Therefore, any Monte Carlo estimate and its standard error can be expressed as:

$$\hat{x}_N \pm S_N = \frac{1}{N}\sum_{n=1}^{N}x_n \pm \sqrt{\frac{1}{N-1}\left(\sum_{n=1}^{N}\frac{x_i^2}{N} - \left(\sum_{n=1}^{N}\frac{x_i}{N}\right)^2\right)} \tag{2.56}$$

In this work, through the use of the use of MCNPX software, the Monte Carlo method is used to calculate reaction rates and fluxes inside simulated foil regions.

Chapter 3

Experimental Apparatus

This chapter outlines the equipment used to conduct the measurements. The selection of equipment was determined by factors such as practicality, cost, and availability.

3.1 The Spallation Neutron Source (SNS)

3.1.1 The Target Station

The SNS is a particle accelerator facility that directs a high-energy proton beam into a liquid mercury target to generate cold and thermal neutron beams for scientific use. The target station is the collection of systems that surround the target and provide for delivery of neutrons to the beamlines.

The target is flowing liquid mercury inside a 316-type stainless steel vessel. The target is approximately 40 cm wide with a height of 10 cm and an active length of 70 cm for neutron production. [18]. A proton pulse of 18 μC approximately 700 ns in length impacts the target at 60 Hz. The proton beam provides up to 1 MW of power to the target. Heat deposited in the mercury is transported through the flowing mercury loop to a heat exchanger.

Four dedicated moderators, two above and two below, are adjacent to the target (Figure 3.1). Each moderator serves three or more beamlines. Three of the moderators composed of supercritical hydrogen are maintained at cryogenic temperatures (19 K), while one moderator is composed of light-water at ambient temperature. The moderator param-
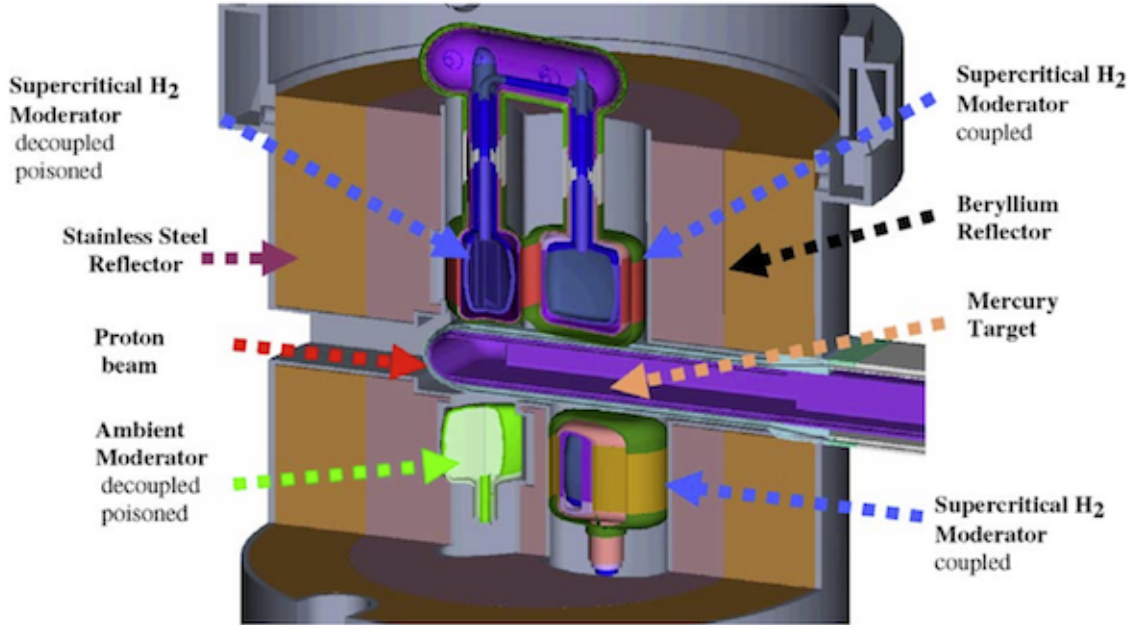
Figure 3.1: The SNS target station [17].

eters such as location and temperature were determined by the general neutron spectrum requirements of the scattering experiments. While neutrons emerge from the moderators in all directions, the neutron beams are considered to emanate from the "viewed face" of the moderator. The forward moderators have two viewed faces while the rear moderators each have one viewed face [18].

The target and moderators are surrounded by a neutron reflector. Reflectors enhance useful neutron production by returning neutrons to the moderators that either leak from the target to the reflector or escape from the moderators in non-useful directions. But reflectors alter the energies and time structure of the resulting emitted neutrons. Neutron poisons such as gadolinium are used inside and around some moderators for tailoring the spectrum and timing of the neutron beams. "Decouplers" geometrically and neutronically isolate the moderators from the reflectors, while "liners" isolate the moderator viewed surface from the reflectors [5]. Two of the moderators at the SNS target station that employ these neutron poisons are said to be neutronically "decoupled" from their surroundings.

The location of the moderators relative to the target precludes spallation neutrons from traveling down beamlines without first scattering in the moderator. This target-

moderator configuration is known as "wing geometry." Wing geometry mitigates the high-energy neutron contamination in the beam at the cost of reducing the overall neutron flux by as much as half when compared to other target-moderator geometries [6].

A core vessel, which serves to contain mercury vapor during target failure, encases the target and moderator systems. Extending radially approximately 1–2 m from the viewed face of the moderator are the core vessel inserts, the first beam-shaping components and physical start of the beamlines [19]. Large moveable shutters can be shifted into the flight path of the neutrons to close off individual beamlines while the target continues to produce neutrons. The entire target station is housed in several thousand tons of radiation shielding known as the target monolith.

3.1.2 Neutron Beamlines

The neutron beamlines are pathways leading from the core vessel inserts to to the sample positions of the scattering instruments. Lateral radiation shielding for personnel protection envelops the beamlines.

Beamlines may be straight or curved and both use super-mirror guides for the transport of low-energy wavelike neutrons. Some beamlines are so curved that no line-of-sight exists between the viewed face of the moderator and the sample position. As high-energy neutrons are not transported along curved guides, these beamlines are not appropriate for high-energy neutron flux spectra measurements.

Pulsed neutron sources like the SNS have an intrinsic neutron beam time structure that is coordinated with the incident proton pulse. Due to the finite time involved in the moderation process, the neutron beam pulses contain a wide spread of energies and need further modification to be useful for specific applications. Choppers, rotating assemblies that alternately block and transmit neutrons with regular frequency, are used to modify the neutron beam. Some beamlines use several choppers over tens of meters for energy selection and neutron pulse time structure. The relative phasing and physical distance of the beamline choppers determines the band of energies transmitted to the sample location. The length of the beamline is important to this work because the high-energy neutron flux will decrease inversely with the square of the distance from the source.

The beamlines at the SNS have several varieties of neutron choppers, most of which are not relevant for high-energy neutron flux spectra measurements. Bandwidth (sometimes called "frame-overlap") choppers set an acceptable band of neutron energies for an experiment and block neutrons from subsequent accelerator pulses. Beamlines may have a T_0 chopper, which is specifically designed to remove the high-energy neutron beam. When high-energy neutron measurements are made on beamlines equipped with T_0 choppers, those choppers should be stopped in the open position to transport high-energy beam to the sample location.

3.1.3 Neutron Instruments

(Wide) Angular-Range Chopper Spectrometer (ARCS)

ARCS is an inelastic scattering instrument designed for the thermal and epithermal energy range. Primary science areas for the instrument include the study of lattice dynamics, such as measuring the phonon density of states of diverse materials, and applications to magnetic dynamics in systems from high temperature superconductors to low dimensional quantum magnets [20]. The instrument views the only ambient temperature light water moderator and is equipped with a T_0 chopper. The sample position is 13.6 m from the moderator viewed face.

POWGEN

POWGEN is a general purpose neutron diffractometer optimized for neutron energies in the range of ∼9–900 meV. Insertable guide sections and the ability to trade resolution for intensity at the analysis stage allow users great latitude to optimize the data range, resolution, and statistical precision for each particular experiment [21]. The instrument views a top upstream cryogenic moderator and is equipped with a T_0 chopper. The sample position is ∼ 60 m from the moderator viewed face.

3.2 Foil Selection

Foils were selected based upon the general criteria of section 2.2.2, references in the literature, scoping calculations of expected counts, and availability. A set of foils that included bismuth, copper, aluminum, and nickel were immediately available. To generate adequate data for spectrum unfolding at least 6 neutron activation reactions are necessary and about 8–10 are recommended [22]. A list of irradiated foils and their physical characteristics can be found in Appendix B.

Bismuth has been acknowledged for its utility in high energy neutron spectrometry at accelerator facilities, and it is the primary foil for measuring the flux spectra above 20 MeV. Measurements of the ^{209}Bi(n,xn), x= 3...12 reaction cross sections [23] have shown good agreement with with the GNASH code based LA150 cross section library [24]. Bismuth is naturally monoisotopic and its (n,xn) products have usable half-lives ranging from minutes to years. Bismuth has been employed as a threshold activation foil at the ISIS spallation source at Rutherford Appleton Laboratory [25], at the Joint Institute for Nuclear Research in Dubna, Russia [26], and at Brookhaven National Laboratory with experiments on a mercury spallation target [27].

For reactions below 20 MeV (^{63}Cu(n,2n) and ^{63}Cu(n,α)), copper has been often used as an threshold activation detector [22, 27, 28]. Measurements with copper foils in the fast-energy range is outlined by ASTM Standard Test Method E 523-11 [29]. Copper also has several threshold reactions above 20MeV (^{65}Cu(n,5n) and ^{65}Cu(n,6n)). In the energy range of 40 – 120 MeV, some natural copper (n,xn) reaction cross sections have been measured [30]. Unfortunately, not all of these data are not in agreement with calculated values. No reference was found for the use of copper as a high-energy activation foil, so the usefulness of copper above 20 MeV is possible but questionable. Natural copper is composed of two isotopes (69.17% ^{63}Cu and 30.83% ^{65}Cu) and therefore has competing reactions must be considered.

Nickel has two commonly used reactions for activation analysis (^{58}Ni(n,2n) and ^{58}Ni(n,p)). The use of nickel foils for measuring fast neutron reaction rates is outlined in ASTM Standard Test Method E 264-08 [31]. Natural nickel is 68.08% ^{58}Ni and four other isotopes, so competing reactions are an issue. Nickel foils have been used at several

facilities for measuring neutron spectra [32–34].

Aluminum is naturally monoisotopic and possesses two usable threshold reactions (^{27}Al(n,α) and ^{27}Al(n,p)). ASTM Standard Test Method E 26611 [35] explains the use of aluminum activation for measuring fast neutron reaction rates. The half-life of ^{24}Na (14.95 hours) and the relatively high reaction cross section of ^{27}Al(n,α) make aluminum an ideal activation detector of fast neutrons. Aluminum foils have been used for this purpose [22, 27, 32].

In addition to the four types of foil that were available immediately, several others were purchased. These included disks of cobalt, gold, indium, iron, and titanium, 1 cm in diameter.

Cobalt has reaction thresholds above 20 MeV, which overlap bismuth reaction cross sections. Cobalt is monoisotopic ^{59}Co and the (n,xn) reactions produce products with half-lives in the range of days. Cross section data for these reactions have been measured in the range of 15–40 MeV [36] and in the range of 40–120 MeV [30]. Cobalt foils have been used for high-energy neutron spectrometry [26, 27], and also in the fast-energy range [22, 33, 34]. Because nickel (atomic number $Z = 28$) and cobalt ($Z = 27$) are separated by one proton, their reaction products overlap. For this reason, some nickel and cobalt activities should not be measured simultaneously.

Gold is the foil material of choice for measuring thermal flux, but it can also be used in the high-energy range. Gold is naturally monoisotopic ^{197}Au and possesses a few (n,xn) reactions with thresholds above 20 MeV. These reactions have been used for high-energy flux spectrum measurements [26]. Gold also has one useable reaction ^{197}Au(n,2n) with a threshold below 20 MeV. There are several reported measurments with gold in this energy range [27, 28, 37].

The indium ^{115}In(n,n') reaction has an unusually low threshold (0.355 MeV) so it is useful for determining the flux below 1 MeV. Indium is 95.71% ^{115}In, but the other isotope ^{113}In does not produce the ^{115m}In reaction product, so competing reactions are not a concern. Indium has been used both as an epithermal activation foil [25, 32], and as a threshold reaction foil [34].

Iron has been employed as a fast neutron activation foil [22, 28, 33]. Natural iron is composed of four isotopes, but is 91.75% ^{56}Fe. The ^{56}Fe(n,2n) reaction would be

useful, but the product ^{55}Fe is a pure beta emitter so it cannot be detected by gamma spectrometry. Iron has two threshold reactions (^{54}Fe(n,p) and ^{56}Fe(n,p)) with usable half-lives. The use of iron in determining fast neutron reaction rates is guided by the ASTM Standard Test Method E263 - 09 [38].

Titanium foils used for fast measuring neutron reaction rates is outlined by ASTM Standard Test Method E526 - 08 [39], and titanium foils have been used to this purpose [22,28,34]. Three natural isotopes of titanium (^{46}Ti, ^{47}Ti, ^{48}Ti) have (n,p) reaction cross sections that cover the range of 2–20 MeV.

Cadmium is not used as an activation foil, but its unique neutron absorption behavior makes it useful for activation measurements. Cadmium is an effective absorber of neutrons below some energy E_c but it passes neutrons of energies above E_c. E_c is known as the "effective cadmium cut-off energy," and for a 1 mm thick cadmium shield in an isotropic neutron field, it may be taken to be about 0.55 eV. The use of cadmium shielded foils is convenient in separating contributions to the measured activity from thermal and epithermal neutrons. Also, cadmium shielding is helpful in reducing activities due to impurities and the loss of the activated nuclide by thermal-neutron absorption [40].

3.3   Gamma Spectrometer

3.3.1   Ortec PopTop

The gamma-ray detector used in this work is an Ortec coaxial P-type High Purity Germanium (HPGe) GEM25P4 PopTop model. The manufacturer claims the useful range for this model is ∼40 keV–10 MeV, the relative efficiency is ≥ 25%, the peak-to-Compton ratio is 56:1, and the full-width half-max (FWHM) resolution is 0.82 keV at 122 keV and 1.85 keV at 1.33 MeV [42]. The PopTop detector has a 70 mm diameter cylindrical aluminum end cap window of 1 mm thickness, and a bulletized (rounded corners) cylindrical P-type germanium crystal 59 mm in diameter and 54.9 mm in length. The crystal has a 700 μm lithium contact layer on the outside, and a 0.3 μm boron contact layer inside a coaxial bore hole [43]. The PopTop detectors are detachable, and once warmed to room temperature, they can be reconfigured with different liquid nitrogen (LN2) dewars (Figure 3.2).
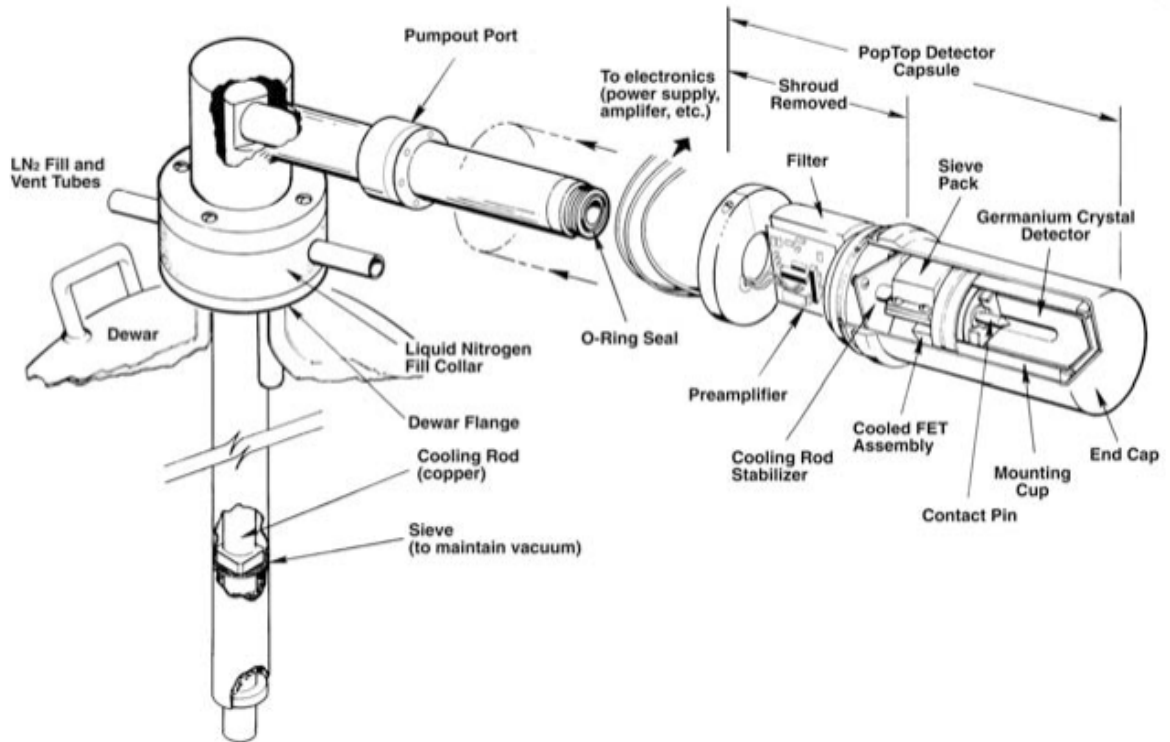
Figure 3.2: Diagram of the Ortec PopTop detector and LN2 dewar [41]. This illustration shows the detector mounted horizontally at a 90° angle, while the actual detector was mounted vertically.

3.3.2   Electronics and Software

Many modern gamma-ray spectrometry systems use integrated power electronics and a computer for data acquisition. The electronics used for this work include an Ortec Digi-DART portable digital MCA with DIM-POSGE Detector Interface Module (DIM). The DIM uses a 13-pin power/signal cable to connect to the DigiDART, and a 9-pin pre-amplifier power cable along with BNC coaxial cables to connect to the detector. The BNC cables provide high voltage (HV), pre-amplifier output signal, and a bias shutdown signal. The DigiDART portable MCA interfaces with a computer via a USB cable. By using a rechargeable battery, the DigiDART will continue to read from and provide HV to the detector if the computer crash or loose power.

The computer runs the Windows operating system and uses the GammaVision-32 software. Through GammaVision-32, many electronics settings can be adjusted, includ-

Figure 3.3: Graded lead shield with copper liner above the 30 L LN2 dewar.

ing HV level, amplifier gain, pulse shaping, and pole-zero cancellation. GammaVision-32 is capable of energy and efficiency calibrations, analysis of spectra including corrections and the use of libraries for identification, and storing spectra in data files for offline analysis. The software also uses a simple programing language for automating repetitive tasks. GammaVision-32 is the primary software used spectral analysis in this work, but custom programs written in the Scientific Python (SciPy) programing language are also used.

3.3.3 Graded Shield

Background radiation from natural sources, such as ^{40}K and radon daughter products, is omnipresent. Radiation from these sources can be reduced by surrounding the gamma-ray detector with a shield, but the shield itself can also act as a source. Lead is often the gamma-ray shielding material of choice. Photoelectric absorption of gamma-rays in lead produces X-ray fluorescence, which can disrupt the gamma-ray spectrum near 80 keV. A few millimeters of copper added to the inside of a lead shield will absorb the lead X-rays.

While copper itself produces fluorescence X-rays, these are in the range of 8–9 keV are below the range of interest for gamma spectrometry. The use of layers of materials to shield primary and secondary radiation is known as a graded shield.

The graded shield used for this work was produced by a now defunct company called Nuclear Data. The shield consists of a 24 cm diameter cylindrical cavity 30 cm tall with coper lining (3 mm) inside 10 cm of lead with a two piece lead lid of the same thickness. At the base of the shield is a 7.6 cm diameter hole through which the gamma-ray detector penetrates the cavity. The entire shield is on a stand 75 cm high. The LN2 dewar underneath the stand rests on ∼0.6 cm of steel to shield the base of the detector from the concrete floor (see Figure 3.3).

3.3.4 Liquid Nitrogen LN2 Dewars

Two LN2 dewars were used with this work. The first was an Ortec Gamma Gage cryostat with 7 L Multi-Orientation Dewar. The dewar allowed for semi-portable usage of the gamma-ray spectrometer, but the 7 L capacity only allowed for maximum count times of 2.5 days. The 7 L dewar could not be refilled while in the shield, and once the geometry was disrupted new calibrations were required.

The low capacity of the 7 L dewar lead to the purchase of an Ortec 30 L dewar with cold finger. This can be refilled online (while counting) and has a LN2 capacity that lasts approximately 10 days (see Figure 3.3).

3.3.5 Calibration Sources

Gamma-ray spectrometers must be regularly calibrated. Energy calibration can be done with any known source and its well documented emission spectrum. The activity of the source need not be known. Efficiency calibration is more complicated. Efficiency takes into account the source-to-detector geometry, so a particular calibration is only valid for its geometry. Calibration of efficiency also requires precise information about a source's activity at a specific time. This information can be used with the exponential decay law to determine the source activity during the calibration.

Calibration sources are commercially available. They typically include certified

Figure 3.4: Calibration source used for spectrometer energy and efficiency calibrations.

measurements of their activities and their uncertainties. A set of eight sources (^{22}Na, ^{54}Mn, ^{57}Co, ^{60}Co, ^{109}Cd, ^{133}Ba, ^{137}Cs, and a multinuclide) purchased from Eckert & Ziegler Isotope Products Laboratories were used for this work. The sources were ~1 μCi with single and multiple peaks that spanned a range of typical energies (88–1836 keV).

3.3.6 Sample Holder

Since efficiency is dependent on source-to-detector geometry, it is important to maintain the same geometry during calibration as during measurement. This can be done with a sample holder. Presumably sample holders are commercially available, although none were found. A sample holder was designed and fabricated to meet the needs of this foil irradiation work.

The sample holder consists of a base, two slotted walls, sample trays, and support rods (see Figure 3.5). The base mounts to the detector end cap with thumb-tightened nylon screws. The slotted walls allow sample trays to be loaded at various heights above the top of the detector. Two of the trays were designed to be used in conjunction. The calibration tray locates the calibration sources centered at the same positions as the foil tray. Due to the radial symmetry of some of the 21 foil locations, only five calibration locations are required. The trays have ridges and grooves that colocate the vertical axis midpoint of the calibration source with a 1 mm thick foil. A third tray that includes a radial locating

42
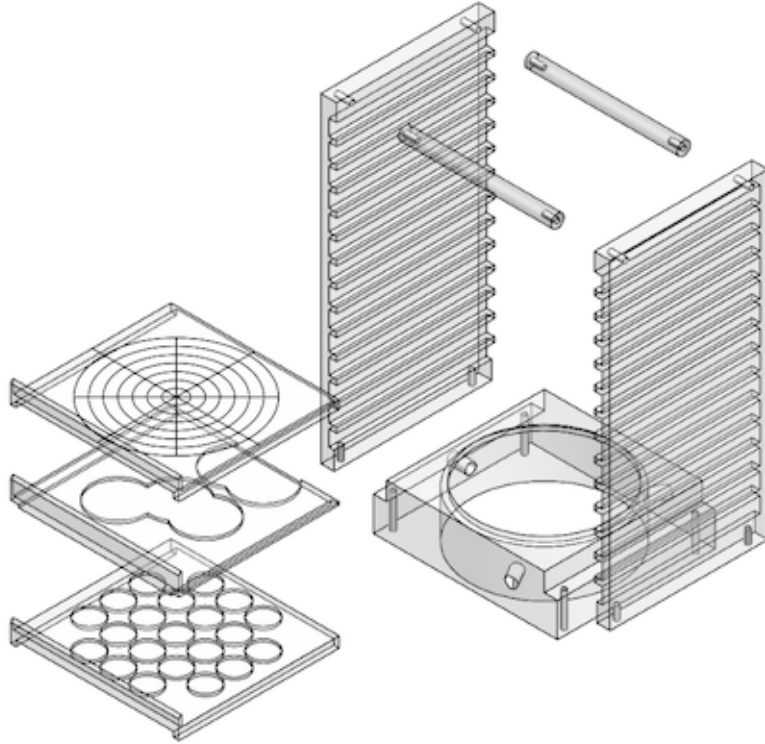
Figure 3.5: Exploded view of plastic sample holder designed and fabricated for this work.

pattern was designed for the possibility of irregularly shaped samples. The entire sample holder is constructed out of clear plastic because high-Z materials attenuate gamma-rays, and metals often include radioactive trace elements.

Chapter 4

Computational Tools

This chapter explains the computational tools used to develop the high-energy flux spectra measurement method at the Spallation Neutron Source (SNS). Suitable nuclear data libraries are also discussed. In addition to the GammaVision-32 software used for data acquisition, two major software packages and several custom programs were used for routine calculations.

4.1 Nuclear Data

4.1.1 ENDF

The standard nuclear data used in the United States come from the Evaluated Nuclear Data File (ENDF), the most recent version of which is the ENDF/B-VII.0 version [44]. Published in December 2006, ENDF/B-VII.0 contains data primarily for reactions with incident neutrons, protons, and photons on almost 400 isotopes, based on experimental data and theoretical predictions.

The standard ENDF library extends up to 20 MeV for incident neutron data. The ENDF/B-VI.6 library released in 1996, included extensions up to 150 MeV maximum energy for about 40 neutron and 40 proton reactions on certain target isotopes, supporting spallation neutron source design and other applications. These extensions were the LA150 library. The higher energy cross section data were based upon measurements and on GNASH nuclear model code predictions. Unfortunately, a bug was later found in
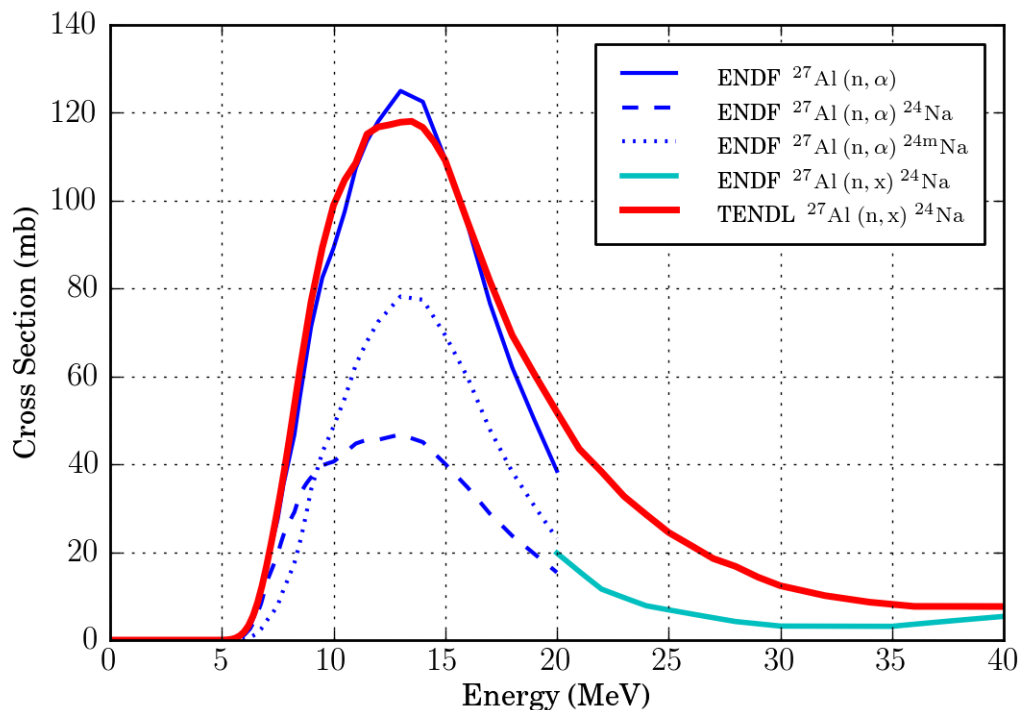
Figure 4.1: Reaction cross section data for ^{27}Al. Note the discontinuities at 20 MeV for the ENDF/B-VII.0 data, which are not present in the TENDL-2010 data.

the GNASH code that was used to predict secondary emitted particle production. For ENDF/B-VII.0 the high energy LA150 data was recalculated and updated with newly corrected results.

Even with the extended energies, ENDF libraries present several issues that make high-energy activation calculations difficult. The byzantine structure of ENDF files (known as ENDF-6 format) are a legacy from an era when data storage was costlier and scarcer than it is today. Consequently, neutron induced reaction cross sections are stored in multiple formats that must be recombined before they are used. For energies less than 20 MeV these reaction cross sections are stored in one format (called "File 3" in ENDF terms), while above 20 MeV they are stored in a different format ("File 5"). The different formats not only make their simultaneous use cumbersome, the two formats actually represent different physical values. Below 20 MeV, reaction cross sections can be extracted for a specific channel on a specific target, for example ^{27}Al(n, α). Above 20 MeV, reaction cross sections can only

be extracted for a specific *residual* (product), for example ^{27}Al$(n, X)^{24}$Na. The two are not equivalent. The ^{27}Al$(n, X)^{24}$Na cross section includes the $(n, n^3$He$)$ reaction, whereas the ^{27}Al(n, α) cross section does not. Also, the ^{27}Al(n, α) cross section includes the ^{24m}Na residual, whereas the ^{27}Al$(n, X)^{24}$Na cross section does not (Figure 4.1).

Because the reaction cross sections above and below 20 MeV are different, it is not surprising to find a discontinuity in the reaction cross sections at that energy. This is the case for all reaction cross sections that span the artificial 20 MeV boundary, although it is more evident for some cross sections. Above 20 MeV the cross sections are usually calculated, whereas below 20 MeV cross section data primarily comes from evaluating experimental data. No attempt was made to match the ENDF data across the 20 MeV boundary. To quote one ENDF expert regarding the 20 MeV discontinuities, "They are unphysical, but they are OK for particle transport calculations, and that was their original intention [3]." Clearly, the ENDF libraries are less than ideal for high-energy neutron activation calculations.

4.1.2 LA150

As mentioned in Section 4.1.1, the LA150 cross section data have been recalculated and incorporated into the most recent release of the ENDF library. Separate LA150 cross section data are also available for use with MCNPX, so they are briefly mentioned here.

The LA150 library was developed at Los Alamos National Laboratory for proton and neutron reactions up to 150 MeV on high priority nuclides for accelerator driven systems. The upper limit of 150 MeV was chosen partially because it corresponds to the pion production threshold, which is not predicted by the GNASH code. The GNASH nuclear model reaction code was used extensively in the LA150 library to predict nuclear reaction cross sections because measured data at higher energies are relatively sparse. Prior to the LA150 library, the intranuclear cascade model in the LAHET code was used to predict nuclear interactions above 20 MeV. LAHET is most accurate above 150 MeV. In that range, nuclear interactions are less sensitive to specific details of nuclear structure along with quantum effects in the scattering [45].

The LA150 library is in the ENDF-6 format, so it suffers from the same defi-

ciencies that affect the ENDF library. Because the ENDF/B-VII.0 has been corrected and updated, the LA150 library is less useful than the ENDF library, but neither library is ideal for calculating high-energy neutron activation.

4.1.3 LAHET in MCNPX

The LAHET nuclear model code is available for use with the MCNPX software. Nuclear models are used by default in MCNPX when cross section tables are unavailable. Unfortunately, FM and DE-DF cards[1] cannot be used with tallies using the LAHET model. As far as can be determined, this prohibits direct activation calculations in MCNPX using the LAHET code.

4.1.4 TENDL-2010

The TENDL-2010 cross section library is based on calculations by the TALYS 1.2 nuclear reaction simulation code, which uses evaluated data as well as nuclear models. TENDL-2010 cross sections range up to 200 MeV with no artificial boundary or discontinuities at 20 MeV. In the incident neutron sub-library, data are available for the entire range of energies by reaction residual (Figure 4.1). For activation calculations, the most useful data is cross section by residual because ultimately the reaction producing the residual (*i.e.* (n,α) or (n,n^3He)) is inconsequential to the foil activity measurement.

The TENDL cross section data have several other features. TALYS generates libraries that are consistent, complete, and reproducible. TENDL libraries include covariance data. The data are freely available for download in plain text, ENDF-6 format, ACE format (used by MCNPX), and AMPX format. The TALYS-2009 data library was validated with a total of 686 International Criticality Safety Benchmark Evaluation Project (ICSBEP) benchmarks and was found to yield results closer to the experimental values than other libraries (*i.e.* JEFF-3.1 and Japanese Evaluated Nuclear Data Library (JENDL)-3.3) [46]. The validity of TENDL at high energies is less verifiable due to the dearth of experimental data in that range.

---

[1]Commands in MCNPX are referred to as "cards." See Section 4.2.1 for details.

4.1.5 Other Cross Section Data

Other sources of cross section data are briefly mentioned here. These sources were considered, but not used in this work.

The European Activation File (EAF) is an ongoing project to produce data for the European fusion program. Its primary use is activation rather than transport. The EAF-2010 library contains 66,256 excitation functions involving 816 different targets from atomic numbers 1–100 in the energy range 10^{-5} eV–60 MeV [47]. While EAF-2010 is not available outside of fusion research projects, a similar library, EASY-2005.1, is available from the Radiation Safety Information Computational Center (RSICC) [48]. Although EAF is appropriate for activation calculations, 60 MeV is too low to use for SNS high-energy neutron spectrometry.

The Japanese Evaluated Nuclear Data Library (JENDL) high energy file JENDL/HE-2007 was developed to meet the intermediate and high energy nuclear data needs in accelerator-driven transmutation systems, particle radiation therapy, radioisotope production, space development, and other areas. The library extends up to to 3 GeV on 132 priority nuclides. Benchmark tests have been performed to validate the JENDL/HE-2007 since its release, such as deep-penetration of high-energy neutrons in shielding materials, and spallation experiments with high-energy protons. The JENDL/HE-2007 evaluation generally showed good agreement when compared with the other evaluations and experimental data [49]. Due to the high upper energy limit of the JENDL/HE-2007 library, its use in high-energy neutron spectrometry at SNS is appealing. Unfortunately, JENDL/HE-2007 has fewer activation cross sections than the TENDL library, and it suffers from the same 20 MeV artificial boundary issues as the ENDF library.

4.1.6 HILO2k

HILO2k is a coupled neutron-photon high-energy multigroup cross section library. The library was developed for SNS shielding design and other associated radiation transport problems. The library includes data for 32 nuclides, in 83 neutron groups and 22 photon groups ranging up to 2 GeV (Table 4.1). Neutron cross sections above 20 MeV are based on high-energy doubly differential neutron interaction and production data generated with

Group #	Upper Energy MeV	Group #	Upper Energy MeV	Group #	Upper Energy MeV
1	2000	23	350.00	45	14.9200
2	1850	24	325.00	46	14.2000
3	1700	25	300.00	47	12.2100
4	1550	26	275.00	48	10.0000
5	1400	27	250.00	49	8.6070
6	1300	28	225.00	50	7.4080
7	1200	29	200.00	51	6.0650
8	1100	30	180.00	52	4.9660
9	1000	31	160.00	53	3.6790
10	950	32	150.00	54	3.0120
11	900	33	140.00	55	2.4660
12	850	34	120.00	56	2.3460
13	800	35	100.00	57	2.2320
14	750	36	80.00	58	1.8270
15	700	37	70.00	59	1.4230
16	650	38	60.00	60	1.1080
17	600	39	50.00	61	0.8209
18	550	40	40.00	62	0.7427
19	500	41	30.00	63	0.6081
20	450	42	25.00	64	0.4979
21	400	43	19.64	65	0.3688
22	375	44	16.91	66	0.2472

Table 4.1: HILO2k neutron energy groups from 247.2 keV to 2 GeV.

a modified version of MCNPX, while below 2 MeV cross sections are based on ENDF data [50].

The HILO2k cross section libraries cannot be used for the high-energy neutron activation calculations needed for the foil measurements. The significance of HILO2k is its energy group structure, which is the standard group structure for neutron transport calculations at the SNS. The source terms used in MCNPX to calculate beamline fluxes at SNS are expressed using this group structure. As shown in equation 2.48, the flux spectrum that is unfolded from the foil measurements consists of group fluxes over several energy groups. The flux spectrum can be expressed using any energy group structure, but is best to use a group structure well suited to the expected features of the spectrum. Since the HILO2k group structure is already in use at the SNS, this is the group structure that is adopted for this neutron spectrometry work.

4.2 Software

4.2.1 Monte Carlo N-Particle eXtended (MCNPX)

MCNPX is a general purpose Monte Carlo radiation transport code designed to track many particle types over broad ranges of energies [51]. The software is very flexible and capable of modeling many types of radiation transport problems. In this work, MCNPX was used to calculate the response matrix elements, estimate expected reaction rates, and calculate gamma-ray self-shielding of the foils. One of several computer clusters at ORNL were used to process the MCNPX models.

Two primary components are required to perform calculations in MCNPX: a source, and a tally on a material cell. The source can be parameterized by several variables including spatial location, energy, and direction. The material cell can also have various attributes including shape, location, and material composition. MCNPX offers several types of tallies, including the so-called F4 tally which specified as the "track length estimate of cell flux" [52]. The F4 tally is a Monte Carlo estimation of the average flux in a volume $\hat{\phi}_V$:

$$\hat{\phi}_V = \frac{1}{V} \int dE \int dt \int dV \int d\Omega \ \Psi(\vec{r}, \hat{\Omega}, E, t) \tag{4.1}$$

where Ψ is the angular flux as a function of position $\vec{r}$, direction $\hat{\Omega}$, energy E, and time t. Each particle that enter the cell scores:

$$Score = W \frac{T_l}{V} \tag{4.2}$$

W is the particle weight, T_l is the particle track length in the cell, and V is the cell volume. Although the F4 tally is typically referred to as a "flux" tally, its actual representation depends on the units of the specified neutron source. If the neutron source is in units of $\frac{\text{particles}}{\text{second}}$, the F4 tally is in units of $\frac{\text{particles}}{\text{cm}^2\text{second}}$ [52].

MCNPX has only a few tally types, but other quantities can be directly computed by using the FM or "Tally Multiplier" card. The FM card is used to calculate any quantity of the form:

$$C \int \phi(E) R_m(E) dE \tag{4.3}$$

where $\phi(E)$ is the energy dependent flux , $R_m(E)$ is an MCNPX specified energy dependent response function, and C is a constant multiplier. For F4 tallies only, if C is negative, C is replaced by $|C|$ times the atom density (units of $\frac{\text{atoms}}{\text{barn}-\text{cm}}$) of the cell where the tally is made. The response function can be a microscopic cross-section σ_m of a particular reaction cross cross-section, for example (n,2n). When the FM card is used with an F4 type tally, the reaction-rate can be computed.

$$\text{Reaction Rate} = N_\rho \times V \int \phi(E)\sigma_m(E)dE \qquad (4.4)$$

where N_ρ is the atomic number density.

Another feature of MCNPX is the DE-DF "Dose Energy - Dose Function" cards. This feature allows the user to input an energy dependent point-wise response function to modify a tally. The DE-DF cards by default are logarithmically interpolated between points, but linear interpolation can be specified.

Two features of MCNPX allow the user to bin the tally by energy. The "Tally Energy" En card allows tallies to be binned by groups of energies of the scoring particles. The "Special Treatment" cards FTn SCX allows tallies to be binned by particle *source energy distribution*. The distinction between these two cards is subtle but important. The En card bins the tally by particle energies where they "score", but the FTn SCX card bins the tally by particle energies how they were "born."

4.2.2 MAXED

Spectral unfolding is done with UMG 3.3. This software includes three main components: the MAXED unfolding program, the GRAVEL unfolding program, and the Integral Quantities Utility (IQU) auxiliary program. The programs were initially used with the Windows operating system and later compiled from Fortran source code for the Mac OSX operating system.

MAXED is the primary unfolding program used for this work. MAXED applies the maximum entropy principle to unfold neutron spectrometric measurements. It was originally written for the unfolding of Bonner sphere data, but later modified to accommodate proton recoil measurements. Advantages of MAXED include:

- it is the only mathematically consistent method of incorporating *a priori* information into the solution;

- it makes use of the estimated variances for each detector's count rate in the unfolding process;

- the algorithm leads to a solution spectrum that is always a non-negative function

- the solution spectrum can be written in closed form [53].

Disadvantages of MAXED, based on the author's personal experience and anecdotal conversations [54], are that the documentation is sparse and the user interface is poor.

When a neutron spectrometry measurement is made, some information is known about both the neutron source and about the physics that govern the neutrons interactions. This *a priori* information, usually derived from calculations or independent measurements, needs to be incorporated into the deconvolution process in a mathematically consistent way. In the language of MAXED, the initial estimate of the spectrum that incorporates all the *a priori* information is called the "default spectrum." The challenge of neutron spectrum unfolding is to take the default spectrum and to modify it as minimally as possible so that it becomes consistent with the measurement data [55]. This minimally modified spectrum that is consistent with the measurements is called the "solution spectrum."

Principle of Maximum Entropy

Derivation of the principle of maximum entropy is beyond the scope of this work, but it is based in part on the "cross entropy" function. Given a probability distribution $p(x)$ and a distribution $q(x)$ the cross entropy S_{CE} is defined as:

$$S_{CE} = - \int q(x) \ln \left(\frac{q(x)}{p(x)} \right) dx \tag{4.5}$$

The cross entropy $S_{CE} \leq 0$ and $S_{CE} = 0$ iff $q(x) = p(x)$. Therefore, the cross entropy has been regarded as a measure of the amount of information required to change $p(x)$ into $q(x)$. Applied to unfolding, the spectrum which maximizes S_{CE} (or minimizes $|S_{CE}|$ since $S_{CE} \leq 0$) for the default spectrum $p(x) = f^{def}$ is the minimally modified solution spectrum $q(x) = f$.

The set of possible solution spectra are defined by two constraints. First, the sum of the solution spectrum f_n elements multiplied by the response matrix elements R_{mn} yields the measurement $\mathcal{M}_m$ within some discrepancy ϵ_m:

$$\mathcal{M}_m + \epsilon_m = \sum_n^N R_{mn} f_n \tag{4.6}$$

This is similar to equation 2.48, where the response matrix was defined. The second constraint is that the discrepancies ϵ_m are bound by some value Ω:

$$\sum_m^M \frac{\epsilon_m^2}{\sigma_m^2} = \Omega \tag{4.7}$$

The value of Ω is chosen by the user in MAXED. In equation 4.7, the discrepancies are squared to be positive and normalized to the standard uncertainty of each measurement σ_m. Setting Ω to the number of detectors M essentially requires that the average uncertainty-normalized discrepancy is equal to 1:

$$\frac{1}{M} \sum_m^M \frac{\epsilon_m^2}{\sigma_m^2} = 1 \tag{4.8}$$

Equations 4.8 and 4.6 state that the discordance between the calculated flux spectrum and the measurements should be the same as the measurement uncertainty on average. It's reasonable that the solution spectrum cannot be more precise than the measurements that were used to determine it.

The solution spectrum satisfies equations 4.7 and 4.8, and maximizes the entropy described by equation 4.5:

$$S = -\sum_n^N \left(f_n \ln \left(\frac{f_n}{f_n^{Def}} \right) + f_n^{Def} - f_n \right) \tag{4.9}$$

Equation 4.9 is a more general form of 4.5 with two additive terms. The addition of f_n^{Def} ensures that the global maximum of S is zero, which is convenient but not necessary. The subtraction of f_n ensures that in the absence of any other constraints, when S is maximized, $f_n = f_n^{Def}$ rather than just being proportional [55].

Equation 4.9 can be maximized using the calculus of variations and Lagrange multipliers λ_m. Using this technique, solving for the the solution spectrum and the discrepancies yields:

$$f_n = f_n^{DEF} \exp\left(\sum_m^M \lambda_m R_{mn}\right) \tag{4.10}$$

$$\epsilon_m = \frac{\lambda_m \sigma_m^2}{2}\left(\frac{4\Omega}{\sum_m^M (\lambda_m \sigma_m)^2}\right)^{1/2} \tag{4.11}$$

Equations 4.10 and 4.11 show that the solution spectrum and the discrepancies can be expressed in terms of the default spectrum, known parameters, and Lagrange multipliers in closed form. This is different from other iterative techniques where a solution is expressed in terms of the previous iteration. Equations 4.10 and 4.11 allow for straightforward propagation of errors and sensitivity analysis that is not possible with other iterative solutions.

The maximization of the entropy in equation 4.9 is equivalent to maximizing a potential function $\mathcal{Z}$:

$$\mathcal{Z} = -\sum_n^N f_n^{Def} \exp\left(-\sum_m^M \lambda_m R_{mn}\right) - \left(\Omega \sum_m^M (\lambda_m \sigma_m)^2\right)^{1/2} - \sum_m^M \mathcal{M}_m \lambda_m \tag{4.12}$$

In equation 4.12, the f_n^{Def}, R_{mn}, $\mathcal{M}_m$, σ_m and Ω are specified as input values. For any chosen λ_m values, $\mathcal{Z}$ can be evaluated. Therefore, to find the global maximum $\mathcal{Z}$, the space of all λ_m must be sampled methodically. This is accomplished using the Simulated Annealing (SA) algorithm.

Simulated Annealing (SA)

Simulated annealing is analogous to the physical cooling of materials. When some materials are allowed to cool slowly, they form large crystals billions of times larger than the constituent atoms. The crystal is global minimum of energy for the system, and it forms because the atoms are allowed to redistribute themselves as they lose energy. If the material is cooled rapidly, a local minimum is reached, but not necessarily a global minimum. Nicholas Metropolis and his colleagues incorporated the physical principles of annealing

into numerical calculation. Metropolis algorithms such as SA allow for redistribution out of local extrema by probabilistically selecting best estimates using an artificial temperature function [56].

As used in MAXED, the SA algorithm randomly chooses a trial point $(\lambda_1^i, \lambda_2^i, ..., \lambda_N^i)$ within some step length of the starting point. If the potential function in equation 4.12 evaluates to a larger value, the "uphill" trial point is always accepted as the new best estimate. If the potential function evaluates to a lower value, the "downhill" trial point is accepted with a probability $p(T)$ as a function of artificial temperature. The lower the temperature, the less likely downhill points will be accepted. The process iterates, and a new random trial point $(\lambda_1^{i+1}, \lambda_2^{i+1}, ..., \lambda_N^{i+1})$ some step length from the current best estimate is again evaluated. After a number of random trials at a given temperature, the artificial temperature will decrease according to a cooling schedule. At the lower temperature, the step length decreases as does the probability $p(T)$. SA is able to move out of local maxima, but as it progresses, it samples from the most promising region of the space.

The SA algorithm used by MAXED is a modification of the `SIMANN.F` program [57]. Many of the parameters of the SA algorithm were optimized by the MAXED authors. The user sets the initial temperature and a temperature reduction factor. The optimal initial temperature depends on the particular problem. The MAXED authors recommend selecting an initial temperature high enough such that no new maxima are found in the first set of iterations at constant temperature, noting that 1000 is typically large enough [55]. In practice, this has not always been achievable. Some unfoldings with MAXED have shown 1 new maximum in the first iterations at constant temperature even for temperatures as high as 10^{25}. The reason this occurs is not known, but it could be due to a bug in the program. In these cases, the initial temperature is selected when it is high enough such that < 2 new maxima are found initially. In each step of the cooling schedule, the temperature reduction factor RF is applied such that $T_{new} = RF \times T_{old}$. A temperature reduction factor of 0.85 is recommended by the MAXED documentation and was used for all unfoldings.

4.2.3 GRAVEL

The GRAVEL algorithm was not used extensively for this work, but is explained here briefly to contrast against MAXED. GRAVEL is an extension of the SAND-II algorithm [58]. SAND-II assumes an estimate of the flux, and for subsequent iterations applies a nonlinear adjustment [8]. Given an element of a discretized flux spectrum f_n^j for iteration j, the flux for iteration $j + 1$ is defined as:

$$f_n^{j+1} = f_n^j \exp \left(\frac{\sum_n^N W_{mn}^j \ln \frac{\mathcal{M}_m}{\sum_m^M R_{mn} f_n^j}}{\sum_n^N W_{mn}^j} \right) \tag{4.13}$$

$$W_{mn}^j = \frac{R_{mn} f_n^j}{\sum_n^N R_{mn} f_n^j} \frac{\mathcal{M}_m^2}{\sigma_m^2} \tag{4.14}$$

The default spectrum is used for the first iteration. Given a non-negative default spectrum, the solution spectrum will always be non-negative. Because equation 4.13 is not written in closed form similar to equation 4.10, the same uncertainty propagation and sensitivity analysis that is used with MAXED cannot be used with GRAVEL [59].

4.2.4 Integral Quantities Utility (IQU)

The IQU program calculates the uncertainty in the solution spectrum Δf^{Meas} due to the uncertainty in the measurements, the uncertainty in the solution spectrum Δf^{Def} due to the uncertainty in the default spectrum, and the total uncertainty Δf^{Total} in the solution spectrum due to both uncertainties. The $N \times N$ uncertainty matrix $\mathbf{U^{Meas}}$ for the solution spectrum due to the uncertainty in the measurements is:

$$\mathbf{U^{Meas}} = \frac{\delta \mathbf{f}}{\delta \mathbf{M}} \mathbf{K^{Meas}} \left(\frac{\delta \mathbf{f}}{\delta \mathbf{M}} \right)^T \tag{4.15}$$

where $\mathbf{K^{Meas}}$ is the $M \times M$ measurement covariance matrix, $\frac{\delta \mathbf{f}}{\delta \mathbf{M}}$ is the $N \times M$ sensitivity matrix, and $\left(\frac{\delta \mathbf{f}}{\delta \mathbf{M}} \right)^T$ is the $M \times N$ transpose of the sensitivity matrix. Similarly, the $N \times N$ uncertainty matrix $\mathbf{U^{Def}}$ for the solution spectrum due to the uncertainty in the default spectrum is:

$$\mathbf{U^{Def}} = \frac{\delta \mathbf{f}}{\delta \mathbf{f^{Def}}} \mathbf{K^{Def}} \left(\frac{\delta \mathbf{f}}{\delta \mathbf{f^{Def}}} \right)^T \tag{4.16}$$

where $\mathbf{K^{Def}}$ is the $N \times N$ default spectrum covariance matrix, $\frac{\delta \mathbf{f}}{\delta \mathbf{f^{Def}}}$ is the $N \times N$ sensitivity matrix, and $\left(\frac{\delta \mathbf{f}}{\delta \mathbf{f^{Def}}} \right)^T$ is the $N \times N$ transpose of the sensitivity matrix. The total uncertainty $\mathbf{U^{Total}}$ is just the sum of the two uncertainty matrices:

$$\mathbf{U^{Total}} = \frac{\delta \mathbf{f}}{\delta \mathbf{M}} \mathbf{K^{Meas}} \left(\frac{\delta \mathbf{f}}{\delta \mathbf{M}} \right)^T + \frac{\delta \mathbf{f}}{\delta \mathbf{f^{Def}}} \mathbf{K^{Def}} \left(\frac{\delta \mathbf{f}}{\delta \mathbf{f^{Def}}} \right)^T \tag{4.17}$$

The group uncertainties are found by multiplying the uncertainty matrices by the solution spectrum:

$$\Delta f^{\text{Meas}} = \mathbf{U^{Meas}} f \tag{4.18}$$

$$\Delta f^{\text{Def}} = \mathbf{U^{Def}} f \tag{4.19}$$

$$\Delta f^{\text{Total}} = \mathbf{U^{Total}} f \tag{4.20}$$

Because the measurements are independent, the measurement covariance matrix $\frac{\delta \mathbf{f}}{\delta \mathbf{M}}$ is assumed to be diagonal with σ_m on the diagonal. For the default spectrum covariance matrix $\mathbf{K^{Def}}$, a diagonal covariance matrix is also assumed. Although a block diagonal matrix may be appear to be justified since the variation in the flux of a particular energy group may be correlated with its adjacent groups, the Unfolding with Maxed and Gravel (UMG) documentation notes:

> ...this approximation is adequate for the case of maximum entropy deconvolution, as can be seen by looking at the mathematical form of the maximum entropy solution. Particular cases using data from measurements show that the off-diagonal elements are 2 or 3 orders of magnitude smaller than the diagonal elements [58].

The "uncertainty" in the default spectrum is input by the user, and is not a true measurement uncertainty, rather it is a *judgement* of the default spectrum's accuracy. The sensitivity matrices are too complicated to present here, but they can be expressed in terms of the solution spectrum, response matrix, and other input parameters in closed form. The sensitivity and uncertainty matrices are computed by the IQU program from the input parameters and the solution spectrum.

The IQU program can also assign uncertainty to any "integral quantity" H of

the form:

$$H = \sum_n^N h_n f_n \tag{4.21}$$

For example, the integral quantity H could be the dose, and h_n could be a group-wise flux-to-dose conversion factor. The uncertainty in the integral quantity ΔH is given by:

$$\Delta H = \sqrt{\sum_{i,j} h_i U_{ij} h_j} \tag{4.22}$$

4.2.5 Other Unfolding Methods

Several methods of deconvolution have been applied to neutron flux spectrum unfolding. These methods are briefly noted here. A comparison of different unfolding techniques found that some algorithms are perform better in different energy regimes, perform better with different initial spectra, can combine different methods of detection, and are computationally faster [60].

Neural Networks are algorithms for cognitive tasks, such as learning and optimization, which are loosely based on concepts derived from brain research. They simulate a highly interconnected, parallel computational structure with many individual processing elements, or neurons. These networks learn through an iterative process of adjustments using training sets. After a network has been trained, it operates on input data to produce new output. Neural Networks have been used to unfold Bonner sphere data [61, 62], and foil activation data [34].

Genetic algorithms mimic natural evolution by "breeding" candidate solutions. Random breeding occurs over many generations with a bias toward "high-fitness" candidate solutions. When solutions breed, they exchange components to produce offspring solutions, and then they are "killed off" to maintain a constant population size. After many generations of breeding, the fittest solutions are expected to have survived. Genetic algorithms have been used to unfold neutron spectra from Bonner sphere data [63, 64].

The BUNKI code is based on the BON algorithm, which applies the transpose of the response matrix to both sides of equation 2.48 to determine a physically relevant solution iteratively. The solution is not sensitive to initial guess, so it is best used when *a priori* information in insufficient [65]. Due to this insensitivity, the BUNKI code was

favored when compared to the MAXED code in unfolding Bonner spheres [66]. This algorithm is similar to the SAND-II algorithm and the results obtained by the two codes have been found to be nearly identical [67].

Gold's algorithm, also known as the ratio method, requires no *a priori* information. The measured data and the response matrix can be used to create an initial approximation, which is further iteratively refined. The algorithm is implemented in the SAYD code, which was found to agree well with other codes in a computational benchmark [68].

The Monte Carlo method can also be applied to neutron spectrum unfolding as well as neutron transport. A large number of spectra are generated randomly and the response fitting errors are calculated. The mean value of the best few solutions is used to smooth statistical fluctuations [69]. This method is regarded as time consuming, but can be used for parameter estimation in cases where other techniques fail [70].

The code MINUIT has used a multi-parameter function minimization routine for the unfolding of activation foil data. A fast breeder reactor neutron spectrum was unfolded using the MINUIT code and a set of experimental activation rates without a guess solution. The solution was found to be in good agreement with measured reaction rates. The output spectrum was less dependent on the cross-section variations of the activation foil detectors, a unique advantage [71].

4.2.6 Custom Programs and Additional Software

Several custom programs were written by the author to streamline the data analysis process. A brief description of each program follows.

- `get_tally_files.pl` - A Perl script written to parse the MCNPX output file for the relevant information and then output the information to freely formatted text files usable by `UMG_MakeFiles`.

- `UMG_MakeFiles` - A Fortran-90 compiled executable that writes three files used as input to the MAXED program. MAXED requires strictly formatted Fortran-style input text files. Experience has shown that formatting these files "by-hand" is extremely tedious. `UMG_MakeFiles` uses the output files of the `get_tally_files.pl`

script and a text file containing the default spectrum (one energy group to a line, whitespace delimited) to produce the `.IBU`, `.FLU`, and `.FMT` files.

- `PowerIntegrator.py` - A python program written to read a formatted text file containing beam power data and a file containing decay constants, and then integrate over a time range to compute the beam correction factors (Section 4.3.4).

- `FLU_Metrics.py` - A python program that compares two `.FLU` (MAXED flux spectrum) files and calculates four metrics based upon their differences. The four metrics are the ℓ_1 or "taxi-cab" norm, the Euclidean norm, the average relative difference, and an absolute difference dose norm. The absolute difference dose norm uses flux-to-dose conversion factors contained in a text file (Section 5.1.3).

- `diffPlotter.py` - A python program that produces three plots comparing two `.FLU` files. The first plot is both flux spectra on the same scale, the second plot is the absolute difference between the two, and the third plot is the relative difference between the two.

- `GVAssembler.py` - A python program that takes multiple `.SPE` (GammaVision-32 ASCII formatted spectrum) files and assembles them into a single file. The program sums the counts in each channel and accounts for the difference between start and stop times by adding the difference to the total dead time.

- `XS_Plotter.py` - A python program that takes an ASCII formatted cross section file and plots the data. The program also reads an energy group file and finds the group-averaged cross section for each energy group.

- `SiSp_plotter.py` - A python program that plots Si-Sp ("Source Information - Source Probability") cards from MCNPX. This is useful to visualize MCNPX input such as source energy distributions.

Additional software has been used to do some analysis. Prior to using SciPy, OriginLab was used for some plotting. Matlab had been used to do some initial investigations of the gamma-ray spectrum. Microsoft Excel spreadsheets are used for simplified

quick estimates and some data storage. ImageJ was used to do image analysis of autoradiographs.

4.3 Application of Software to Specific Problems

4.3.1 Estimating of Foil Activity Using MCNPX and Other Tools

Calculating expected results before executing an experiment is prudent. Foil activity calculations help to estimate type and number of foils, the irradiation time, the counting time, and other important parameters. To estimate foil activity, two methods were used: a cursory calculation using a spreadsheet, and a detailed calculation using MCNPX.

The first step of the cursory calculation is to get average group cross-sections from the continuous cross sections. Continuous reaction cross sections are available for download in plain text from the TENDL website. Using the HILO2k group structure and the custom `XS_Plotter.py` program, group averaged cross sections σ_n are computed quickly. Multigroup source terms that SNS staff have calculated are available [2]. To find the flux at a beamline sample location ϕ_n, MCNPX can be used with a flux tally, or a simple $1/r^2$ factor can be applied, where r is the source to sample distance. It may also be necessary to scale the source term by a beam power factor. The multigroup fluxes and the multigroup cross sections can be multiplied group by group along with the number of target nuclei N_i in the foil to produce a reaction rate

$$\text{Reaction Rate} = N_i \sum_g^G \phi_g \sigma_g \tag{4.23}$$

This can be used to calculate the activity at the end of the irradiation, which depends on the irradiation time t_0 and the decay constant λ:

$$A(t_0) = \left(1 - e^{-\lambda t_0}\right) N_i \sum_g^G \phi_g \sigma_g \tag{4.24}$$

The total number of counts C for a gamma-ray of energy E_γ is calculated during the count

time, which occurs between t_{start} and t_{stop}:

$$C(t_{\text{start}}, t_{\text{stop}}) = I_\gamma \epsilon(E_\gamma) \frac{\left(e^{-\lambda t_{\text{start}}} - e^{-\lambda t_{\text{stop}}}\right)}{\lambda} \left(1 - e^{-\lambda t_0}\right) N_i \sum_g^G \phi_g \sigma_g \qquad (4.25)$$

where I_γ is the gamma emission probability, and $\epsilon(E_\gamma)$ is the spectrometer efficiency. Equation 4.25 is similar to equation 2.19, but equation 4.25 does not account for gamma-ray self-shielding. The following equation is used to estimate the Relative Standard Error (RSE) of the count:

$$\text{RSE} = \sqrt{\frac{1}{C}} \qquad (4.26)$$

Equations 4.26 and 4.25 can be used to make decisions about the number of foils, the irradiation time, the counting time, and other parameters.

The detailed calculation uses MCNPX. Foil geometry and orientation can be modeled at the sample location and the source can be modeled using the SNS source terms. The reaction rates can be calculated by using an $F4$ tally on each foil cell along with an FM multiplier card, where the reaction cross section is the response function and the constant multiplier accounts for the number of foil nuclei and units conversions. The MCNPX calculation uses the continuous energy cross sections and accounts for changes in the flux in the foils (self-shielding). A more accurate result is obtained by calculating equation 4.4 instead of equation 4.23. This result can be substituted into equations 4.24 through 4.26 to obtain more accurate count estimates. The cursory method works well for scoping calculations and quick estimates, while the detailed calculation should be used when modeling actual experimental data.

4.3.2 Calculation of Response Matrix Elements Using MCNPX

MAXED solves the inverse problem of equation 4.6, which is to say that given the $\mathcal{M}_m$ and the R_{mn}, the f_n are determined. As stated in Section 2.4, it is convenient to express the $\mathcal{M}_m$ as the reaction rate during irradiation:

$$\mathcal{M}_m = \int_{E_{\text{min}}}^{E_{\text{max}}} N_i \sigma(E) \phi(E) dE \qquad (4.27)$$

Combining (4.27) with the definition of $\mathcal{M}_m$ in equation (2.44), the energy dependent response function $R(E)$ is determined:

$$R(E) = N_i\sigma(E) \tag{4.28}$$

Using the definition of R_{mn} in equation (2.45), the response matrix elements are determined by:

$$R_{mn} = \frac{\int_{E_n}^{E_{n+1}} N_i\sigma(E)\phi(E)dE}{\int_{E_n}^{E_{n+1}} \phi(E)dE} \tag{4.29}$$

This is just the group reaction rate divided by the group flux, which conforms to the original definition of the response function $R = \mathcal{M}/\phi$ from equation 2.43. As explained in Section 4.3.1, the reaction rate for each foil m can be calculated in MCNPX using $F4$ tallies and FM tally multiplier cards. These results can be binned by energy group n using the FTn SCX special treatment card. The response matrix elements are calculated when these $m \times n$ MCNPX results are each divided by the appropriate group flux, which can be done post-processing. This is final step is done with the custom program get_tally_files.pl.

Calculation of the response matrix elements from equation 4.29 appears straightforward, but unfortunately the R_{mn} are defined in terms of the *unknown* flux $\phi(E)$. An estimate of the flux must be used, and an appropriate estimate is the default spectrum to be used by MAXED. Once the new solution spectrum is found, that solution spectrum can be used to recompute the response matrix, and further unfoldings can be performed iteratively to refine the solution [67].

Sensitivity of the Response Matrix to Flux

In practice, the response matrix is not very sensitive to differences in the flux used to calculate it. The N energy groups should be defined such that the flux is approximately constant across each group, so equation 4.29 can be approximated by:

$$R_{mn} \approx \frac{\int_{E_n}^{E_{n+1}} N_i\sigma(E)dE}{E_{n+1} - E_n} \tag{4.30}$$

Equation (4.30) can be rewritten in more intuitive forms:

$$R_{mn} \approx N_j \frac{\int_{E_n}^{E_{n+1}} \sigma(E) dE}{E_{n+1} - E_n}$$

$$R_{mn} \approx N_j \; {}^{\mathrm{n}}\overline{\sigma} \tag{4.31}$$

$$R_{mn} \approx {}^{\mathrm{n}}\overline{\Sigma} V \tag{4.32}$$

where ${}^{\mathrm{n}}\overline{\sigma}$ is the average microscopic reaction cross section for group n, ${}^{\mathrm{n}}\overline{\Sigma}$ is the average macroscopic reaction cross section for group n, and V is the volume of the foil. Equation 4.31 is commensurate with equation 4.28 and is a good approximation of R_{mn}. But even if the flux were exactly constant across each group, equation 4.31 would fail to be exact because the effect of the foil thickness has not yet been considered.

Accounting for Neutron Self-Shielding

Ideally, a foil material and thickness is chosen such that it does not significantly disturb the flux. A single thin foil approximates the ideal situation, but sometimes a foil is not thin or multiple foils are layered into a thick foil packet. Due to its finite thickness and cross section, the front of a foil will slightly shield the rear of a foil from neutrons. To account for this neutron self-shielding, a distinction is made between the flux in the foil $\phi_{Foil}(E)$ and the flux at the sample location in the absence of the foil $\phi(E)$.

$$^{\mathrm{Foil}}R_{mn} = \frac{\int_{E_n}^{E_{n+1}} N_j \sigma_j(E) \phi_{Foil}(E) dE}{\int_{E_n}^{E_{n+1}} \phi(E) dE} \tag{4.33}$$

MCNPX computes $\phi_{Foil}(E)$ when foil materials are specified. When the materials are "voided," MCNPX computes $\phi(E)$. The flux in the foil $\phi_{Foil}(E)$ depends on thickness and the ordering of the foils, while $\phi(E)$ does not. For a given beamline, it is sufficient to compute $\phi(E)$ once, while $\phi_{Foil}(E)$ will need to be recomputed for any change in the foil configuration. Using the approximation of constant flux across energy groups, equation 4.33 becomes:

$$^{\mathrm{Foil}}R_{mn} \approx \left(\frac{\phi_{\mathrm{Foil}}}{\phi} \right) N_j \, {}^{\mathrm{n}}\overline{\sigma} \tag{4.34}$$

Equation 4.34 has an additional flux-dependent factor, as compared to 4.31. This term can be considered the neutron self-shielding factor. In summary, equation 4.33 with the default spectrum is used to calculate the response matrix elements in MCNPX, but equation 4.31 provides a good approximation which can be used to check the MCNPX output for reasonableness.

4.3.3 Calculation of Gamma-ray Self-Shielding Using MCNPX

Just as neutrons are attenuated as they propagate through the foil, so are the gamma-rays which emanate from the foil. Generally, gamma-ray self-shielding is a greater effect in a foil than is neutron self-shielding. The effect of a millimeter of high-Z (atomic number) material can be significant, especially for softer gamma-rays.

To calculate the gamma-ray self shielding effect, foils of various geometry and material are modeled in MCNPX. The gamma-ray source is specified to originate from the bulk of the foil using a single energy. An enveloping surface, such as a sphere, surrounding the foil is used to tally the particle current (an $F1$ tally). By default, tallies are in units of per source particle. When this tally is binned by energy using the En card, the uncollided particle current is distinguished from the collided current. The gamma-ray self-shielding factor is the uncollided current tally. Several runs over a range of gamma-ray energies will produce several points which can be interpolated for an approximate gamma-ray self-shielding function $F_\gamma(E)$.

4.3.4 Correcting for Time-Varying Flux

For a neutron flux that varies with time, such as when accelerator power changes from one minute to the next, the activation rate is not constant. Two important relationships simplify the analysis of this scenario. First, the magnitude of the flux changes with time, but the energy distribution does not. This is equivalent to saying the energy-time dependence of the flux $\phi(t, E)$ is separable:

$$\phi(t, E) = \mathcal{F}(t)\ \phi(E) \tag{4.35}$$

The $\mathcal{F}(t)$ is the time-dependent magnitude of the flux $\phi(E)$. These variables can be separated because the underlying physical processes that generate the neutrons do not change when the beam power changes. The energy spectrum of neutrons is determined by the spallation and moderation processes. When the beam power increases or decreases, there are more or less of these processes occurring, but the processes themselves are unchanged, therefore the energy component of the spectrum is unchanged with beam power.

The second relationship is that the time-dependent magnitude of the flux $\mathcal{F}(t)$ is linearly proportional to the beam power $P(t)$:

$$\mathcal{F}(t) = k \ P(t) \tag{4.36}$$

where k is some yet undetermined scalar constant with units of $\left[\frac{1}{\text{power}}\right]$. Equations (4.35) and (4.36) can be combined into:

$$\phi(t, E) = k \ P(t)\phi(E) \tag{4.37}$$

Using this time-dependent definition of the flux, the change in the number of nuclei N_i due to the production, destruction, and decay processes is:

$$\frac{dN_i(t)}{dt} = \quad \text{production} \quad - \quad \text{destruction} \quad - \quad \text{decay}$$
$$\frac{dN_i(t)}{dt} = kP(t)N_j(t)\overline{\sigma_j \phi} - kP(t)N_i(t)\overline{\sigma_i \phi} - N_i(t)\lambda_i \tag{4.38}$$

Where the simplified notation from equation (2.7) has been used. With initial condition $N_i(0) = 0$ the differential equation (4.38) can be solved in a manner similar to the way equation (2.6) was solved. To make the derivation simpler, this time the two approximations will be applied before seeking the solution:

$$\frac{dN_i(t)}{dt} = \quad kP(t)\underbrace{N_j(t)}_{\approx N_j}\overline{\sigma_j \phi} \quad \underbrace{-kP(t)N_i(t)\overline{\sigma_i \phi}}_{\approx 0} - N_i(t)\lambda_i$$
$$N_i(t_0) \approx N_j\overline{\sigma_j \phi}e^{-\lambda_i t_0}\int_0^{t_0} kP(t)e^{\lambda_i t}dt$$

The foil activity $A_{\phi(t)}(t_0)$ during irradiation at time t_0 due to a time-dependent flux $\phi(t, E)$

66

is:

$$A_{\phi(t)}(t_0) = N_j \overline{\sigma_j \phi} \lambda_i e^{-\lambda_i t_0} \int_0^{t_0} kP(t) e^{\lambda_i t} dt \tag{4.39}$$

Note that when $kP(t) = 1$, equation (4.39) reduces to the time-independent equation (2.10). Equation (4.39) can be rewritten in terms of the activity $A_\phi(t_0)$ due to a time-independent flux:

$$A_{\phi(t)}(t_0) = \underbrace{\left(N_j \overline{\sigma_j \phi} (1 - e^{-\lambda_i t_0}) \right)}_{A_\phi(t_0)} \left(\frac{\lambda_i e^{-\lambda_i t_0}}{(1 - e^{-\lambda_i t_0})} \int_0^{t_0} kP(t) e^{\lambda_i t} dt \right)$$

This equation can be rearranged so that the activity $A_\phi(t_0)$ due to a time-independent flux is written in terms of power history correction factor $C_P(P(t), t_0)$:

$$A_{\phi(t)}(t_0) = C_P(P(t), t_0) \quad A_\phi(t_0) \tag{4.40}$$

$$C_P(P(t), t_0) = \frac{\lambda_i e^{-\lambda_i t_0} \int_0^{t_0} kP(t) e^{\lambda_i t} dt}{1 - e^{-\lambda_i t_0}} \tag{4.41}$$

Equation (4.41) permits activity analysis of a fluctuating power foil irradiation by relating it to a constant power case. This correction requires the time dependence of the beam power $P(t)$, which is known for a given irradiation. The integral in equation 4.40 is computed by the custom program `PowerIntegrator.py`.

4.4 Other Corrections

4.4.1 Partially Irradiated Foils

Autoradiography is the primary tool in determining if a foil has been partially irradiated. While a foil still retains significant activity, it is exposed to an autoradiographic plate, generating two-dimensional image of its activity. This image is then analyzed using the ImageJ program. Tools in ImageJ allow pixel sizes to be calibrated to absolute length, so that total irradiation area can be determined. The ratio of the irradiated area to the total area is a fractional factor that can be applied to activity and reaction rate calculations used in the unfolding.
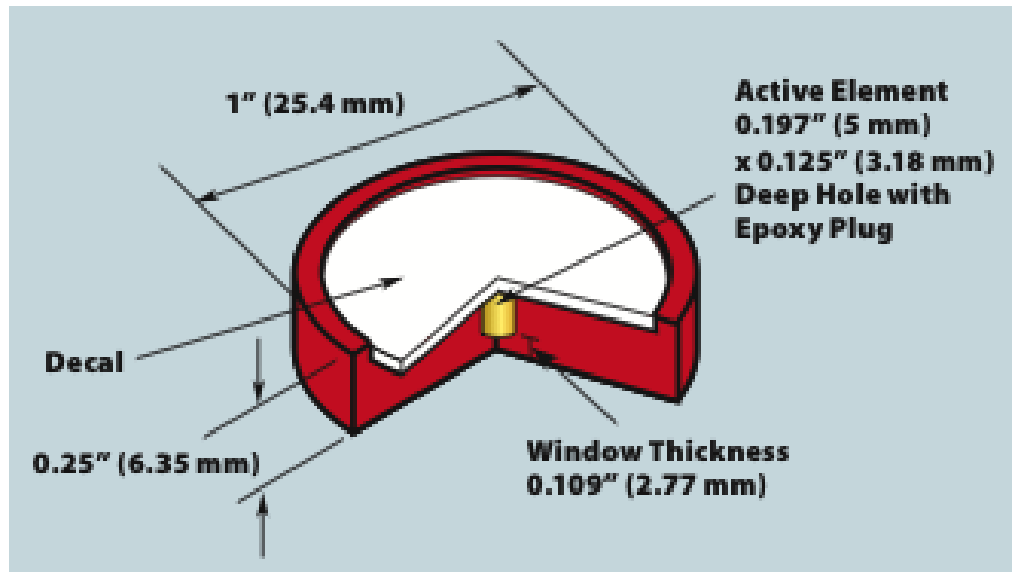
Figure 4.2: Dimensions of the sources used for calibration of the gamma-ray spectrometer [72].

4.4.2 Calibration Source Size Versus Foil Size

Although the sample holder attempts to colocate the axial and radial centers of the calibration source and foils using two trays, the calibration sources and the foils are not of the same dimensions. This introduces small errors into the efficiency calculation. The active volume of the calibration sources is a cylinder 5 mm in diameter and 3.18 mm high (Figure 4.2), while the foils are cylinders ~10 mm in diameter and up to 10 mm high. The closer the sample is measured to the gamma-ray spectrometer, the more sensitive it is to differences in position. Sensitivity to changes in position can be empirically estimated from calibrations at various positions. Based on these calibrations, the differences in the calibration source size and foil size can safely be neglected.

Chapter 5

Measurement Results

This chapter details the experimental measurements and their results. Two foil irradiations were performed: at the ARCS beamline, and at the POWGEN beamline.

5.1   July 8, 2009 ARCS

5.1.1   Foil Irradiation

Foil Packet

The foil packet used at the ARCS beamline consisted of four types of foils: two aluminum, three copper, three nickel foils, and a single bismuth foil. These foils were selected because they were immediately available for the irradiation opportunity. The foils were mounted to an aluminum holder and wrapped in aluminum foil ($\sim$0.033 mm thickness). The packet was mounted to a sample stick and placed in the beam at the ARCS sample location.

Beam Power

As discussed in Section 4.3.4 beam power on the target must be monitored to scale the calculated flux spectrum appropriately. The power on target is measured using a proton beam current monitor in the final beam transport section of the accelerator. Measurement uncertainty on this instrument is unavailable. Tens of thousands of control points, including the proton beam power, are recorded by the centralized controls system at the SNS. Once recorded, the values of these control points can be retrieved using software
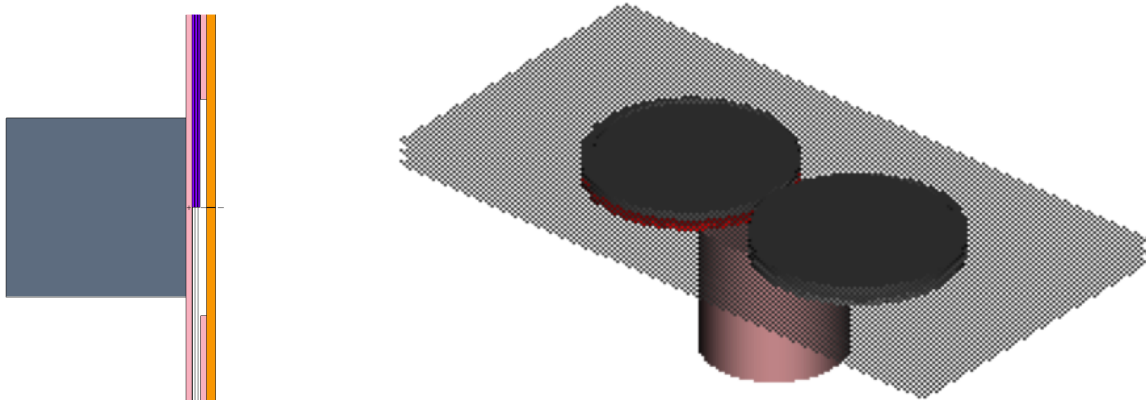
Figure 5.1: Bismuth, copper, nickel, and aluminum foils along with aluminum holder as modeled in MCNPX and visualized with the VisEd (left) and Sabrina (right) software.

from a system archive. Unfortunately, during the ARCS foil irradiation, the control system archive experienced some kind of system-wide error that prevented data recording. This error was confirmed with SNS control systems staff [73]. Therefore, no beam power data was archived during the irradiation for approximately 55 minutes from 12:10 until 13:15. The author does not recall significant power fluctuations during this time and none were noted in the log book, but beam power fluctuations may have occurred.

Due to the control system archiver failure, the beam power history must be assumed during the 55 minute interval. The power history during this interval is assumed to be similar to the power history that was recorded by the control system archiver from 13:15 until 14:54. The power history from 13:15 to 14:54 was used to calculated the power history correction factor. The average power from 13:15 to 14:53 is 379.748 kW. The calculated correction terms are minor, in most cases less than 1% (Table 5.1).
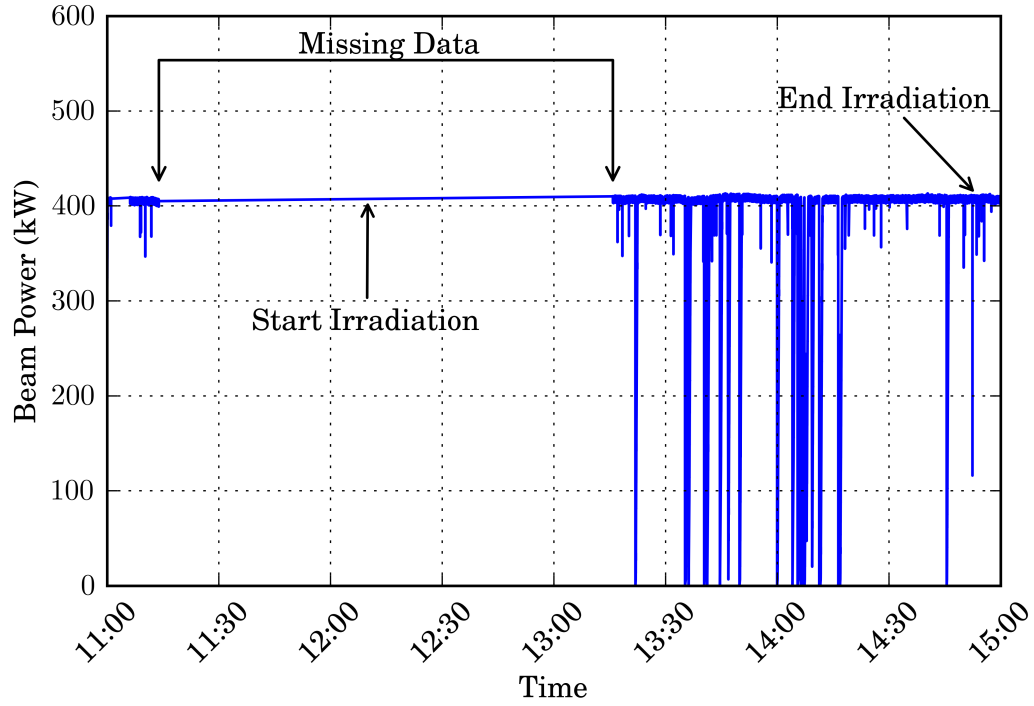
Figure 5.2: Beam power during the July 8, 2009 ARCS foil irradiation.

Nuclide	Correction	Nuclide	Correction
^{208}Bi	1.000	^{200m}Bi	1.017
^{207}Bi	1.000	^{199}Bi	1.020
^{206}Bi	1.000	^{199m}Bi	1.023
^{205}Bi	1.000	^{198m}Bi	1.046
^{204}Bi	1.001	^{57}Ni	1.000
^{203}Bi	1.000	^{58}Co	1.000
^{202}Bi	1.004	^{61}Cu	1.002
^{201}Bi	1.004	^{64}Cu	1.000
^{201m}Bi	1.008	^{24}Na	1.000
^{200}Bi	1.014	^{27}Mg	1.052

Table 5.1: Power history corrections for the ARCS foil irradiation. Corrections are defined by equation 4.41.

Figure 5.3: Radiation control technician checks the dose rate on the foils as they are removed the sample position after irradiation.

Irradiation Time

The total irradiation time from 12:10 to 14:54 is 9840 ± 120 s.

Cooling Time

When the beamline shutter was closed at 14:54, irradiation ceased and the foil activity began to decay. A finite time interval was necessary to remove the foils and have a radiation control technician perform a radiological survey. The foils were then transported to the counting room, and several initial counts were performed, none of which were used for the final analysis. The count used for the analysis began at 18:38:41, so the cooling time is approximately 3 hours and 44 minutes ($13{,}380 \pm 120$ s).
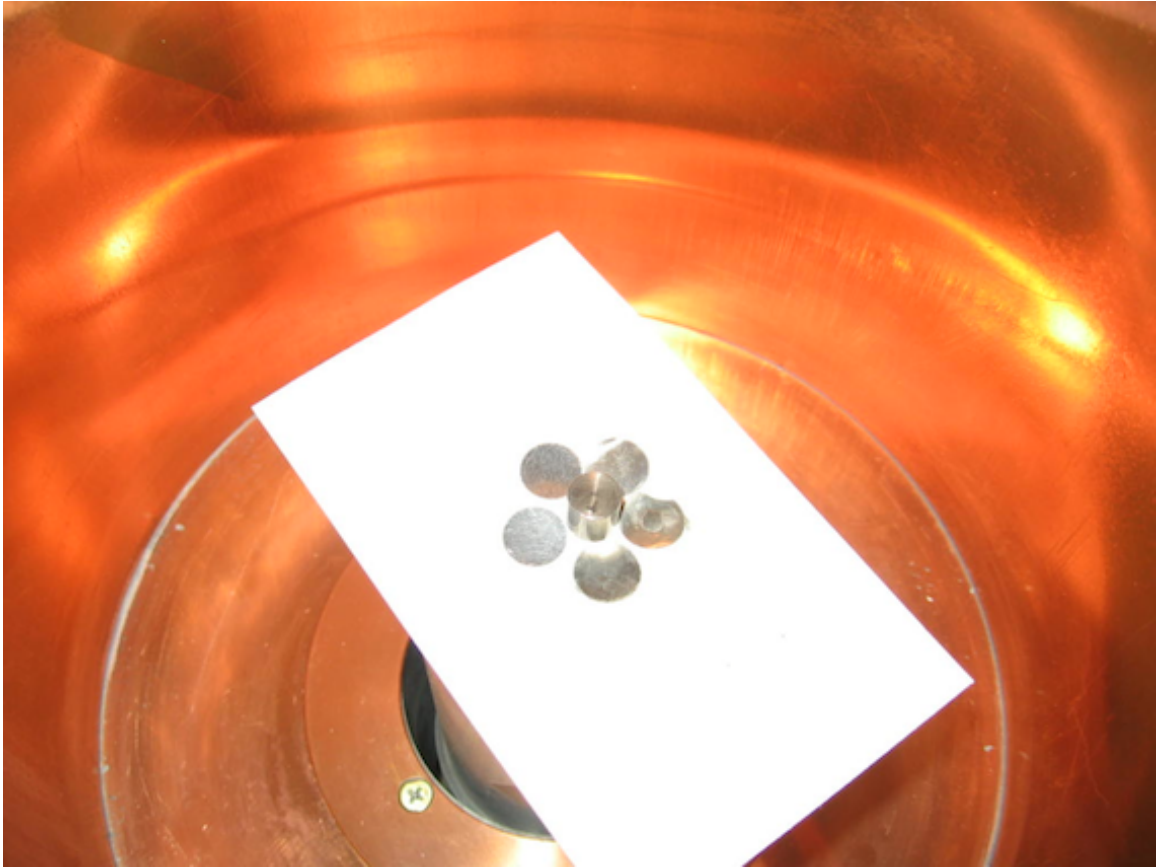
Figure 5.4: Foil activity was measured on the detector end cap. A white index card was used to reduce possible contamination of the detector.

5.1.2 Gamma Spectrometry

Energy and Efficiency Calibrations

Energy and efficiency calibrations were performed using the following radioisotope calibration sources: ^{109}Cd, ^{57}Co, ^{123m}Te, ^{51}Cr, ^{113}Sn, ^{85}Sr, ^{137}Cs. The energy calibration used 15 peaks ranging from 122 keV to 2754 keV. A linear fit was made to the data with a coefficient of determination r^2 value of 0.999.

The efficiency calibration used 5 peaks ranging from 159 keV to 835 keV. The data were used to produce a linear fit (natural log of efficiency vs. natural log of energy) with a coefficient of determination r^2 value of 0.997. Because the samples were measured on the detector cap in a "close geometry," True Coincidence Summing (TCS) was present. Only non-cascade gamma peaks were used for the calibration, which limited the number
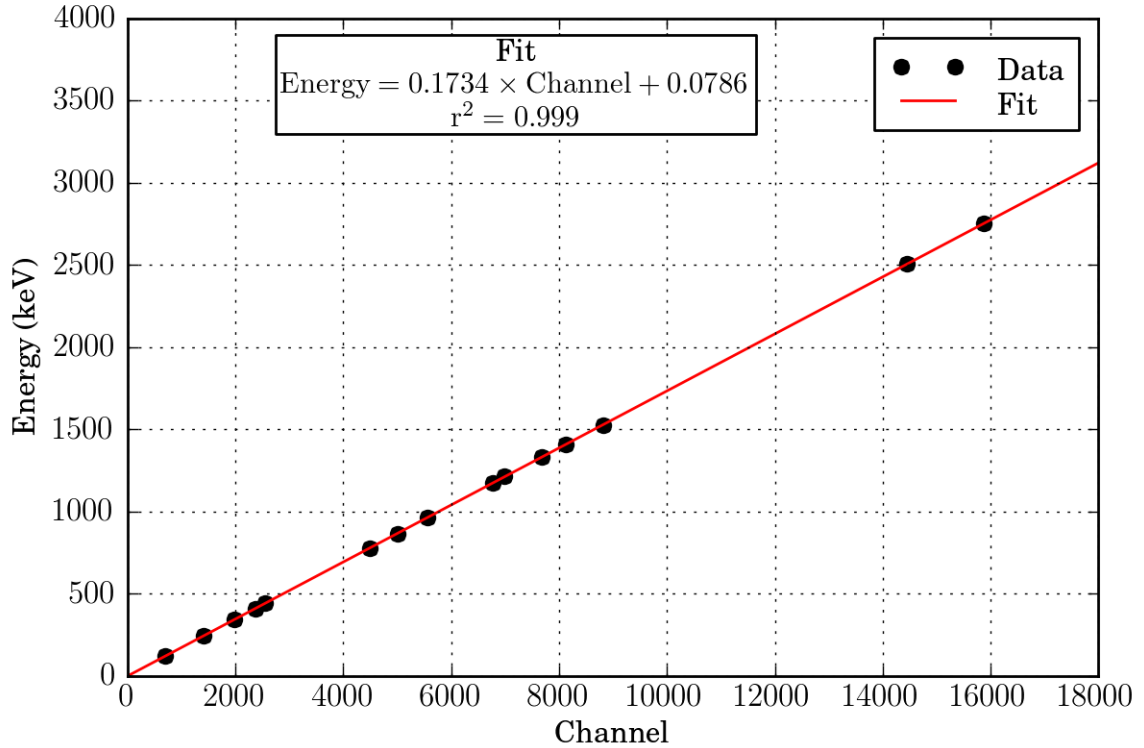
Figure 5.5: Energy calibration curve for the HPGe spectrometer used for the ARCS foil irradiation.

of peaks to 5. Efficiency data below 159 keV were not required for the measurements, but several efficiency measurements beyond 835 keV, where the curve is extrapolated, were made. When possible, the use of extrapolated curves is best avoided. Unfortunately, in this case no non-cascade gamma peaks above 835 keV were measured with the available calibration sources. Use of the extrapolated curve is justified because in the 130 keV to 2000 keV range, the efficiency curve (natural log of efficiency vs. natural log of energy) is expected to be approximately linear [10].
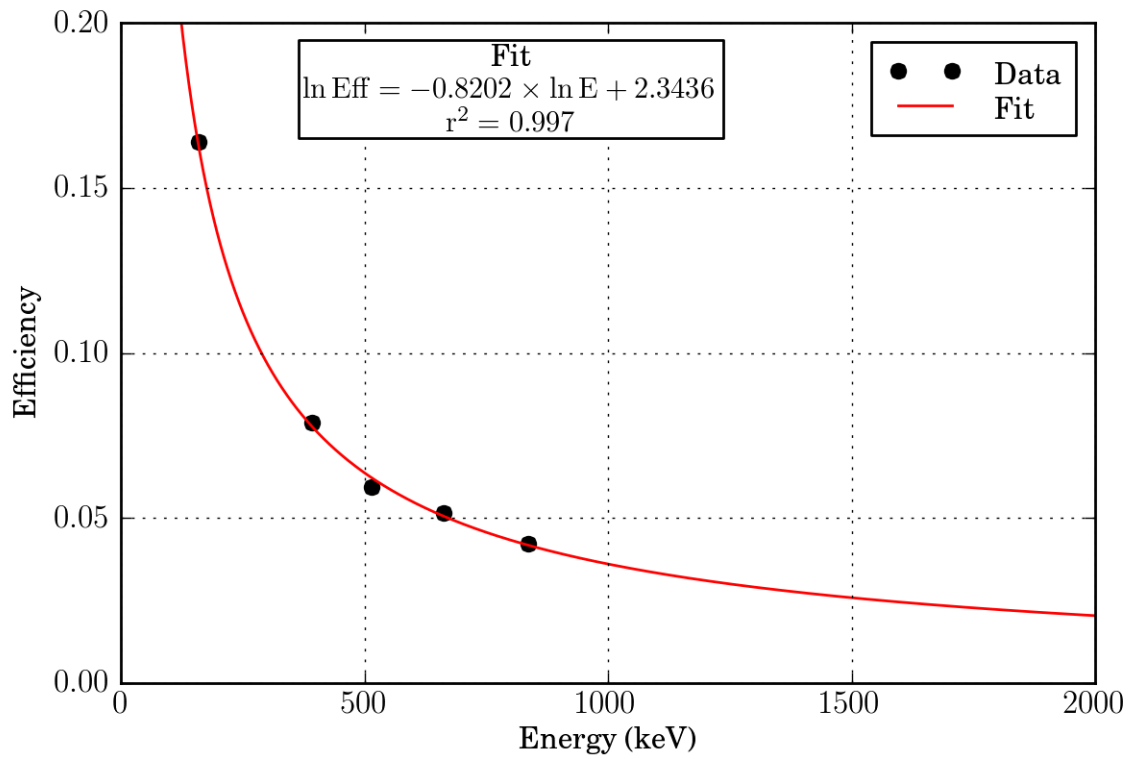
Figure 5.6: Efficiency calibration curve for the HPGe spectrometer used for the ARCS foil irradiation.

Count Time

The count used for the analysis was started at 18:38:41.

Total Real Time: 148,745.00 ± 1 s (∼ 41.3 hours)

Total Live Time: 147,618.00 ± 1 s (∼ 41.0 hours)

Candidate Peaks

Forty-one full-energy peaks from 10 nuclides were identified in the gamma-ray spectrum. These peaks will be referred to as "candidate peaks" because they are potentially valid peaks to use in the unfolding. Only a subset of the total peaks will be used in the unfolding. Some of the candidate peaks may have been misidentified or poorly measured. The time analysis is used to inform the selection of peaks to be used in the unfolding.

Nuclide	Peak Energy keV	Nuclide	Peak Energy keV	Nuclide	Peak Energy keV
^{199}Bi	841.70	^{204}Bi	899.15	^{206}Bi	620.48
		^{204}Bi	911.78	^{206}Bi	632.26
^{201m}Bi	846.40	^{204}Bi	918.15	^{206}Bi	803.10
		^{204}Bi	984.02	^{206}Bi	881.01
^{202}Bi	422.18			^{206}Bi	1018.63
^{202}Bi	657.49	^{205}Bi	703.44	^{206}Bi	1098.26
^{202}Bi	960.67	^{205}Bi	1043.72	^{206}Bi	1595.28
		^{205}Bi	1764.36	^{206}Bi	1718.70
^{203}Bi	820.30	^{205}Bi	1861.67		
^{203}Bi	825.20			^{58}Co	810.78
^{203}Bi	1033.80	^{206}Bi	183.98		
^{203}Bi	1536.40	^{206}Bi	262.70	^{60}Co	1173.24
^{203}Bi	1670.50	^{206}Bi	343.51	^{60}Co	1332.50
^{203}Bi	1847.40	^{206}Bi	398.00		
		^{206}Bi	497.06	^{24}Na	1368.63
^{204}Bi	374.72	^{206}Bi	516.18	^{24}Na	2754.03
^{204}Bi	670.75	^{206}Bi	537.45		

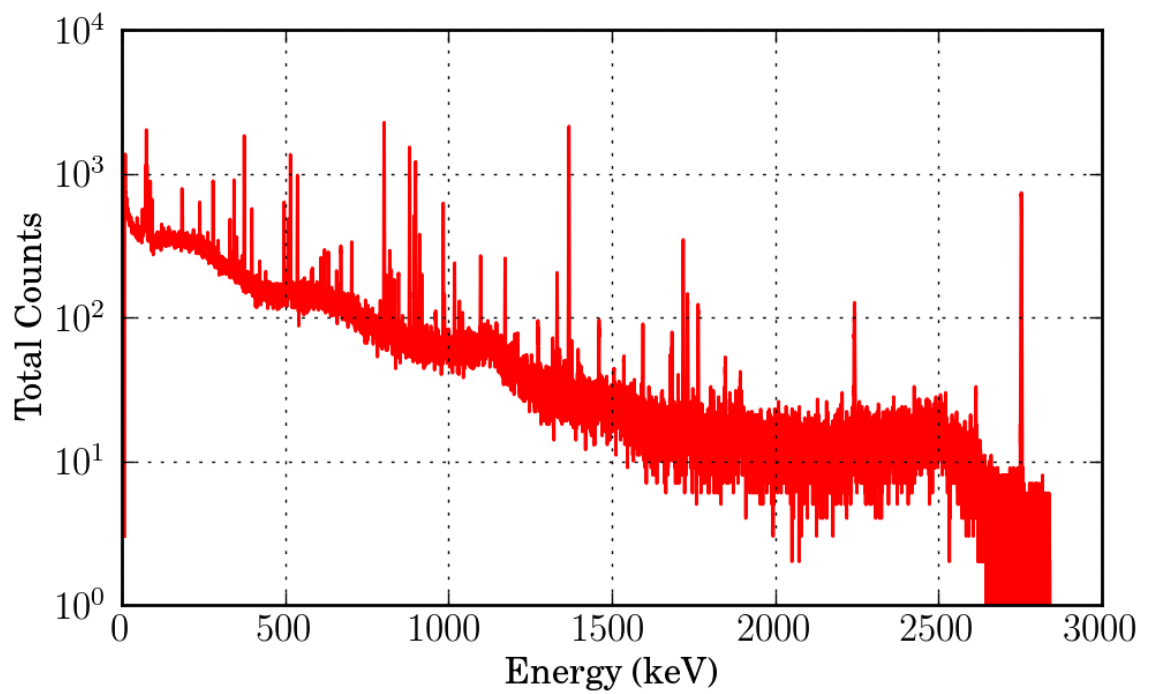Table 5.2: Candidate peaks in the gamma-ray spectrum of the ARCS foil irradiation.

Figure 5.7: The gamma-ray spectrum of the foils irradiated at the ARCS beamline.

Time Analysis

As a precaution, the gamma-ray spectrum was saved several times while counting. Later it was realized these data could be used to measure the decay constant of candidate peaks. Measuring the decay constant provided more evidence to determine if a peak was legitimately produced by the suspected nuclide in the foil. In other words, if the measured decay constant of a candidate peak is significantly different from the known decay constant, this peak can be eliminated as a candidate. Decay constants longer than a few days were difficult to measure with these low count rates and relatively short count times. In many cases, at least one peak per nuclide was measured with a relative error less than 10%.
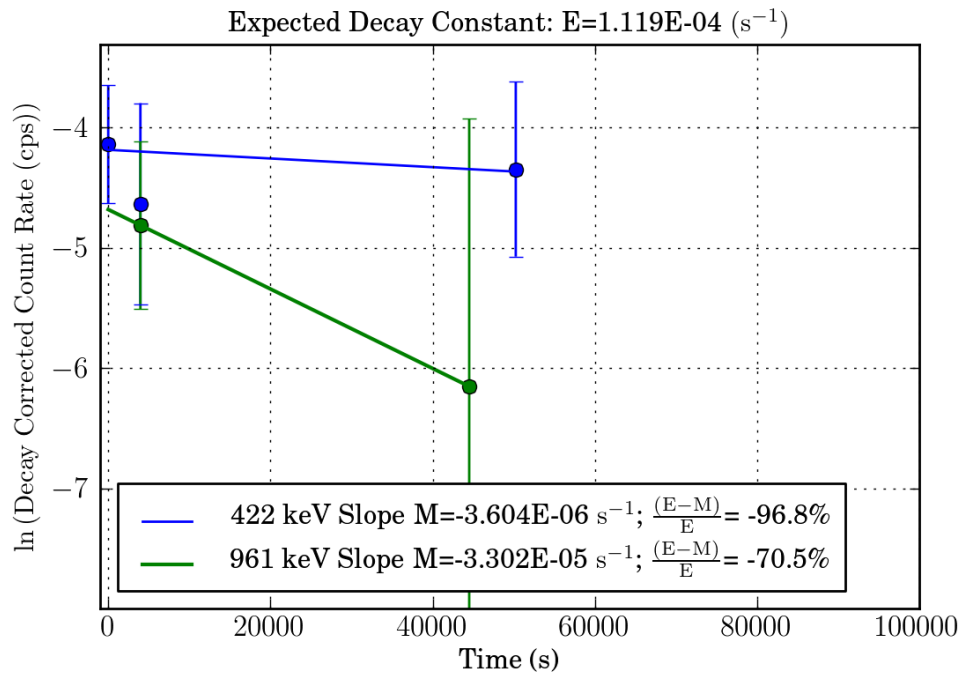
(a)
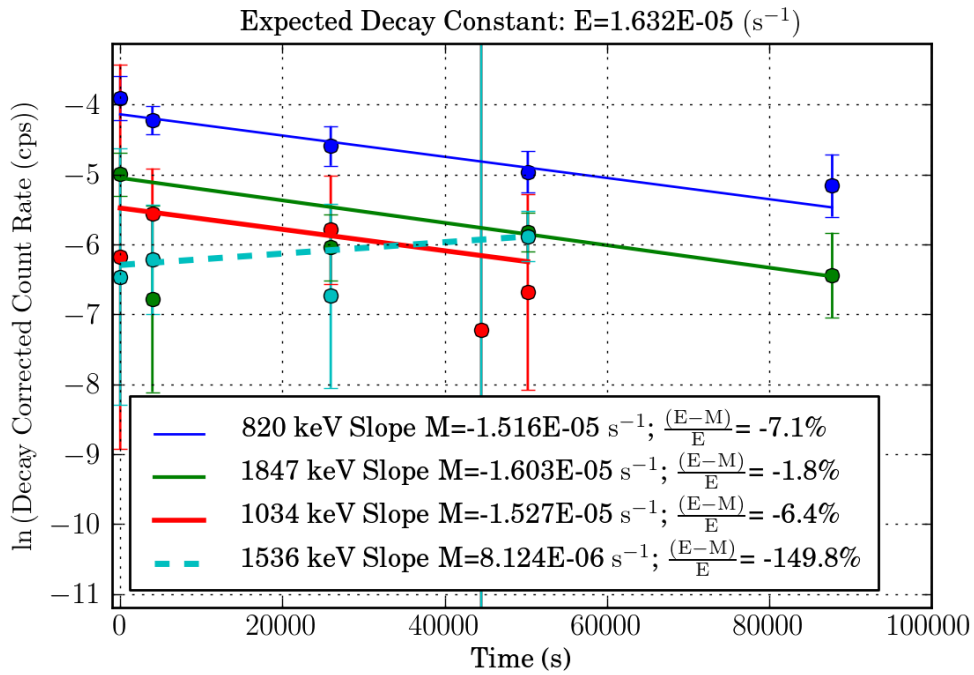
(b)

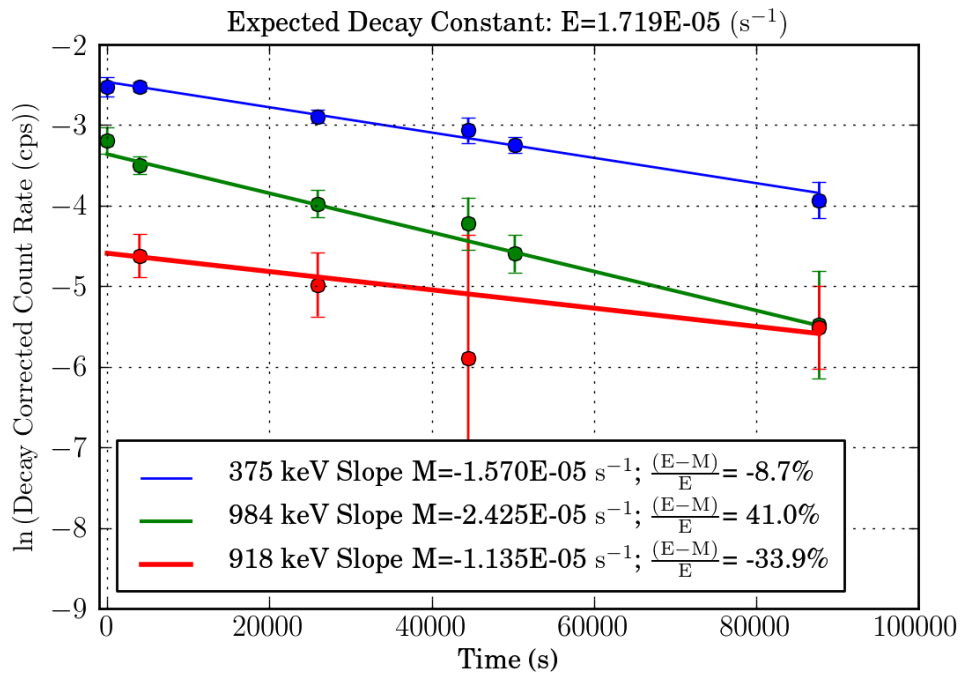Figure 5.8: Time analysis measuring the decay constant for the ^{202}Bi and ^{203}Bi candidate peaks.

79
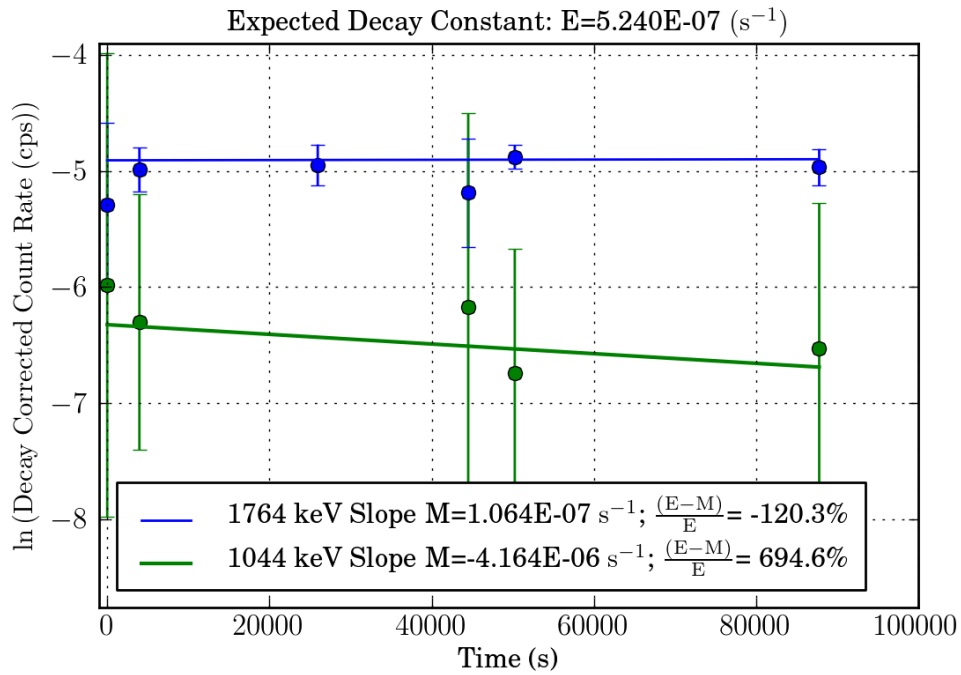
(a) ^{204}Bi

(b) ^{205}Bi
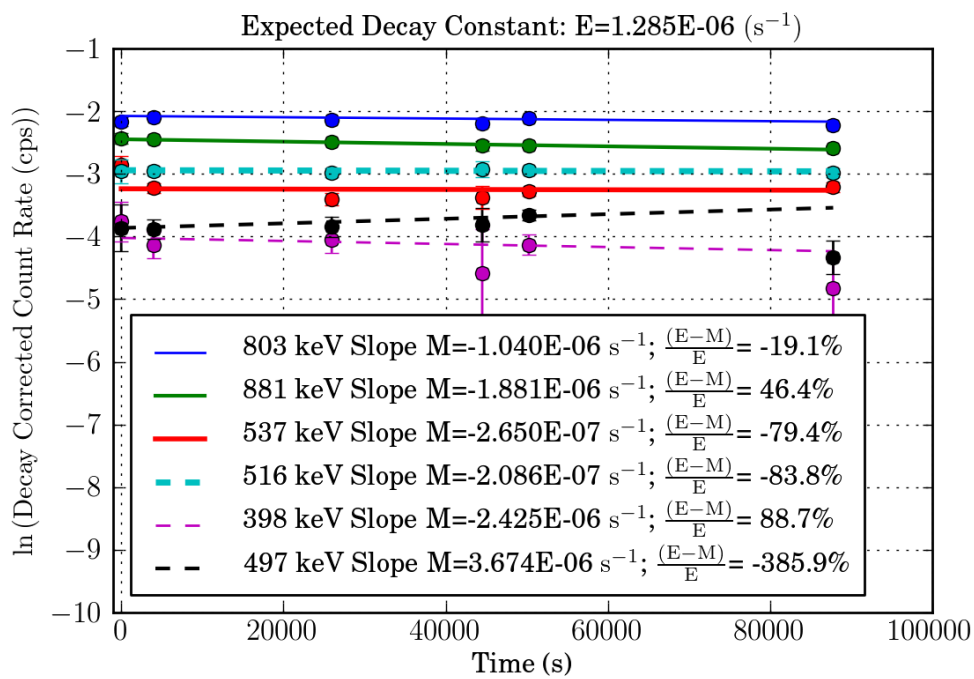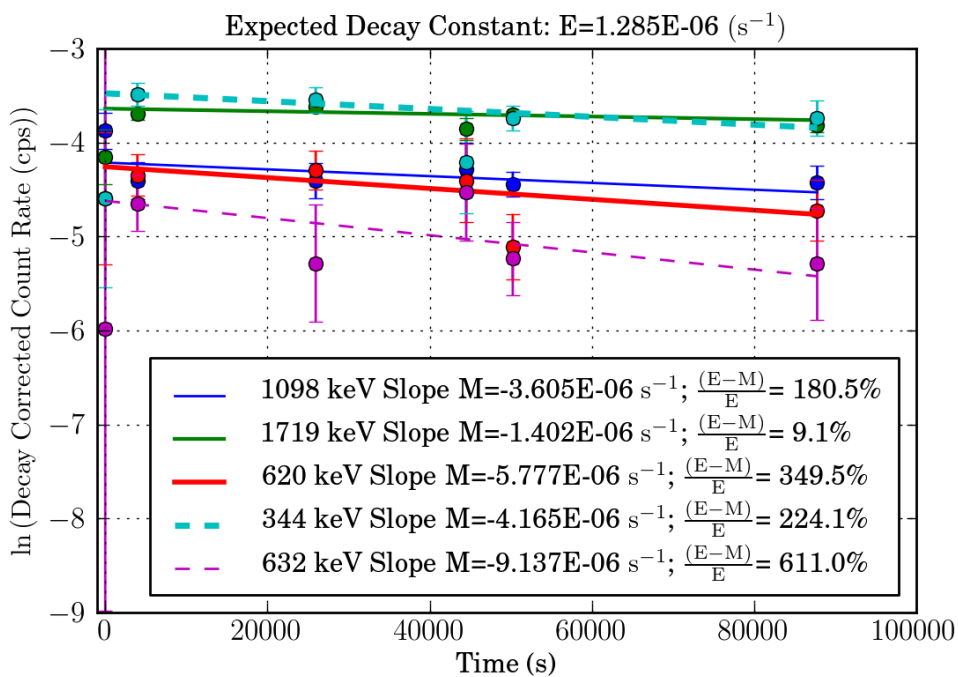
Figure 5.9: Time analysis measuring the decay constant for the ^{204}Bi and ^{205}Bi candidate peaks.

Figure 5.10: Time analysis measuring the decay constant for the ^{206}Bi candidate peaks.

(a) ^{58}Co

(b) ^{24}Na
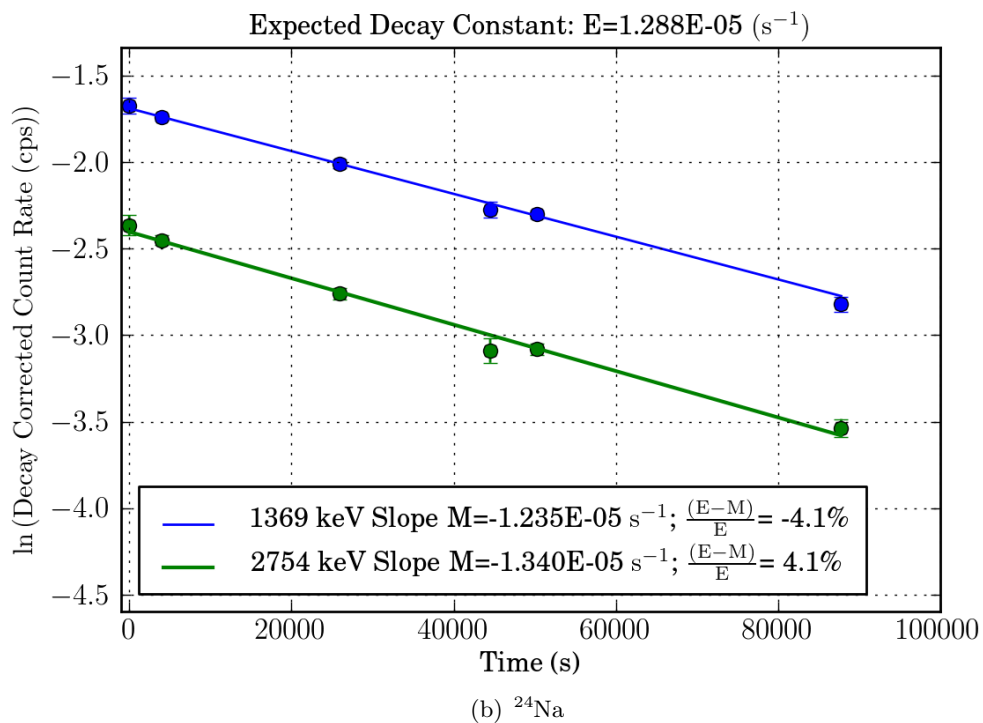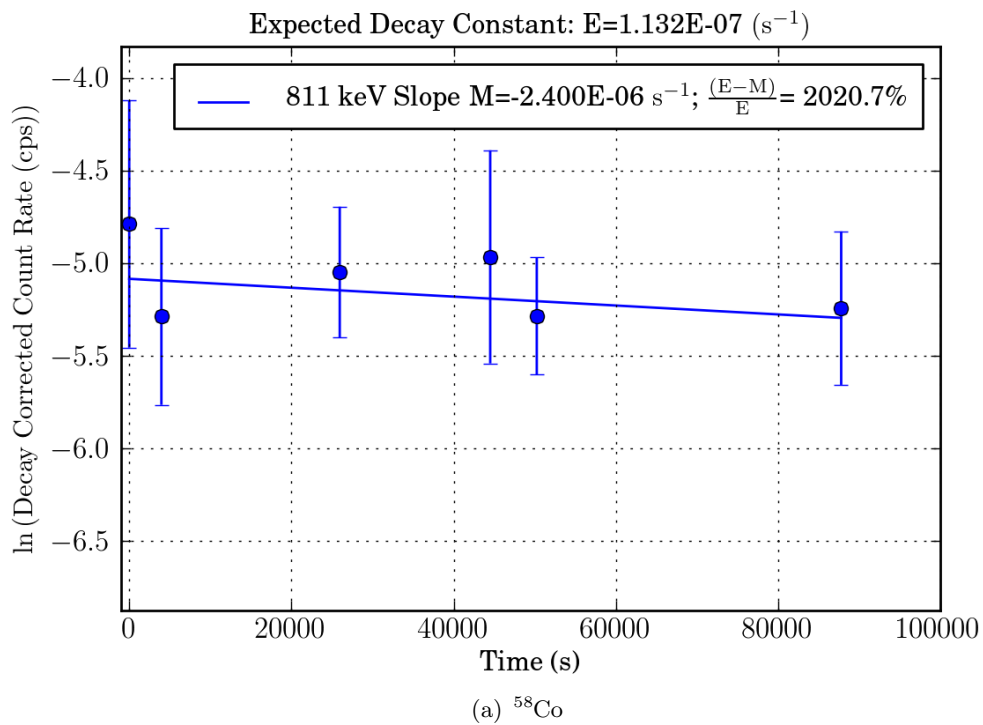
Figure 5.11: Time analysis measuring the decay constant for the ^{58}Co and ^{24}Na candidate peaks.
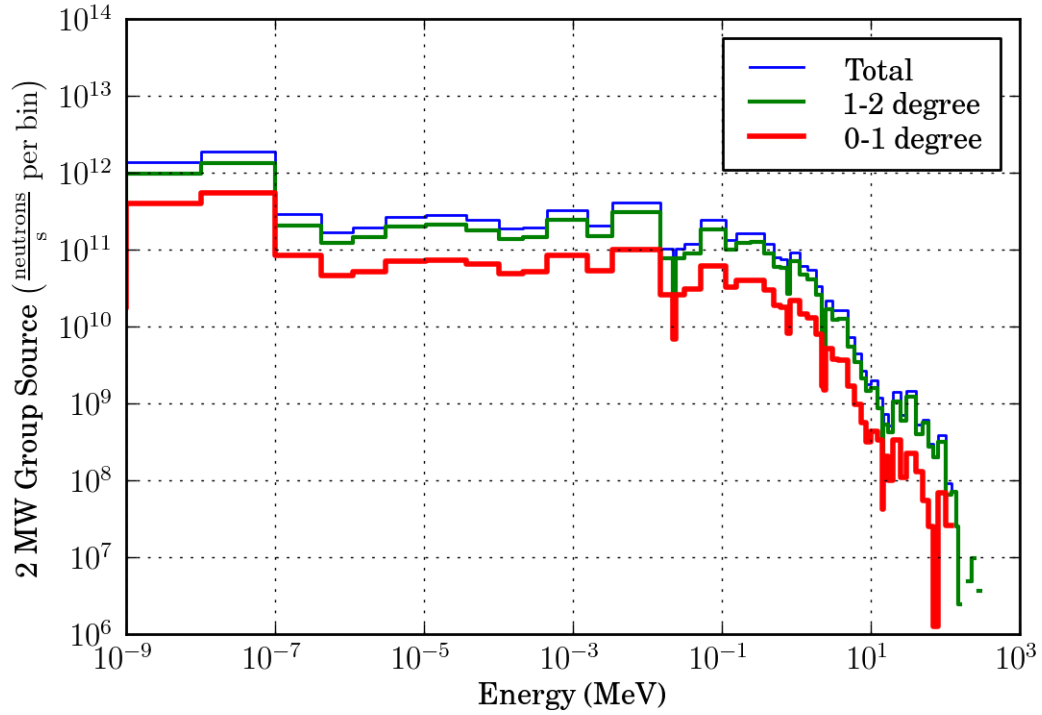
Figure 5.12: Calculated ARCS group source spectrum.

5.1.3 Unfolding

ARCS Calculated Spectrum

A neutron source spectrum for the ARCS instrument was calculated and used for shielding design at the SNS [74]. This neutron source spectrum represents the best estimate for the high-energy beam at ARCS. The origin of the source is at the core vessel insert, approximately 1 m from the moderator face and 13.6 m from the sample position. The source area is rectangular (12 cm x 10 cm) with two angular distributions ($0° < \theta < 1°$ and $1° < \theta < 2°$) each with an associated energy distribution. Only neutrons in the central angular distribution are transported uncollided to the sample location. The flux at the sample location is computed using MCNPX and the calculated source spectrum.
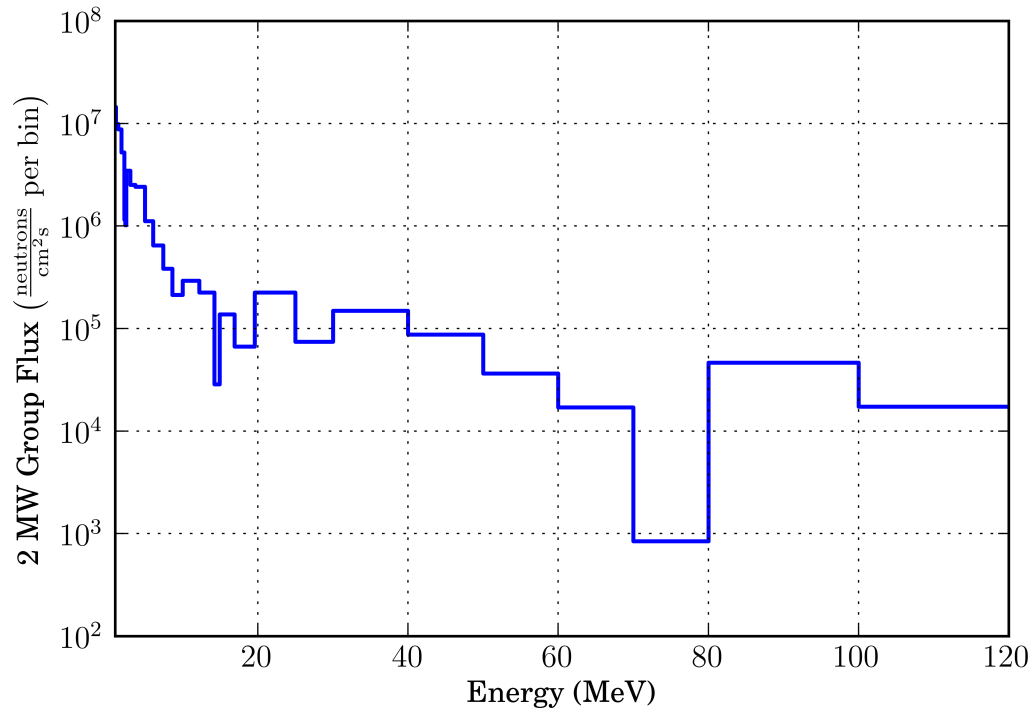
Figure 5.13: Calculated ARCS flux spectrum at the sample location.

Calculated Vs. Measured Counts

Using the calculated ARCS spectrum to compute reaction rates, then using the irradiation, cooling, and counting time along with the gamma-ray emission probability, spectrometer efficiency, gamma self-shielding, and power-history corrections, the expected number of counts were computed for each peak. If the calculated ARCS spectrum accurately reflects the measured spectrum, the ratio of the calculated counts to the measured counts should be approximately 1. In all cases, the average calculated-to-measured count ratio is greater than 1 and in most cases in the range of 3–5. This is an indication that the calculated spectrum does not accurately reflect the measured spectrum, but unfolding must be used determine a spectrum consistent with the measurements.
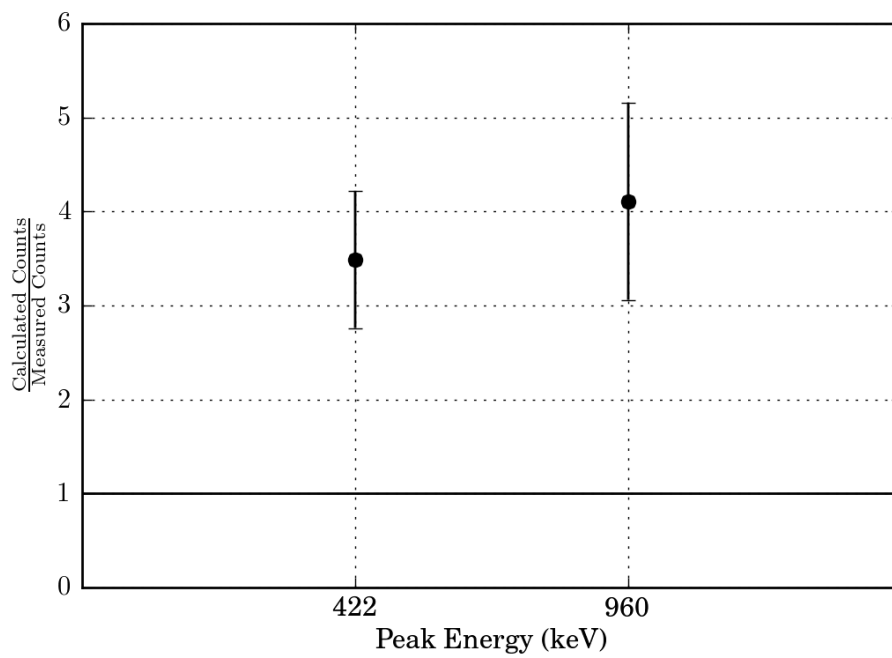
(a) ^{202}Bi
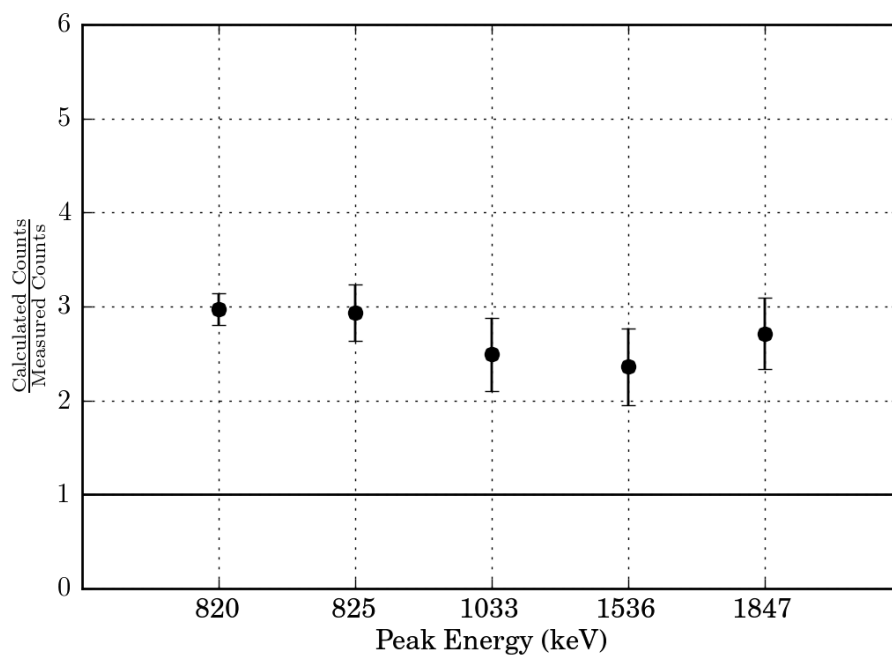
(b) ^{203}Bi

Figure 5.14: The ratio of calculated counts to measured counts for the ^{202}Bi and ^{203}Bi candidate peaks.
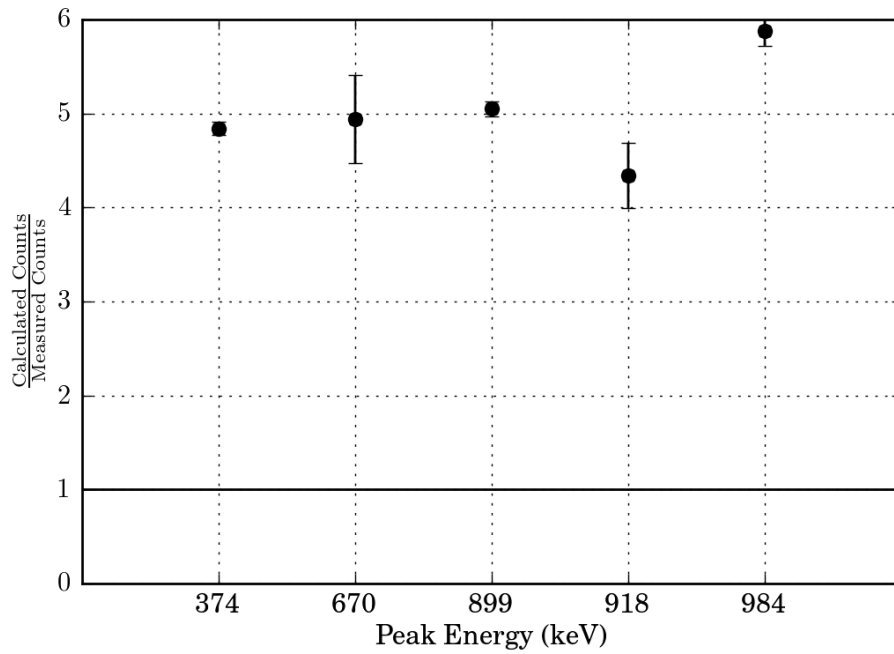
(a) ^{204}Bi
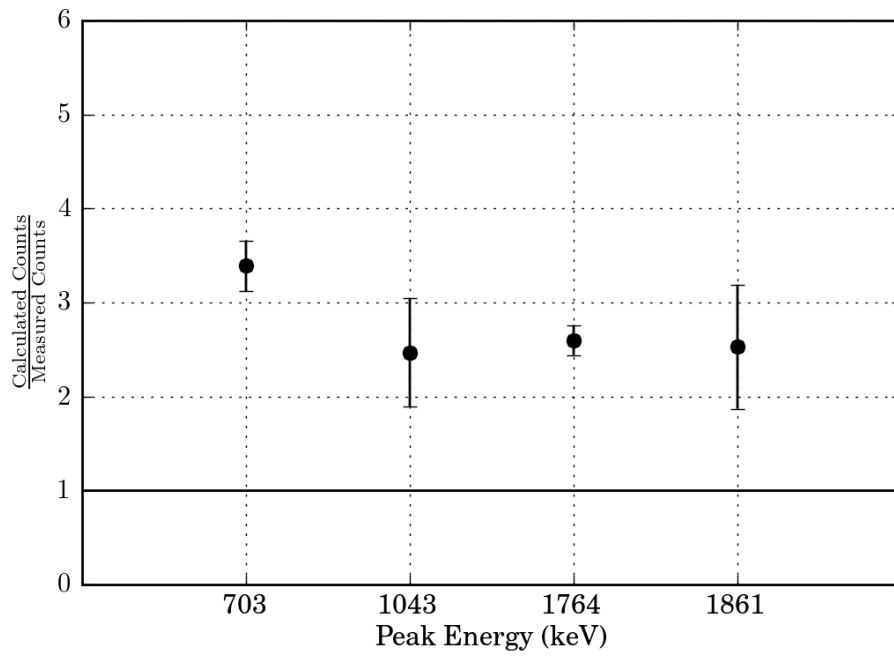
(b) ^{205}Bi

Figure 5.15: The ratio of calculated counts to measured counts for the ^{204}Bi and ^{205}Bi candidate peaks.
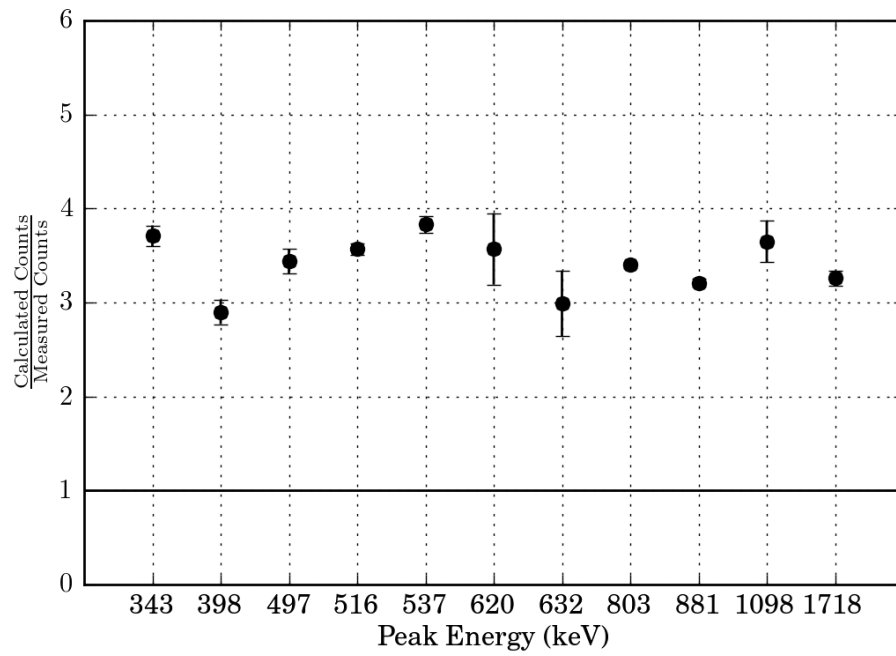
Figure 5.16: The ratio of calculated counts to measured counts for the ^{206}Bi candidate peaks.

(a) ^{58}Co

(b) ^{24}Na
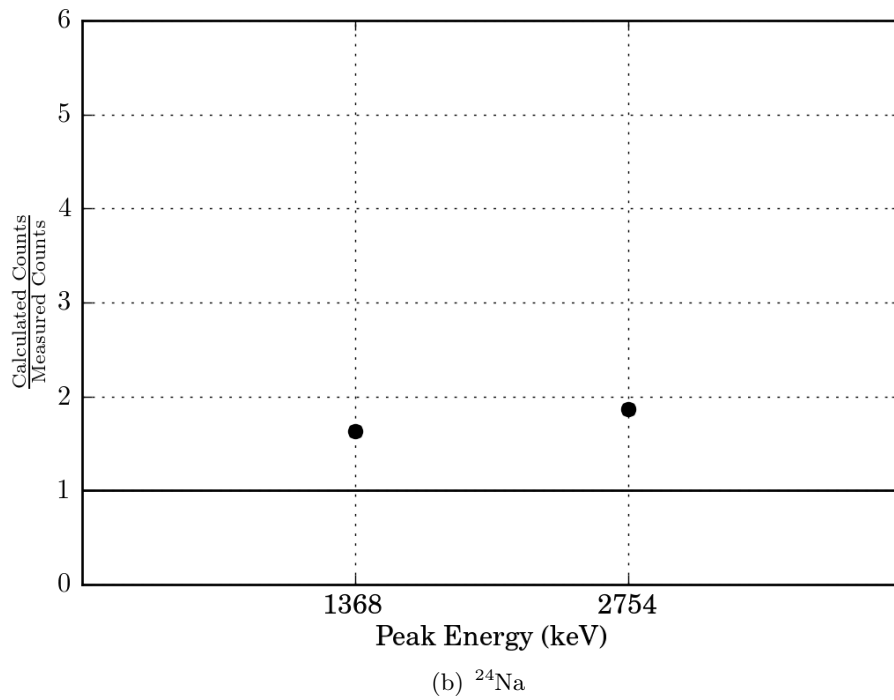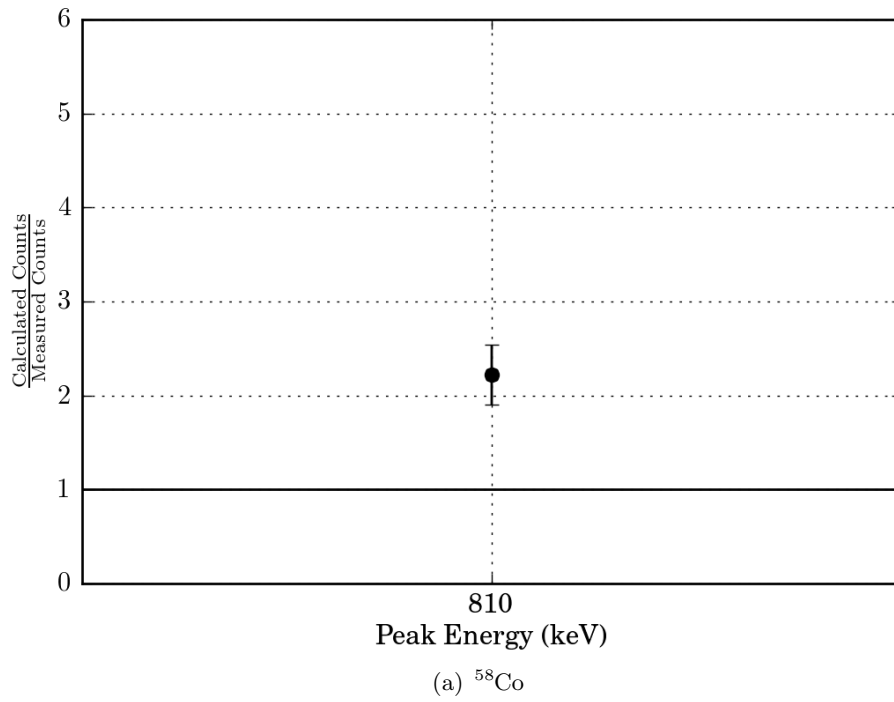
Figure 5.17: The ratio of calculated counts to measured counts for the ^{58}Co and ^{24}Na candidate peaks.
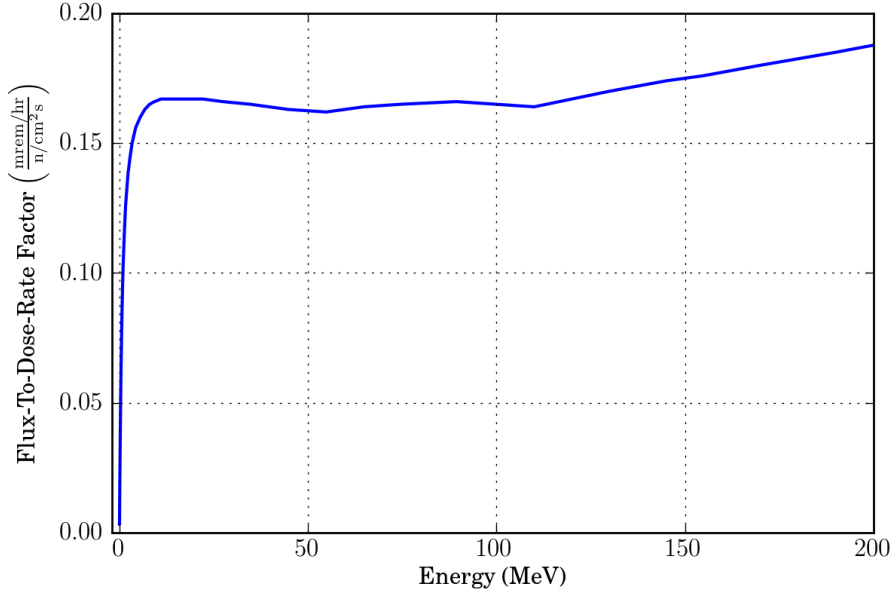
Figure 5.18: Flux-to-dose-rate conversion factor as a function of energy used to compute the dose rate metric.

Dose Rate Metric

To compare the similarity of one spectrum with a default spectrum, a dose rate metric was devised. The dose rate metric is the dose rate produced by the absolute flux differences of each energy group divided by the total dose rate produced by the default spectrum.

$$\text{Dose Rate Metric} = \frac{\sum\limits_{g=\text{groups}} |\dot{H}_g^{\text{default}} - \dot{H}_g|}{\dot{H}^{\text{default}}} \tag{5.1}$$

The dose rate metric is essentially a normalized ℓ_1 norm (or "taxi-cab" norm) weighted by an energy dependent flux-to-dose-rate conversion factor. It is always greater than or equal to the difference in overall dose rates produced by the two flux spectra. The use of the absolute value of the difference of the group-by-group dose rate means that the dose rate metric will equal zero if and only if the two spectra are identical. The energy dependent flux-to-dose-rate conversion factor used is shown in Figure 5.18.

Initial Analysis

An initial spectral unfolding from 20 MeV to 120 MeV was done with the MAXED program using reaction rates determined from 5 measured nuclide activities: ^{206}Bi, ^{205}Bi, ^{204}Bi, ^{203}Bi, ^{202}Bi. The initial default spectrum used for the unfolding was the calculated ARCS spectrum, and the response functions were determined from the group-wise reaction rates of the default spectrum. Initially, the calculated high-energy neutron flux at the sample position was used as the default spectrum in the unfolding, but later it was determined that using the source spectrum directly was more convenient.

The results of the unfolding process showed a spectral shape similar to the input spectrum, but scaled by a factor of 0.32. This scaling factor is consistent with the calculated to measured ratios observed. Using the flux-to-dose-rate conversion function, the dose rate metric between the scaled unfolded spectrum and the default spectrum is 6%. The calculated-to-measured ratios after unfolding (using the unfolded spectrum) were closer to unity, with 2 of 5 error bars overlapping a value of 1. These results were published in the AccApp'11 conference proceedings [75].

Because only 2 of 5 error bars overlapped the value of 1, because of the spread in the calculated-to-measured ratios, and because the output spectrum appeared suspiciously close to the input spectrum, a complete re-analysis of the data was done. This re-analysis uncovered errors, and therefore the unfolding produced a different result.
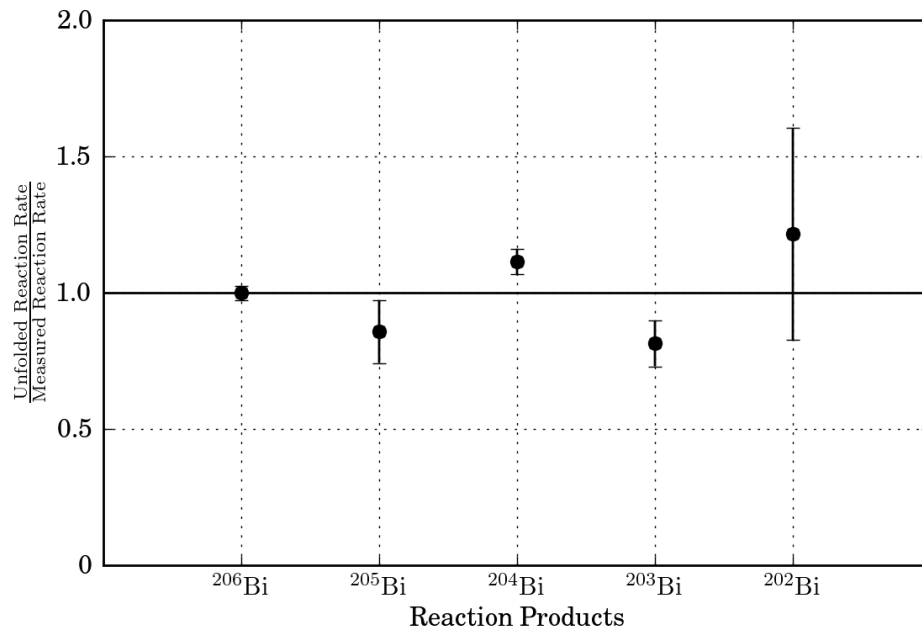
(a) Unfolded Reaction Rate to Measured Reaction Rate Ratio
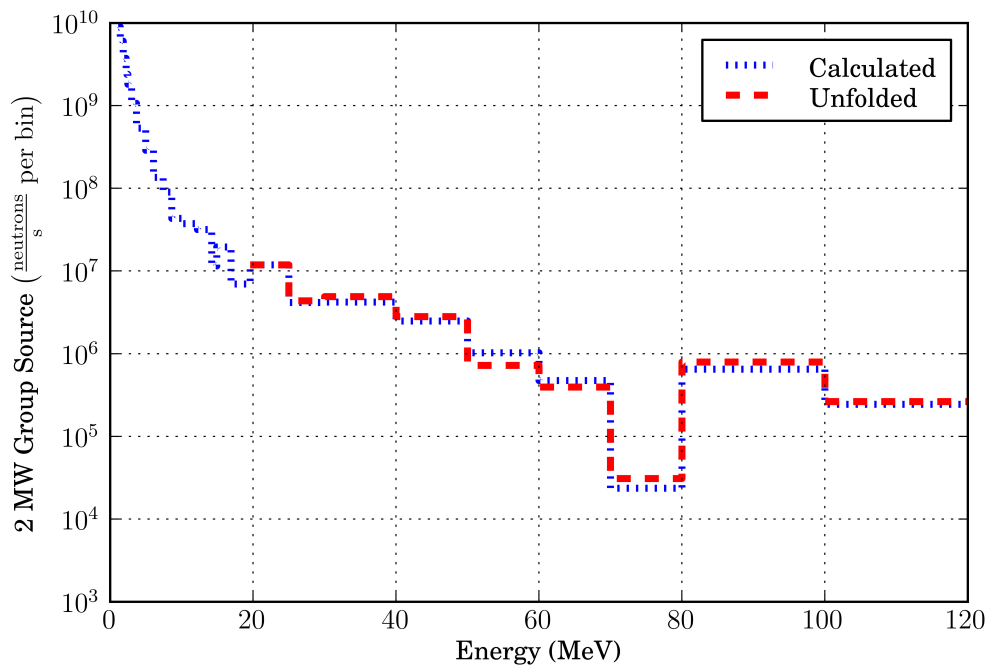
(b) Calculated and Unfolded Source Spectra

Figure 5.19: The unfolded reaction rate to measured reaction rate ratio after initial unfolding and the initial unfolded spectrum as compared to the calculated spectrum. The calculated spectrum is scaled by an overall factor of 0.32 for the best fit to the measured data.

Reanalyzed

The reanalyzed ARCS spectrum used reaction rates from 6 measured nuclide activities: ^{206}Bi, ^{205}Bi, ^{204}Bi, ^{203}Bi, ^{58}Co, ^{24}Na. Because the time analysis results of the candidate peaks were inconsistent with ^{202}Bi, this nuclide was eliminated from the reanalysis. The time analysis results showed the candidate peaks for ^{24}Na were good candidates, so ^{24}Na was added to the reanalysis. Due to the relatively long half-life of ^{58}Co, the time analysis results were inconclusive, but ^{58}Co was included in the reanalysis.

Errors in the self-shielding factors were discovered for the bismuth nuclides in the initial analysis. These errors were due to poor interpolation of values calculated for the self-shielding factors. In the reanalysis, the self-shielding factors were computed for the exact values of the gamma-ray energies.

MAXED was again used for the unfolding process. The computed ARCS spectrum was used for the initial default spectrum and for determining the response functions. The output spectral shape differed noticeably from the input spectral shape, and was scaled by 0.32. This factor of 0.32 indicates that the calculated spectrum was more intense than the unfolded spectrum. The calculated-to-measured ratios after unfolding were all consistent with unity, and all error bars overlapped 1. This result indicates that this unfolded spectrum is more consistent with the measurements, and the re-analysis is more reliable than the initial unfolding.

(a) Unfolded Reaction Rate to Measured Reaction Rate Ratio
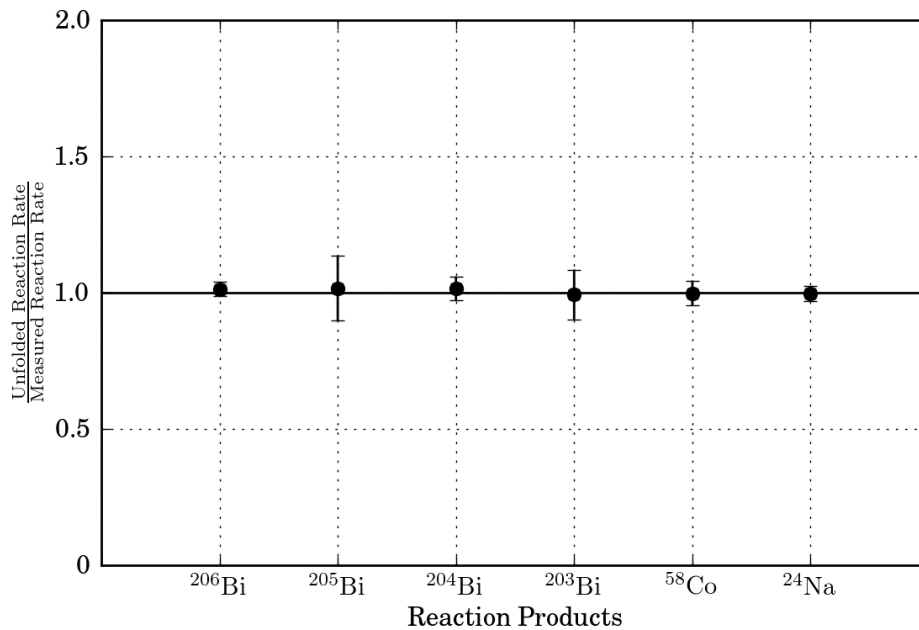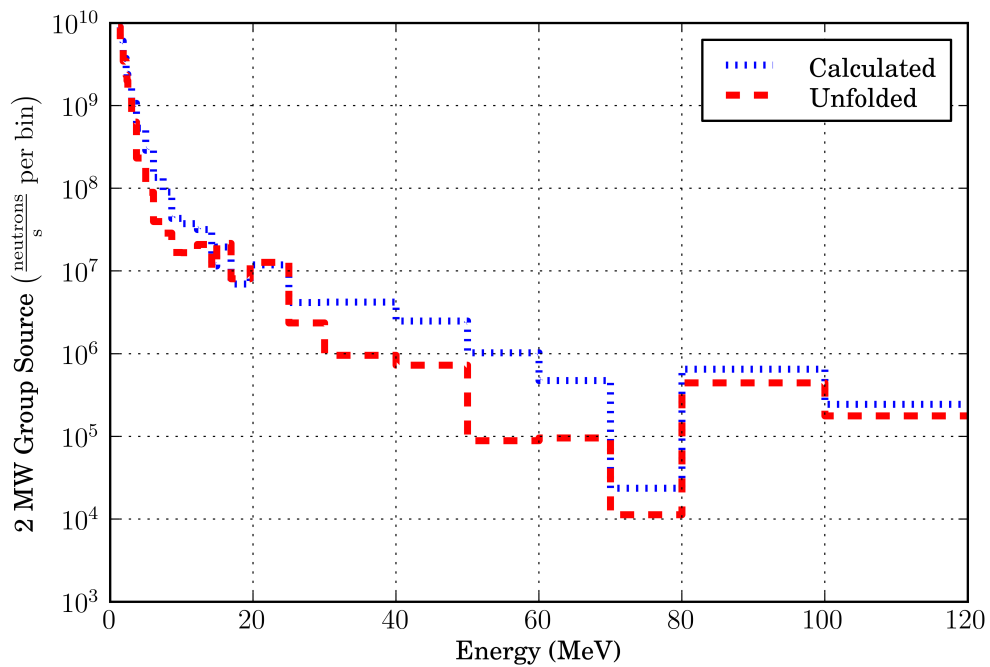

(b) Calculated and Unfolded Source Spectra

Figure 5.20: The unfolded reaction rate to measured reaction rate ratio after reanalyzed unfolding and the unfolded spectrum as compared to the calculated spectrum. The calculated spectrum is scaled by an overall factor of 0.32 for the best fit to the measured data.
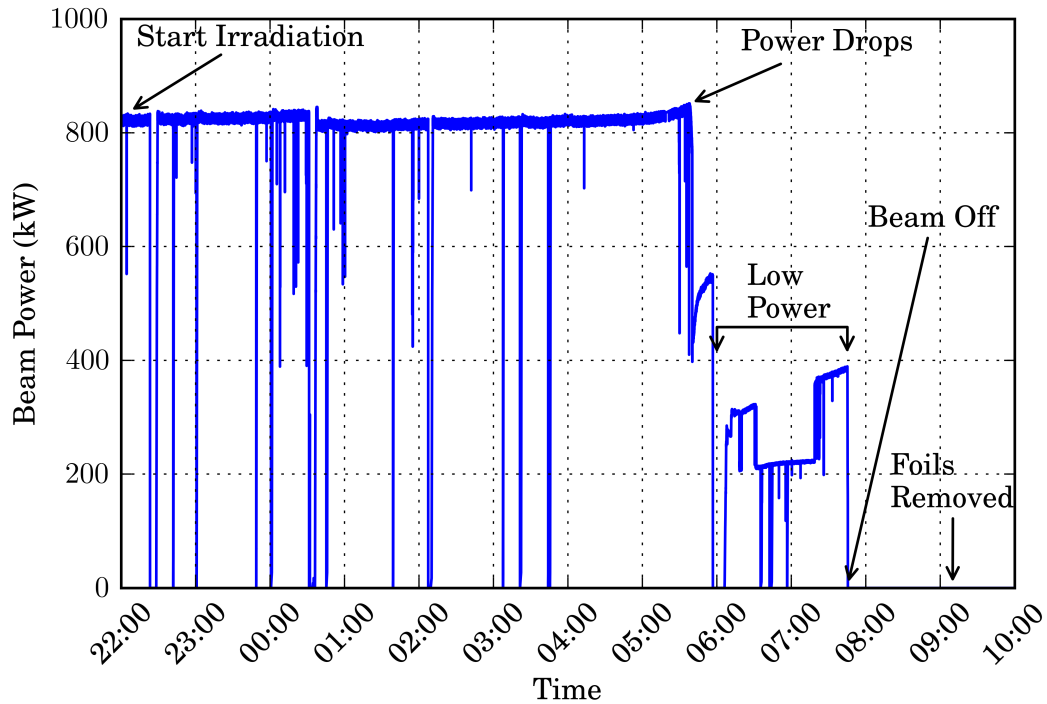
Figure 5.21: Beam power during the June 22, 2011 POWGEN foil irradiation.

5.2 June 22, 2011 POWGEN

5.2.1 Foil Irradiation

Foil Packet

The foil packet used at the POWGEN beamline consisted of nine types of foils: 3 nickel foils (previously irradiated), and a single bismuth foil in a top stack; 1 copper, 1 aluminum, 1 gold, 1 iron, 1 indium, 1 titanium, and 1 cobalt foil in a bottom stack. Five new foil types (as compared to the ARCS foil packet) were used because the additional foils provided reaction cross sections that would overlap and span the range of energies. The foils were mounted to an aluminum holder and wrapped in aluminum foil. The packet was mounted to a sample holder and placed in the beam at the sample location of the POWGEN instrument.

Beam Power

The beam power history during the POWGEN irradiation was fully archived, but fluctuated significantly. Initially the beam power level was approximately 810 kW. While at this level, the beam was off for several intervals of a few minutes. At approximately, 05:30 the beam power underwent a gradual rise, before suddenly dropping to half-power. Over the next several minutes, the power rose gradually, and then dropped to zero. After a several minute time interval of no beam, beam power returned to less than half the original power level. For a period of approximately two hours, the power level fluctuated variously between 200 kW and 400 kW. At 07:45, the beam was turned off. The foils were removed from the sample position shortly after 09:00.

The average power from the start of the irradiation at 22:06 to the time beam turned off at 07:45 is 682.794 kW. Due to the power fluctuations, the power history corrections are significant.

Irradiation Time

The irradiation began at 22:06 and ended when the beam shut off at 07:45. The total irradiation time was 34740 ± 120 s (~ 9.65 hours).

Cooling Time

The cooling time started at 07:45 and ended at 09:55 for a total cooling time of 7800 s $\pm$ 120 s (~ 2 hours 10 minutes).

5.2.2 Autoradiography

After irradiation and counting, the foils (except the bismuth foil) were placed on a gamma-ray sensitive image plate for autoradiography. The foils and plate needed to be sealed in a light-tight case, which was too small for the 1 cm thick bismuth foil, so it was excluded. The foils were allowed to activate the image plate undisturbed for ~ 1 week, and then the plate was read using the Fuji Medical Systems FLA-7000. The autoradiograph showed partial irradiation of the gold and indium foils, and low intensity total irradiation of the nickel foils. The nickel foils, having been previously irradiated, retained a residual amount
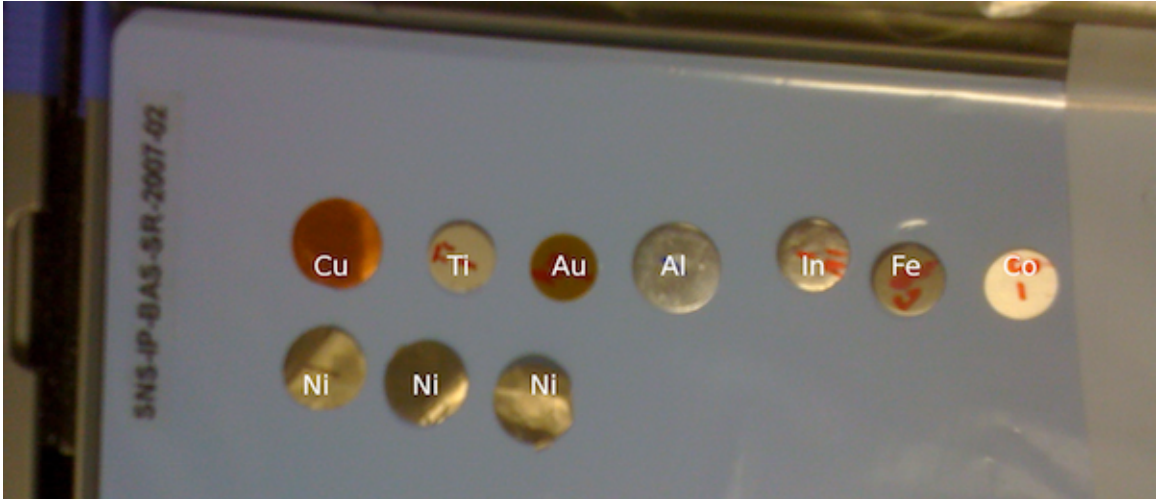
(a)
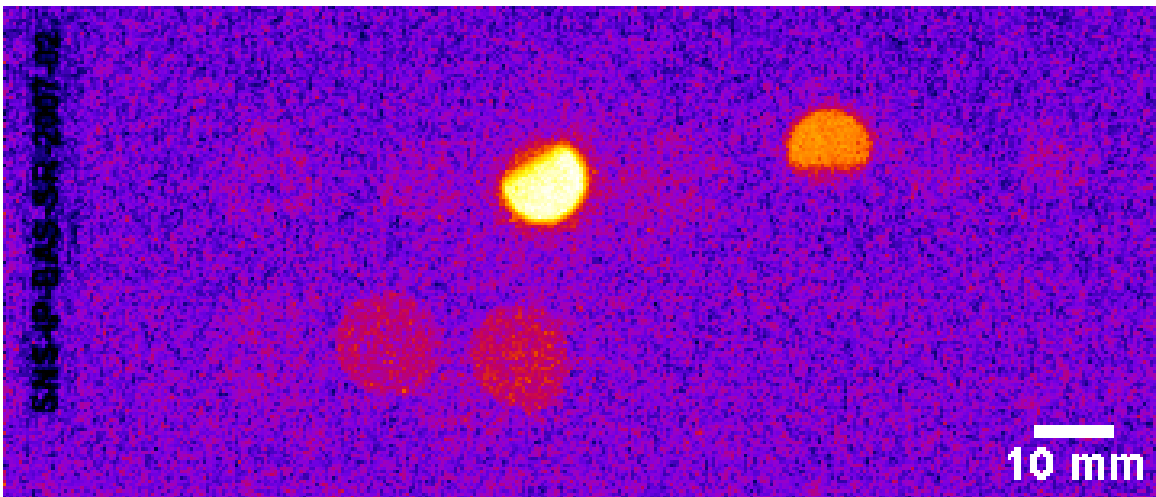
(b)

Figure 5.22: Autoradiograph for the foils irradiated at the POWGEN beamline.

of ^{60}Co activity. This residual ^{60}Co activity from the previous irradiation is likely the source of the image on the autoradiograph.

Although all foils in the top row of the radiograph image were in the same stack in the foil packet, only the gold and indium foils were visible. The activity of these foils during the exposure period must have been too low to be measured by the image plate.
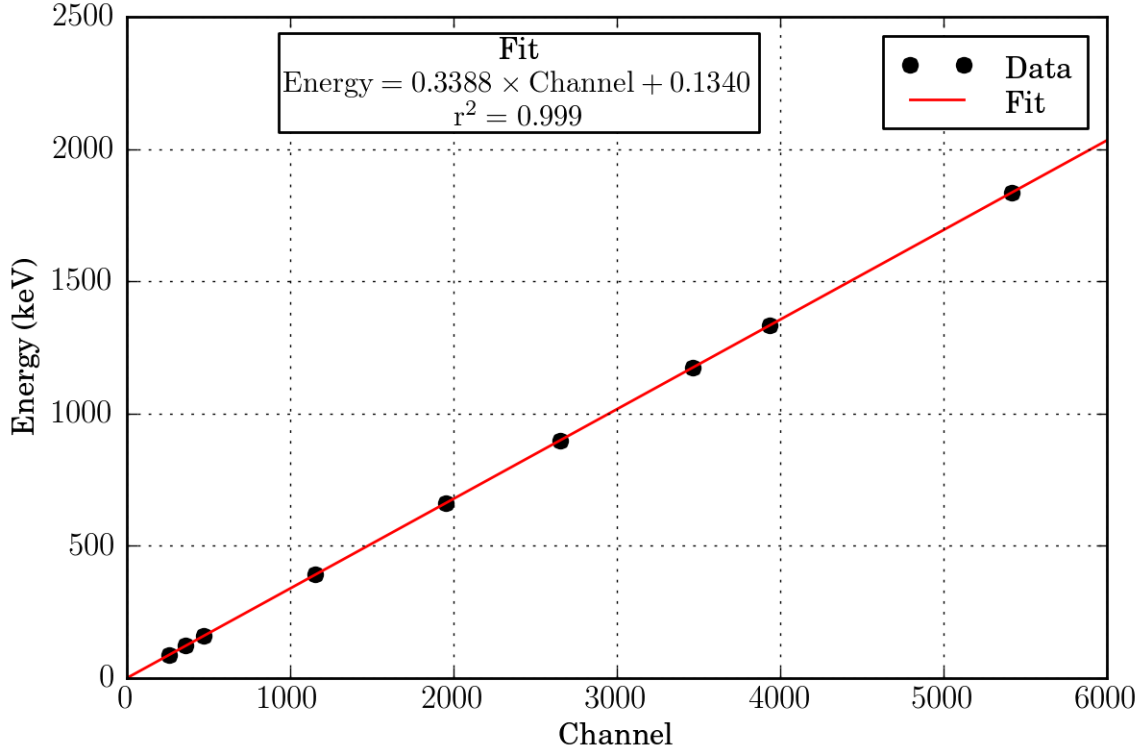
Figure 5.23: Energy calibration curve for the HPGe spectrometer used for the POWGEN foil irradiation.

5.2.3 Gamma Spectrometry

Energy and Efficiency Calibrations

Energy and efficiency calibrations were performed using the following radioisotope calibration sources: ^{22}Na, ^{109}Cd, ^{57}Co, ^{113}Sn, ^{137}Cs, ^{88}Y. The energy calibration used 9 peaks ranging from 88 keV to 1836 keV. A linear fit was made to the data with a coefficient of determination r^2 value of 0.999.

The efficiency calibration used 14 peaks ranging from 160 keV to 1835 keV. A linear fit was made to the data (natural log of efficiency vs. natural log of energy) with a coefficient of determination r^2 value of 0.999. Unlike the ARCS measurement, the calibrations and samples were measured using the sample holder sufficiently far from the detector end cap ($\sim$10 cm) to minimize TCS. Efficiency calibrations below 160 keV were performed, but these data were not needed to analyze the gamma-ray spectrum.
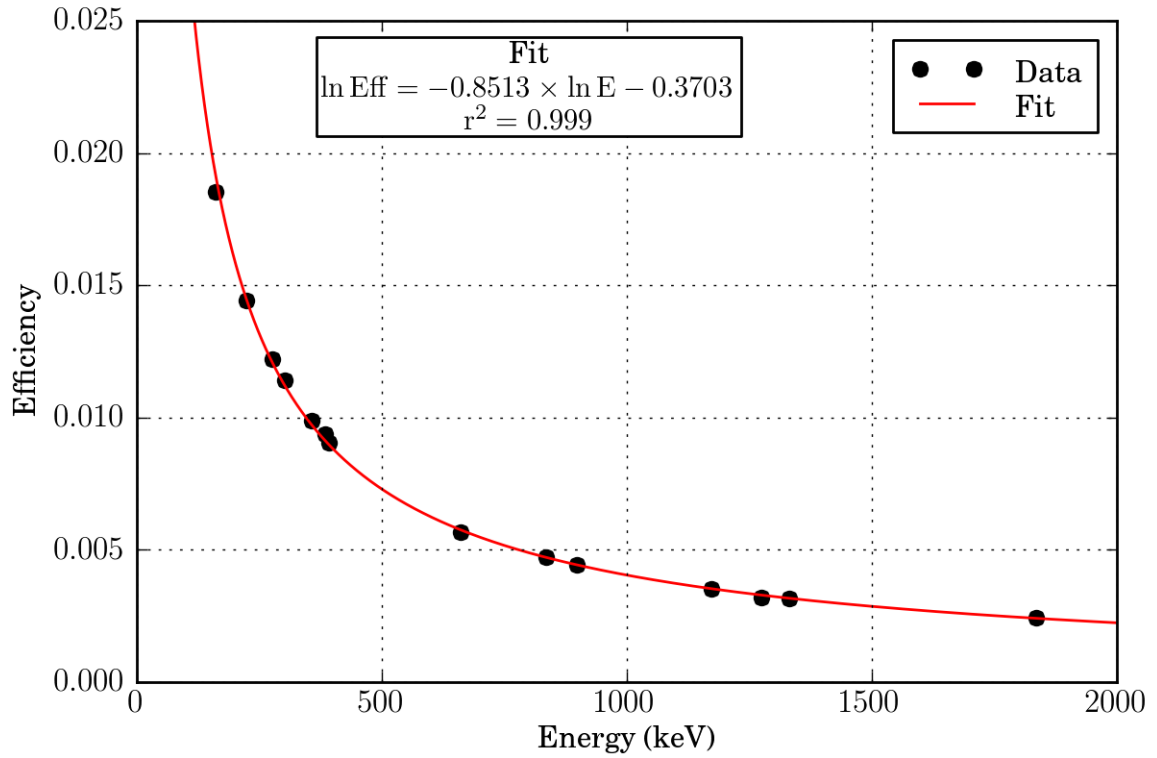
Figure 5.24: Efficiency calibration curve for the HPGe spectrometer used for the POWGEN foil irradiation.

Count Time

The count used for the analysis was started at 09:55:48.

Total Real Time: 541,748.00 $\pm$ 1 s ($\sim$ 150.5 hours)

Total Live Time: 528,300.00 $\pm$ 1 s ($\sim$ 146.8 hours)

Measured Candidate Peak and Expected Peaks Not Measured

The results of the gamma-ray spectrometry showed several peaks, but none of the peaks are due to threshold reactions. Several of the peaks were identified as background peaks, and the remainder were due to (n,γ) reactions on the indium and gold foils, and the residual ^{60}Co activity of the nickel foils (Table 5.3). This measurement is consistent with the autoradiograph, which showed no or low activity on all foils except gold, indium, and nickel.

The gamma-ray spectra data are inconsistent with a high-energy flux irradiation of the foils. Using the calculated POWGEN flux spectrum, many threshold reaction peaks were expected. The expected peaks not measured and their expected counts are listed in Table 5.4. The possible source of errors are discussed in the Section 6.2.

Nuclide (Foil)	Peak Energy keV	Nuclide (Background)	Peak Energy keV
^{116m}In	417.00	Annihilation	511.39
^{116m}In	1097.36		
^{116m}In	1293.69	^{40}K	1460.54
^{116m}In	1507.69		
^{116m}In	2112.24	^{214}Bi	1764.41
		^{214}Bi	1847.1
^{198}Au	411.69	^{214}Bi	2203.05
^{198}Au	675.89		
^{198}Au	1087.98	^{208}Tl	2615.72
^{60}Co	1173.54		
^{60}Co	1332.57		

Table 5.3: Candidate peaks

Nuclide	Peak Energy keV	Expected Counts	Nuclide	Peak Energy keV	Expected Counts
^{195}Au	98.85	73	^{56}Mn	846.77	1441
^{115m}In	336.24	30700	^{204}Bi	899.15	5768
^{196}Au	355.68	5973	^{202}Bi	960.67	597
^{201}Bi	629.1	212	^{48}Sc	983.52	340
^{206}Bi	803.1	21049	^{46}Sc	1120.55	313
^{58}Co	810.76	454	^{24}Na	1368.63	973
^{203}Bi	820.3	1761	^{205}Bi	1764.36	806
^{54}Mn	834.85	451			

Table 5.4: Expected peaks
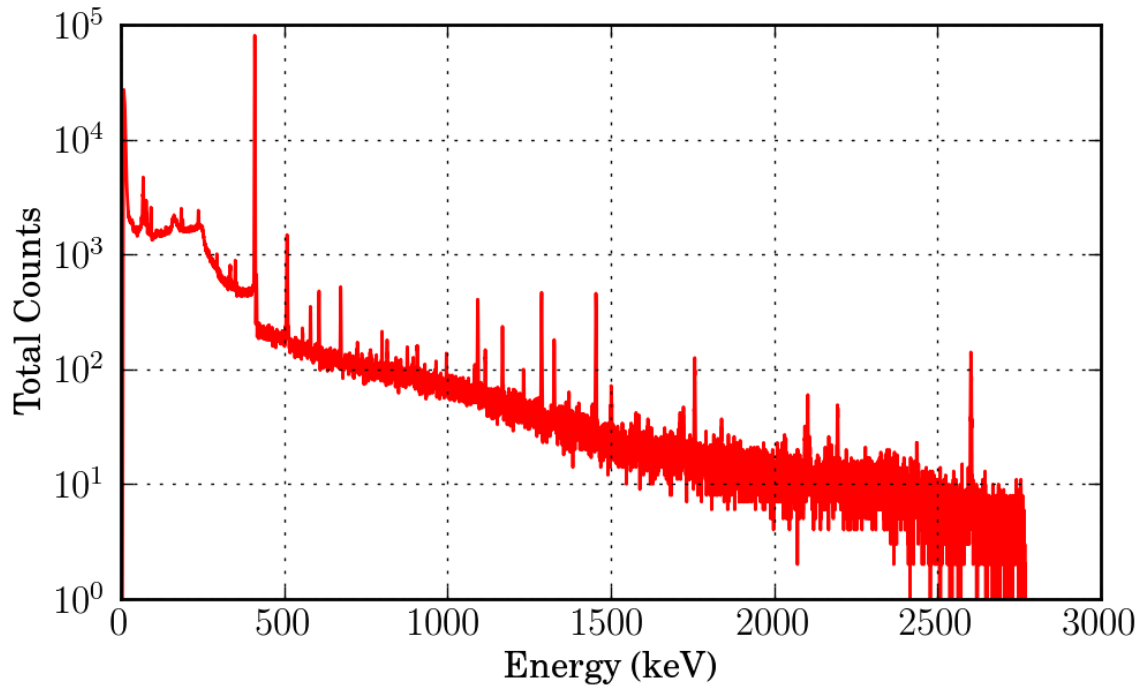
Figure 5.25: The POWGEN gamma spectrum
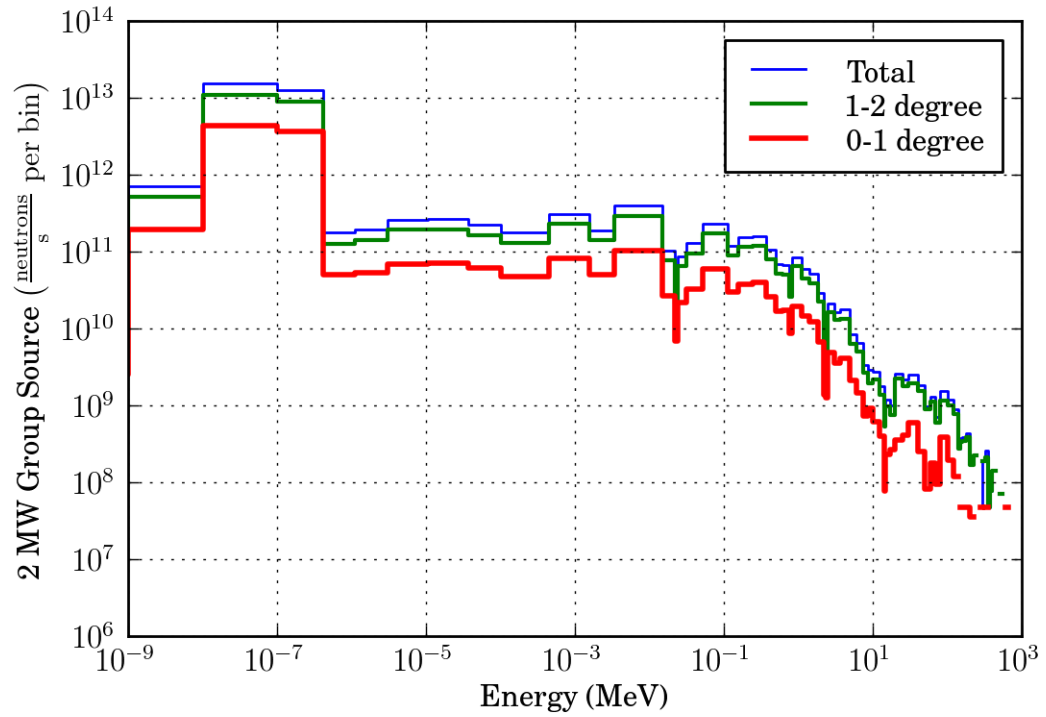
Figure 5.26: The POWGEN neutron source spectrum

5.2.4 Unfolding

Because threshold reaction activities were not measured, spectral unfolding could not be conducted for these data. The calculated POWGEN source spectrum that would have been used as the default spectrum and to generate the response functions is shown in Figure 5.26.

Chapter 6

Conclusions

The chapter presents conclusions drawn from the measurement results. Future work for improved measurements are also discused.

6.1 ARCS Measurements Conclusions

Based on the reanalyzed data and unfolding, the measured high-energy source term spectrum at ARCS is about 0.32 the calculated source term, therefore the measured flux is approximately 1/3 the calculated flux. The measured spectral shape differs noticeably from the calculated spectrum in the range of 25 MeV to 80 MeV. This energy range is where the computational models used to calculate the spectrum are known to perform relatively poorly [76]. Based on the calculated-to-measured ratios, the unfolded spectrum predicts the six reaction product activities precisely. Therefore the reanalyzed unfolded ARCS spectrum is should be regarded as an internally consistent measurement, which has yet to be validated by further measurements. It is a reasonable first step in the full measurement of the SNS high-energy flux spectrum, but it is not incontrovertible. Future and repeated measurements are necessary to draw conclusions with high confidence, but these measurements and analysis do not show gross disagreement with the calculated high-energy flux spectrum. These measurements indicated that a conservative source term was used for the shielding design.

The measurements performed at ARCS informed several improvements for sub-

sequent measurements. The gamma-ray spectrometry count time was limited by the use of a 7 L LN2 dewar. This dewar could not be refilled without removing it from the shield, thus causing a change in geometry and requiring recalibration. A larger 30 L dewar that could be refilled on-line replaced the smaller Dewar. This allowed the count time for the POWGEN foils to be longer by a factor of > 3.5. Experience with TCS issues and source calibration geometry also informed the subsequent measurements. At first, it was assumed that close measurement geometry would provide the best data because of the high geometric efficiency and high count rates. Only after several poor calibration curves were made was it realized that close geometry is difficult for accurate efficiency calibrations. For the POWGEN foil measurements, a sample holder was designed and used. This virtually eliminated TCS issues and enforced standardization of the calibration geometry with the sample geometry.

The ARCS measurements also informed the use of additional foils in the POWGEN measurements. Foils were added which offered threshold reactions spanning a broader energy range (e.g. ^{115}In(n,n')^{115m}In with a threshold at 340 keV) and reactions that overlapped other reactions (e.g gold (n,xn) reactions which overlap bismuth (n,xn) reactions). The ARCS gamma-ray spectrum file was saved several times during the count, which later proved to be useful for doing the time analysis and decay constant measurement. For the POWGEN measurement, periodic saving of the gamma-ray spectrum occurred every 15 minutes by a software script to improve the time analysis.

6.2   POWGEN Measurements Conclusions

The POWGEN foils gamma-ray spectrum results and the autoradiograph results point to an error in the experimental setup. Therefore, nothing can be concluded about the high-energy neutron flux spectrum from these data. It is useful for planning future measurements to consider what experimental error(s) are consistent with the observed data. The source of the experimental error may be deduced and avoided in future measurements

The gamma-ray spectrum and the autoradiograph indicated activation of the gold and indium foils. The gold and indium foils were in a stack that also included aluminum, cobalt, copper, iron, and titanium foils, but no activity from these foils was

measured with the gamma-ray spectrometer or autoradiograph. The gold and indium foils showed partial irradiation (a non-uniform spatial distribution) on the autoradiograph, and from the gamma-ray spectrum the origin of their activity is due to (n,γ) reactions, not threshold reactions.

One conceivable scenario is that the foils were exposed to a beam of thermal energy neutrons, but not a beam of high-energy neutrons. This is possible because a beam guide is in use at POWGEN. The beam guide directs thermal energy neutrons, but has no impact on high-energy neutrons, therefore two beam "footprints" are possible at the sample location. The foils could have been inside the thermal footprint, but not inside the high-energy footprint, thus thermal, but not high-energy, activation would have occurred. But this explanation is contradicted by other data. The lithium phosphate beam slits were reportedly fully closed, so no thermal beam should have been present. The position of the beam slits was confirmed in the data archive, although it is conceivable that the slit positions are false indications. If the slits were actually open and thermal energy beam did irradiate the foil stack, ^{60}Co from the cobalt foil (by the ^{59}Co(n,γ)^{60}Co reaction) should have been detected in the gamma-ray spectrum and on the autoradiograph. While ^{60}Co was detected in the gamma-ray spectrum, this is due entirely to the residual activity of the nickel foil. When measured separately, the cobalt foil showed no activity. Based on the evidence, thermal beam activation is not a consistent explanation.

Another conceivable explanation is that there is no measurable high-energy flux at the POWGEN sample location. If all sources of experimental error were eliminated, this explanation would be the most straightforward. And while this explanation cannot be negated, based on the expected counts of Table 5.4, the calculated POWGEN source term would be incorrect by orders of magnitude. For example, the highest expected number of counts was 30,000 due to ^{115m}In. All other factors remaining unchanged, if the spectrum was scaled by 0.001, a measurable number of counts should have been present in the gamma-ray spectrum. Similar arguments could be made for the expected counts due to ^{206}Bi and ^{196}Au. So while it is possible that high-energy flux is not present at POWGEN, the calculated spectrum would need to be grossly erroneous.

"Room return" is the phenomenon whereby radiation, typically neutrons, are reflected back from surrounding material. This effectively makes the walls, floors, and

ceiling of the beam room an additional source to consider. It is possible, that the foils were not exposed to any beam, and they were instead activated by the room return neutrons. Without modeling the surrounding structure, the magnitude of the room return cannot be easily gauged. While room return could explain the absence of high energy neutron activation on the foils, it cannot explain why only the gold and indium foils were activated. The room return explanation is also contradicted by the partial irradiation indicated on the autoradiograph. Room return is typically ambient, so a uniform irradiation of the foils is expected.

The most convincing explanation of the spectrometry and autoradiograph results is a failure with the T_0 chopper. The T_0 chopper, a large rotating block of inconel, is designed to stop the high-energy neutrons from traveling to the sample location. The T_0 chopper was allegedly stopped in the open position, allowing high-energy neutrons to pass. If the T_0 chopper continued to operate during these measurements, it would have blocked the high-energy neutrons, and the lithium phosphate slits would have blocked the thermal-energy neutrons. Only a beam of resonance-energy neutrons would have arrived at the sample site to irradiate the foils. These resonance-energy neutrons would have caused activation in the gold and indium (due to their relatively high resonance integrals), but not affected the other foils. The resonance-energy neutrons would be too high in energy for significant activation of cobalt through the $^{59}Co(n,\gamma)^{60}Co$ reaction (which has a low resonance integral), and they would be too low for threshold activation. While qualitatively this T_0 chopper failure theory appears to provide the most complete explanation, further modeling is required to provide a quantitative assessment of the theory.

6.3   Future Work

These measurements are the first in the attempt to quantify the high-energy neutron flux at the SNS. They have provided a basis to conduct future measurements, but several improvements can be made.

From an administrative perspective, the immediate objective of future work should be to preserve the knowledge advanced by this work. The entire method from foil selection, to irradiation, to gamma-ray spectrometric and autoradiography, to computa-
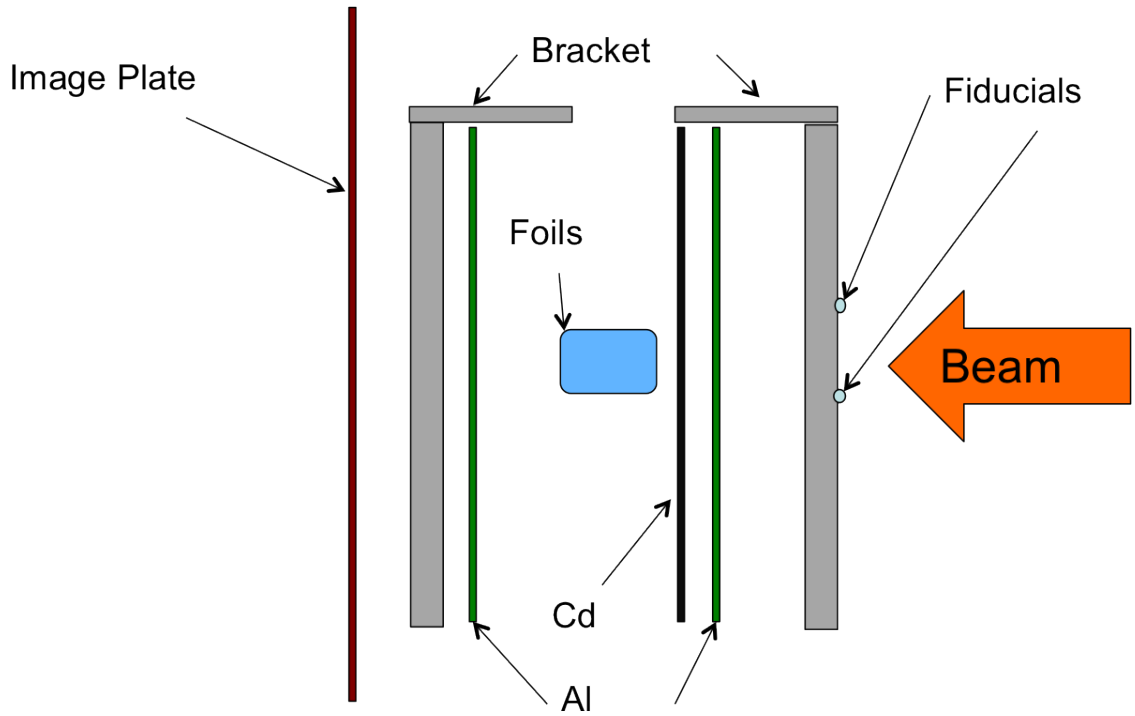
Figure 6.1: Exploded side view of a foil packet designed to address issues encountered with the POWGEN foil irradiation.

tional analysis needs to be codified into a repeatable process. While this document serves as a detailed guide to the work completed, more concise operation documentation is required. Several "HowTo" documents have been written, but these documents need to be vetted and revised. The computational work was conducted mostly on a personal computer, so software and auxiliary programs need to be transferred to systems accessible by SNS staff.

From an experimental standpoint, the next measurement should take place with a foil packet already designed and constructed for use. This foil packet attempts to address some of the issues encountered with the POWGEN foil irradiation (Figure 6.1). Two aluminum brackets form the structure of the packet, with metal fiducials (nuts on screws) mounted to the front. The metal fiducials are designed to cast bam shadows on the large ($\sim 12 \times 12$ cm) aluminum foils behind them, but not on the high-energy foil packet. The aluminum foils have enough area to fully contain the beam footprint, and they will be used for autoradiography immediately following irradiation. A cadmium plate (0.6 mm thick) is used as a thermal neutron cover to shield the high-energy foil packet and the rear

aluminum foil. The high-energy foil packet contains 9 types of foils and is similar to the packet used for the POWGEN measurement. Autoradiography on the rear aluminum foil should produce an image of the high-energy beam footprint (since it's behind the cadmium cover), while autoradiography on the forward aluminum foil should produce a footprint of both high-energy and thermal beam. The entire foil packet can be optionally used with a neutron-sensitive image plate placed to the rear for direct radiography of the beam footprint.

The newly constructed foil packet eliminates concerns of false indications of the lithium phosphate beam slits because the cadmium cover provides a local thermal beam filter. The large aluminum foils allow for radiography to commence in parallel with the gamma-ray spectrometry. The two foils would show any difference in location of the thermal and high-energy beam footprints. If this packet had been used for the POWGEN foil irradiation, it is likely that several additional data would have been used to deduce the source of the experimental error.

A second measurement at the ARCS beamline should be a priority. With more foils, higher beam power, longer irradiation, and more experience a second measurement would provide validation (or invalidation) of the unfolded spectrum already measured. If possible, two measurements should occur within a short time interval to minimize the likelihood of changes in conditions.

From an analysis perspective, the priority should be to unfold the spectrum using alternative algorithms. The most obvious choice is GRAVEL, since the software is already available with UMG. The IQU program could be used to propagate uncertainties from the activity measurements to the unfolded spectra. Additional metrics could be designed to judge the conformity of an output spectrum with a default spectrum. One example metric could be the difference in activity the two spectra produce in a sample material (*e.g.* stainless steel, concrete).

Beyond these near-term objectives, several broad goals can be envisioned. Measurement of the high-energy neutron flux using alternative means, such as a proton recoil telescope, could be used to confirm measurements made with foil activation. A software suite that merges response function generation, data collection of gamma-ray spectrometry, calculational corrections, and spectral unfolding could be produced.

6.4   General Conclusions

It was the goal of this work to develop a foil activation method to measure high-energy neutron flux spectra at the SNS by researching the scientific literature, assembling an experimental apparatus, performing experiments, analyzing the results, and refining the technique based on experience. This goal has been achieved. A method has been constructed, measurements were conducted, and techniques refined. The results remain to be validated by additional measurements, but this work has provided a framework and a foundation to conduct those future measurements.

Personally speaking, conducting this work has been enriching. When I began, I had classroom knowledge of topics like gamma-ray spectrometry and transport theory. My skills using MCNPX were basic, my knowledge of nuclear data was minimal, and my experimental experience was limited. I have traveled down many mental blind alleys while working on this topic. I have spent futile hours trying to track down the source of so many errors - computational, experimental, calculational. At times, it seemed impossible. But, also I've had small eureka moments when the code ran, the numbers agreed, and the measurement worked. Over time, I noticed that the number of mistakes I made has declined, and when I do make errors, I know how to recover from them faster. My skills and knowledge in spectrometry, transport theory, MCNPX, nuclear data, *etc.* have improved, but the most significant lesson has come from going through the entire process. This work accomplished a small engineering task at the Spallation Neutron Source, but it also provided me with an invaluable education and a deeply rewarding experience.

Bibliography

[1] F. X. Gallmeier, P. D. Ferguson, I. I. Popova, and E. B. Iverson, "The Spallation Neutron Source (SNS) project: a fertile ground for radiation protection and shielding challenges," *Radiation Protection Dosimetry*, vol. 115, pp. 23–32, Dec 2005.

[2] R. A. Lillie, F. X. Gallmeier, and J. O. Johnson, "HILO2K: Transport cross sections for neutron energies to 2 GeV," *Fourth International Topical Meeting on Nuclear Applications of Accelerator Technology, American Nuclear Society, Washington D.C.*, 2000.

[3] A. Trkov, March 2011. personal email communication.

[4] W. Lu, P. D. Ferguson, F. X. Gallmeier, E. B. Iverson, I. I. Popova, and Y. Wang, "A sample activation program for neutron-scattering experiments," *Nuclear Technology*, vol. 168, pp. 970–974, Dec 2009.

[5] G. J. Russell, E. J. Pitcher, G. Muhrer, F. Mezei, and P. D. Ferguson, *Fundamental Physics with Pulsed Neutron Beams*, ch. Overview of Spallation Neutron Source Physics, pp. 19–48. World Scientific, Jun 2000. Christopher R. Gould, Geoffrey L. Greene, Frank Plasil, William M. Snow, Eds.

[6] D. Filges and F. Goldenbaum, *Handbook of Spallation Research*. WILEY-VCH Verlag GmbH & Co. KGaA, 2009.

[7] K. H. Beckurts and K. Wirtz, *Neutron Physics*. Springer-Verlag, 1964.

[8] N. Tsoulfanidis, *Measurement and Detection of Radiation, Second Edition*. Taylor & Francis, 1995.

[9] M. J. Berger, J. H. Hubbell, S. M. Seltzer, J. Chang, J. S. Coursey, R. Sukumar, D. S. Zucker, and K. Olsen, "XCOM: photon cross sections database." http://www.nist.gov/pml/data/xcom/index.cfm, Oct 2011.

[10] G. Gilmore, *Practical Gamma-ray Spectrometry, 2nd Edition.* John Wiley & Sons, 2008.

[11] G. F. Knoll, *Radiation Detection and Measurement, Third Edition.* John Wiley & Sons, 2000.

[12] J. R. Taylor, *Introduction to Error Analysis, Second Edition.* University Science Books, 1997.

[13] Ortec, *GammaVision-32 Software User's Manual*, 6 ed., 2003.

[14] D. T. Bartlett, J. L. Chartier, M. Matzke, A. Rimpler, and D. J. Thomas, "Concepts and quantities in spectrometry and radiation protection.," *Radiation Protection Dosimetry*, vol. 107, no. 1-3, pp. 23–35, 2003.

[15] ASTM Standard E 262–08, "Standard test method for determining thermal neutron reaction rates and thermal neutron fluence rates by radioactivation techniques," March 2009.

[16] E. E. Lewis and W. F. M. Jr., *Computational Methods of Neutron Transport.* American Nuclear Society, Inc, 1993.

[17] L. K. Mansur and J. R. Haines, "Status of the spallation neutron source with focus on target materials," *Journal of Nuclear Materials*, vol. 356, pp. 1–15, Sept 2006.

[18] T. A. Gabriel, *Fundamental Physics with Pulsed Neutron Beams*, ch. Spallation Neutron Source With Emphasis on Target Systems, pp. 1–18. World Scientific, Jun 2000. Christopher R. Gould, Geoffrey L. Greene, Frank Plasil, William M. Snow, Eds.

[19] F. X. Gallmeier, P. D. Ferguson, and E. B. Iverson, "Radiation environment for the replacement scenario of the activated SNS core vessel inserts," *ICANS-XVI 16th Meeting of the International Collaboration on Advanced Neutron Sources, Düsseldorf-Neuss, Germany*, May 2003.

[20] D. Abernathy, "ARCS: a wide angular-range chopper spectrometer at the SNS," *Notiziario Neutroni E Luce di Sincrotrone*, vol. 13, pp. 4–7, Jan 2008.

[21] T. E. Mason, D. Abernathy, I. Anderson, J. Ankner, T. Egami, G. Ehlers, A. Ekkebus, G. Granroth, M. Hagen, K. Herwig, J. Hodges, C. Hoffmann, C. Horak, L. Horton, F. Klose, J. Larese, A. Mesecar, D. Myles, J. Neuefeind, M. Ohl, C. Tulk, X.-L. Wang, and J. Zhao, "The Spallation Neutron Source in Oak Ridge: A powerful tool for materials research," *Physica B*, vol. 385-386, pp. 955–960, Nov 2006.

[22] G. Lovestam, M. Hult, A. Fessler, J. Gasparro, P. Kockerols, K. Okkinga, H. Tagziria, F. Vanhavere, and J. S. E. Wieslander, "Neutron fluence spectrometry using disk activation," *Radiation Measurements*, vol. 44, pp. 72–79, Jan 2009.

[23] E. Kim, T. Nakamura, A. Konno, Y. Uwamino, N. Nakanishi, M. Imamura, N. Nakao, S. Shibata, and S. Tanaka, "Measurements of neutron spallation cross sections of C-12 and Bi-209 in the 20- to 150-MeV energy range," *Nuclear Science and Engineering*, vol. 129, pp. 209–223, Jul 1998.

[24] M. B. Chadwick, H. G. Hughes, R. C. Little, E. J. Pitcher, and P. G. Young, "Nuclear data for accelerator-driven systems," *Progress in Nuclear Energy*, vol. 38, no. 1-2, pp. 179–219, 2001.

[25] T. Nunomiya, N. Nakao, P. Wright, T. Nakamura, E. Kim, T. Kurosawa, S. Taniguchi, M. Sasaki, H. Iwase, Y. Uwamino, T. Shibata, S. Ito, and D. R. Perry, "Measurement of deep penetration of neutrons produced by 800-MeV proton beam through concrete and iron at ISIS," *Nuclear Instruments and Methods in Physics Research Section B*, vol. 179, pp. 89–102, Jun 2001.

[26] J. Adam, A. R. Balabekyan, V. S. Barashenkov, R. Brandt, V. M. Golovatiouk, V. G. Kalinnikov, K. Katovsky, M. I. Krivopustov, V. Kumar, H. Kumawat, R. Odoj, V. S. Pronskikh, A. A. Solnyshkin, V. I. Stegailov, V. M. Tsoupko-Sitnikov, and W. West-meier, "Spallation neutron spectrum on a massive lead/paraffin target irradiated with 1 GeV protons," *The European Physical Journal A*, vol. 23, pp. 61–68, 2005.

[27] E. Jerde, D. Glasgow, and J. Hastings, "Neutron activation by neutrons produced via proton-induced spallation in a liquid-mercury target: Measurements and assessment of uncertainties," *Journal of Radioanalytical and Nuclear Chemistry*, vol. 242, pp. 473–485, 1999.

[28] J. Sisterson and J. Ullmann, "Measurements of energy integrated cross sections for reactions producing relatively short-lived radionuclides using neutron beams with an energy range of 0.1–750 MeV," *Nuclear Instruments and Methods in Physics Research Section B*, vol. 234, pp. 419–430, Jul 2005.

[29] ASTM Standard E 523–11, "Standard test method for measuring fast-neutron reaction rates by radioactivation of copper," June 2011.

[30] E. J. Kim, T. Nakamura, Y. Uwamino, N. Nakanishi, M. Imamura, N. Nakao, S. Shibata, and S. Tanaka, "Measurements of activation cross sections on spallation reactions for Co-59 and Cu-nat at incident neutron energies of 40 to 120 MeV," *Journal of Nuclear Science and Technology*, vol. 36, no. 1, pp. 29–40, 1999.

[31] ASTM Standard E 264–08, "Standard test method for measuring fast-neutron reaction rates by radioactivation of nickel," July 2008.

[32] Y. Liu, S. Nievaart, H. Liu, R. Moss, and S. Jiang, "Monte Carlo determined self-shielded groupwise cross-sections for the activation foil stack applied in the epithermal neutron spectrum adjustment," *Nuclear Instruments and Methods in Physics Research A*, vol. 602, pp. 557–563, Apr 2009.

[33] S. A. Jonah and K. Ibikunle, "Neutron spectral distribution from a sealed-tube neutron generator by multiple-foil activation unfolding method," *Nuclear Instruments and Methods in Physics Research Section A*, vol. 501, pp. 514–516, Apr 2003.

[34] S. Endo, E. Yoshida, Y. Yoshitake, W. Zhang, K. Fujikawa, T. Itoh, M. Ishikawa, M. Hoshi, and K. Shizuma, "Neural networks for the neutron spectrum determination based on the foil activation method," *Japanese Journal of Applied Physics 1*, vol. 41, pp. 2191–2194, Apr 2002.

[35] ASTM Standard E 266–11, "Standard test method for measuring fast-neutron reaction rates by radioactivation of aluminum," June 2011.

[36] Y. Uno, Y. Uwamino, T. S. Soewarsono, and T. Nakamura, "Measurement of the neutron activation cross sections of C-12, Si-30, Ti-47, Ti-48, Cr-52, (CO)-C-59, and Ni-58 between 15 and 40 MeV," *Nuclear Science and Engineering*, vol. 122, pp. 247–257, Feb 1996.

[37] C. C. Negoita, *Measurement of Neutron Flux Spectra in a Tungsten Benchmark by Neutron Foil Activation Method.* PhD thesis, Der Technischen Universitat Dresden, 2004.

[38] ASTM Standard E 263–09, "Standard test method for measuring fast-neutron reaction rates by radioactivation of iron," June 2009.

[39] ASTM Standard E 526–08, "Standard test method for measuring fast-neutron reaction rates by radioactivation of titanium," July 2008.

[40] ASTM Standard E 261–10, "Standard practice for determining neutron fluence, fluence rate, and spectra by radioactivation techniques," January 2010.

[41] Ortec, "GEM series coaxial HPGe detector product configuration guide." http://www.ortec-online.com/download/HPGe%20Germanium%20GEM%20Detectors.pdf, 2011.

[42] Ortec, "Gem high-purity germanium (HPGe) coaxial detectors (in PopTop capsule)." http://www.ortec-online.com/detectors/photon/b2_1.htm, May 2009.

[43] R. Keyser, August 2011. personal email communication.

[44] M. Chadwick, P. Oblozinsky, M. Herman, N. Greene, R. Mcknight, D. Smith, P. Young, R. Macfarlane, G. Hale, and S. Frankle, "ENDF/B-VII.0: Next generation evaluated nuclear data library for nuclear science and technology," *Nuclear Data Sheets*, vol. 107, pp. 2931–3060, Dec 2006.

[45] M. Chadwick, P. Young, S. Chiba, S. Frankle, G. Hale, H. Hughes, A. Koning, R. Little, R. MacFarlane, R. Prael, and L. Waters, "Cross-section evaluations to 150 MeV

for accelerator-driven systems and implementation in MCNPX," *Nuclear Science and Engineering*, vol. 131, pp. 293–328, Mar 1999.

[46] D. Rochman and A. J. Koning, "TENDL-2009: on evaluations and Monte Carlo covariances." White paper, Nuclear Research and Consultancy Group NRG, September 2009. Available online, `ftp://ftp.nrg.eu/pub/www/talys/tendl-2009beta/Document/tendl2009_web.pdf`.

[47] J.-C. Sublet, L. W. Packer, J. Kopecky, R. A. Forrest, A. J. Koning, and D. A. Rochman, "Activation File: EAF-2010 neutron-induced cross section library." White paper, EURATOM/CCFE Fusion Association, April 2010. Available online, `http://www.ccfe.ac.uk/EASY-data/eaf2010/Docs/EAF_n_Cross_sections_2010.pdf`.

[48] J.-C. Sublet, March 2011. personal email communication.

[49] Y. Watanabe, K. Kosako, S. Kunieda, S. Chiba, R. Fujimoto, H. Harada, M. Kawai, F. Maekawa, T. Murata, H. Nakashima, K. Niita, N. Shigyo, S. Shimakawa, N. Yamano, and T. Fukahori, "Status of JENDL high energy file," *Journal of Korean Physical Society*, vol. 59, pp. 1040–1045, Aug 2011.

[50] R. A. Lillie and F. X. Gallmeier, "HIL02k: A coupled neutron-photon transport cross section library for neutron energies up to 2000 MeV," *Proceedings of the Fourth International Topical Meeting on Nuclear Applications of Accelerator Technology, Washington DC, USA*, 2000.

[51] Los Alamos National Laboratory, *MCNPX User's Manual*, 2.6.0 ed., April 2008.

[52] Los Alamos National Laboratory, *MCNP – A General Monte Carlo N-Particle Transport Code, Volume I: Overview and Theory*, 5 ed., February 2008.

[53] M. Reginatto, P. Goldhagen, and S. Neumann, "Spectrum unfolding, sensitivity analysis and propagation of uncertainties with the maximum entropy deconvolution code MAXED," *Nuclear Instruments and Methods in Physics Research Section A*, vol. 476, pp. 242–246, Jan 2002.

[54] L. F. Miller, February 2011. personal communication.

[55] M. Reginatto and P. Goldhagen, "MAXED, a computer code for the deconvolution of multisphere neutron spectrometer data using the maximum entropy method," Technical Report EML-595, Environmental Measurements Laboratory, U.S. Department of Energy, 201 Varick Street, 5th Floor, New York, NY 10014-4811, June 1998.

[56] W. H. Press, S. A. Teukolsky, W. T. Vetterling, and B. P. Flannery, *Numerical Recipes in Fortran 77: The Art of Scientific Computing, Second Edition.* Press Syndicate of the University of Cambridge, 1992. Available online, http://apps.nrbook.com/fortran/index.html.

[57] W. Goffe, "SIMANN: a global optimization algorithm using simulated annealing," *Studies in Nonlinear Dynamics and Econometrics*, vol. 1, pp. 169–176, Oct 1996.

[58] Physikalisch-Technische Bundesanstalt PTB, *UMG FC Manual*, 3.3 ed., 2004.

[59] M. Matzke, "Propagation of uncertainties in unfolding procedures," *Nuclear Instruments and Methods in Physics Research Section A*, vol. 476, pp. 230–241, Jan 2002.

[60] R. Koohi-Fayegh, S. Green, and M. Scott, "A comparison of neutron spectrum unfolding codes used with a miniature NE213 detector," *Nuclear Instruments and Methods in Physics Research A*, vol. 460, pp. 391–400, Mar 2001.

[61] C. Braga and M. Dias, "Application of neural networks for unfolding neutron spectra measured by means of Bonner spheres," *Nuclear Instruments and Methods in Physics Research A*, vol. 476, pp. 252–255, Jan 2002.

[62] H. Vega-Carrillo, V. Martin-Hernàndez-Dàvila, E. M. Acuna, G. Mercado-Sànchez, M. P. I. de la Torre, R. Barquero, F. Palacios, R. M. Villafane, T. A. Arteaga, and J. M. O. Rodriguez, "Neutron spectrometry using artificial neural networks," *Radiation Measurements*, vol. 41, pp. 425–431, Apr 2006.

[63] D. W. Freeman, D. R. Edwards, and A. E. Bolon, "Genetic algorithms - a new technique for solving the neutron spectrum unfolding problem," *Nuclear Instruments and Methods in Physics Research Section A*, vol. 425, pp. 549–576, Apr 1999.

[64] B. Mukherjee, "A high-resolution neutron spectra unfolding method using the genetic algorithm technique," *Nuclear Instruments and Methods in Physics Research Section A*, vol. 476, pp. 247–251, Jan 2002.

[65] S. P. Tripathy, C. Sunil, M. Nandy, P. K. Sarkar, D. N. Sharma, and B. Mukherjee, "Activation foils unfolding for neutron spectrometry: Comparison of different deconvolution methods," *Nuclear Instruments and Methods in Physics Research Section A*, vol. 583, pp. 421–425, Dec 2007.

[66] A. Esposito and M. Nandy, "Measurement and unfolding of neutron spectra using Bonner spheres," *Radiation Protection Dosimetry*, vol. 110, no. 1-4, pp. 555–558, 2004.

[67] M. Matzke, "Unfolding procedures," *Radiation Protection Dosimetry*, vol. 107, no. 1–3, pp. 155–174, 2003.

[68] A. Seghour and F. Z. Seghour, "Unfolding neutron energy spectra from foil activation detector measurements with the gold algorithm," *Nuclear Instruments and Methods in Physics Research Section A*, vol. 457, pp. 617–626, Jan 2001.

[69] J. V. Roulti and J. V. Sandberg, "Unfolding activation and multisphere detector data," *Radiation Protection Dosimetry*, vol. 10, no. 1-4, pp. 103–110, 1985.

[70] M. Matzke and K. Weise, "Neutron-spectrum unfolding by the Monte-Carlo method," *Nuclear Instruments and Methods in Physics Research Section A*, vol. 234, pp. 324–330, Feb 1985.

[71] A. Seghour and F. Z. Seghour, "Neutron energy spectra unfolding from foil activation detector measurements with minuit," *Nuclear Instruments and Methods in Physics Research Section A*, vol. 555, pp. 347–355, Dec 2005.

[72] Eckert & Ziegler, "Reference & calibration sources product information." http://www.ezag.com/, Oct 2011.

[73] K. Kasemir, September 2011. personal email communication.

[74] F. X. Gallmeier, "Source Terms for Neutron Beamline Shielding and Activation Calculations," Technical Report SNS-107030700-DA0002-R00, Spallation Neutron Source, February 2005.

[75] N. Luciano and E. B. Iverson, "High-energy neutron flux spectra measurements using foil activation at the spallation neutron source," *Tenth International Topical Meeting on Nuclear Applications of Accelerator Technology, Knoxville, TN.*, 2011.

[76] F. X. Gallmeier, November 2011. personal communication.

Appendix A

Units and Constants

Units (Conversions to *Systéme International* base units are provided.)

b barn $= 10^{-28}$ m^2

C Coloumb $= 1$ Ampere $\cdot$ s

Ci Curie $= 3.7 \times 10^{10}$ $\frac{\text{decays}}{\text{s}}$

eV electron-volt $= 1.602176565(3) \times 10^{-19}$ $\frac{\text{kg} \cdot \text{m}^2}{\text{s}}$

g gram $= 10^{-3}$ kg

Hz Hertz $= 1$ $\frac{\text{cycles}}{\text{s}}$

in inches $= 2.54 \times 10^{-2}$ m

K Kelvin

L Liter $= 10^{-3}$ m^3

m meter

s second

W Watt $= 1$ $\frac{\text{kg} \cdot \text{m}^2}{\text{s}^3}$

Constants

k $= 1.3806488(13) \times 10^{-23}$ $\frac{\text{kg} \cdot \text{m}^2}{\text{s} \cdot \text{K}}$ (Boltzmann Constant)

Appendix B

Experimental Foils

Image	Material	Beamlines	Radius (measured)	Mass (measured)	Thickness (calculated)
in			cm	g	cm
	Aluminum	ARCS POWGEN	0.64(0)	0.175(2) 0.174(5) 0.175(7)	0.0498
	Bismuth	ARCS POWGEN	0.49(5)	7.581(8) 7.581(9)	1.00
	Cobalt	POWGEN	0.5(0)	0.173(9)	0.0249
	Copper	ARCS POWGEN	0.64(0)	0.152(1)	0.0132
	Gold	POWGEN	0.5(0)	0.369(1)	0.0243
	Indium	POWGEN	0.5(0)	0.570(1)	0.0993
	Iron	POWGEN	0.5(0)	0.613(6)	0.0991
	Nickel	ARCS POWGEN	0.64(0)	0.014(5) 0.014(0) 0.013(8)	0.0012
	Titanium	POWGEN	0.5(0)	0.350(4)	0.0989

Table B.1: Foils irradiated at ARCS and POWGEN. Where multiple mass values are listed, each value indicates a single foil.

Appendix C

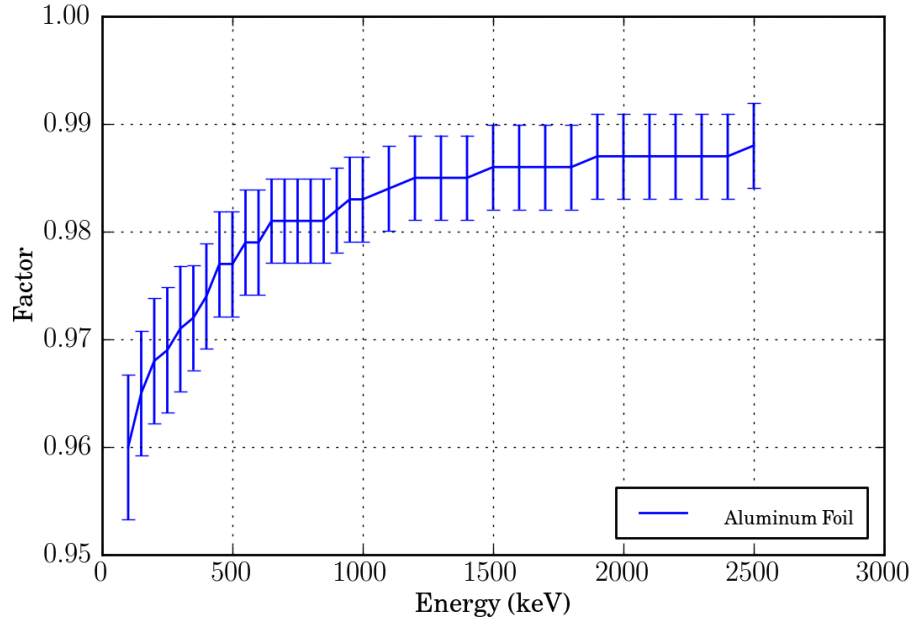# Foil Gamma-ray Self-Shielding Factors

Figure C.1: Gamma-ray self-shielding factors for the aluminum foil listed in Table B.1. Error bars represent absolute standard error.

Gamma-ray Energy keV	Self-Shielding Factor	MCNPX RSE	Gamma-ray Energy keV	Self-Shielding Factor	MCNPX RSE
100	0.9600	0.007	950	0.9830	0.004
150	0.9650	0.006	1000	0.9830	0.004
200	0.9680	0.006	1100	0.9840	0.004
250	0.9690	0.006	1200	0.9850	0.004
300	0.9710	0.006	1300	0.9850	0.004
350	0.9720	0.005	1400	0.9850	0.004
400	0.9740	0.005	1500	0.9860	0.004
450	0.9770	0.005	1600	0.9860	0.004
500	0.9770	0.005	1700	0.9860	0.004
550	0.9790	0.005	1800	0.9860	0.004
600	0.9790	0.005	1900	0.9870	0.004
650	0.9810	0.004	2000	0.9870	0.004
700	0.9810	0.004	2100	0.9870	0.004
750	0.9810	0.004	2200	0.9870	0.004
800	0.9810	0.004	2300	0.9870	0.004
850	0.9810	0.004	2400	0.9870	0.004
900	0.9820	0.004	2500	0.9880	0.004

Table C.1: Gamma-ray self-shielding factors for the aluminum foil listed in Table B.1. Error bars represent absolute standard error.
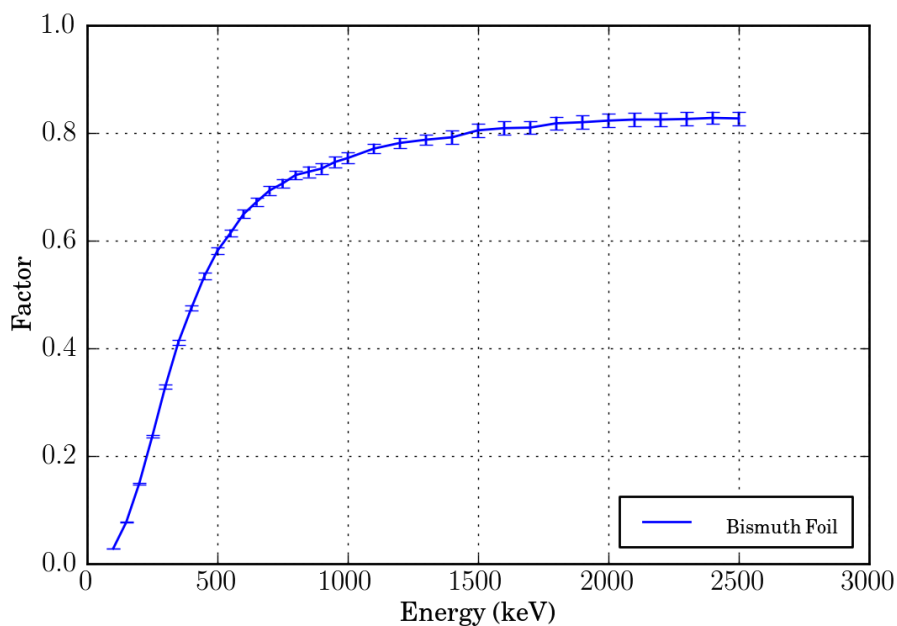
Figure C.2: Gamma-ray self-shielding factors for the bismuth foil listed in Table B.1. Error bars represent absolute standard error.

Gamma-ray Energy keV	Self-Shielding Factor	MCNPX RSE	Gamma-ray Energy keV	Self-Shielding Factor	MCNPX RSE
100	0.0281	0.016	950	0.7460	0.013
150	0.0770	0.013	1000	0.7535	0.013
200	0.1491	0.011	1100	0.7710	0.012
250	0.2367	0.011	1200	0.7815	0.012
300	0.3292	0.011	1300	0.7875	0.012
350	0.4113	0.011	1400	0.7920	0.016
400	0.4749	0.011	1500	0.8050	0.016
450	0.5341	0.011	1600	0.8090	0.015
500	0.5813	0.011	1700	0.8100	0.015
550	0.6142	0.011	1800	0.8180	0.015
600	0.6493	0.012	1900	0.8200	0.015
650	0.6720	0.011	2000	0.8230	0.015
700	0.6933	0.012	2100	0.8250	0.015
750	0.7063	0.012	2200	0.8250	0.015
800	0.7220	0.011	2300	0.8260	0.015
850	0.7280	0.014	2400	0.8280	0.014
900	0.7340	0.014	2500	0.8270	0.015

Table C.2: Gamma-ray self-shielding factors for the bismuth foil listed in Table B.1. Error bars represent absolute standard error.
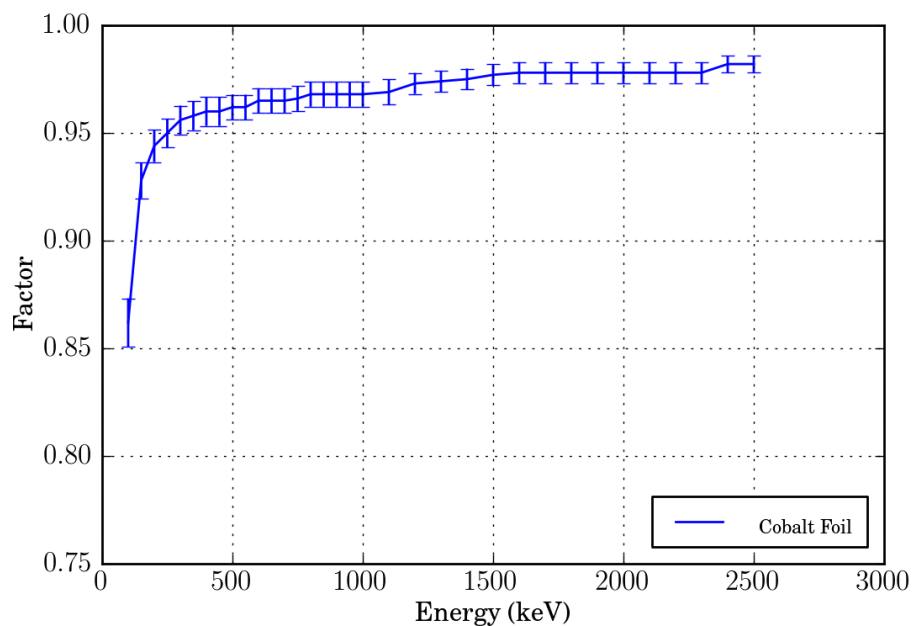
Figure C.3: Gamma-ray self-shielding factors for the cobalt foil listed in Table B.1. Error bars represent absolute standard error.

Gamma-ray Energy keV	Self-Shielding Factor	MCNPX RSE	Gamma-ray Energy keV	Self-Shielding Factor	MCNPX RSE
100	0.8620	0.013	950	0.9680	0.006
150	0.9280	0.009	1000	0.9680	0.006
200	0.9440	0.008	1100	0.9690	0.006
250	0.9500	0.007	1200	0.9730	0.005
300	0.9560	0.007	1300	0.9740	0.005
350	0.9580	0.007	1400	0.9750	0.005
400	0.9600	0.007	1500	0.9770	0.005
450	0.9600	0.007	1600	0.9780	0.005
500	0.9620	0.006	1700	0.9780	0.005
550	0.9620	0.006	1800	0.9780	0.005
600	0.9650	0.006	1900	0.9780	0.005
650	0.9650	0.006	2000	0.9780	0.005
700	0.9650	0.006	2100	0.9780	0.005
750	0.9660	0.006	2200	0.9780	0.005
800	0.9680	0.006	2300	0.9780	0.005
850	0.9680	0.006	2400	0.9820	0.004
900	0.9680	0.006	2500	0.9820	0.004

Table C.3: Gamma-ray self-shielding factors for the cobalt foil listed in Table B.1. Error bars represent absolute standard error.
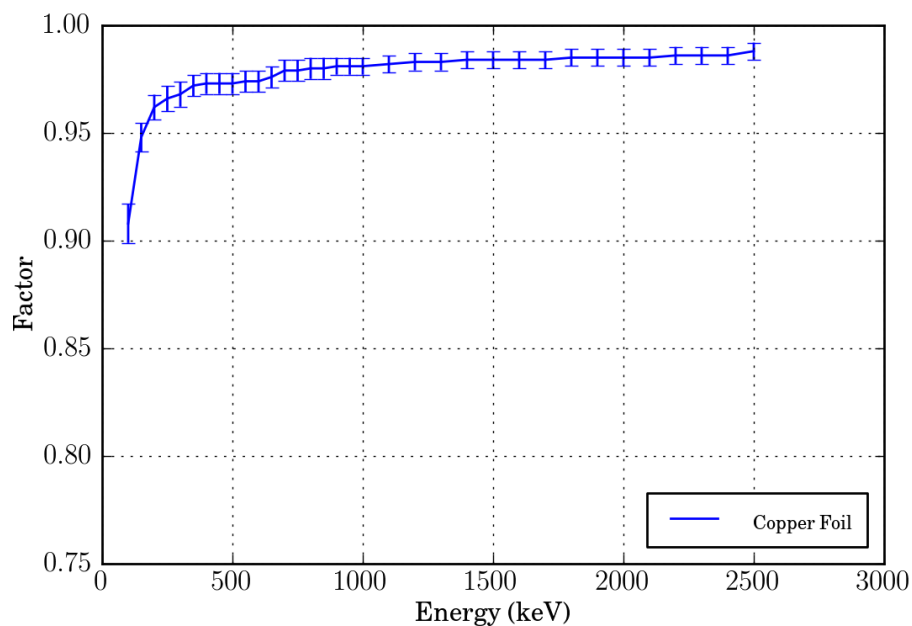
Figure C.4: Gamma-ray self-shielding factors for the copper foil listed in Table B.1. Error bars represent absolute standard error.

Gamma-ray Energy keV	Self-Shielding Factor	MCNPX RSE	Gamma-ray Energy keV	Self-Shielding Factor	MCNPX RSE
100	0.9080	0.010	950	0.9810	0.004
150	0.9480	0.007	1000	0.9810	0.004
200	0.9620	0.006	1100	0.9820	0.004
250	0.9660	0.006	1200	0.9830	0.004
300	0.9680	0.006	1300	0.9830	0.004
350	0.9720	0.005	1400	0.9840	0.004
400	0.9730	0.005	1500	0.9840	0.004
450	0.9730	0.005	1600	0.9840	0.004
500	0.9730	0.005	1700	0.9840	0.004
550	0.9740	0.005	1800	0.9850	0.004
600	0.9740	0.005	1900	0.9850	0.004
650	0.9760	0.005	2000	0.9850	0.004
700	0.9790	0.005	2100	0.9850	0.004
750	0.9790	0.005	2200	0.9860	0.004
800	0.9800	0.005	2300	0.9860	0.004
850	0.9800	0.005	2400	0.9860	0.004
900	0.9810	0.004	2500	0.9880	0.004

Table C.4: Gamma-ray self-shielding factors for the copper foil listed in Table B.1. Error bars represent absolute standard error.
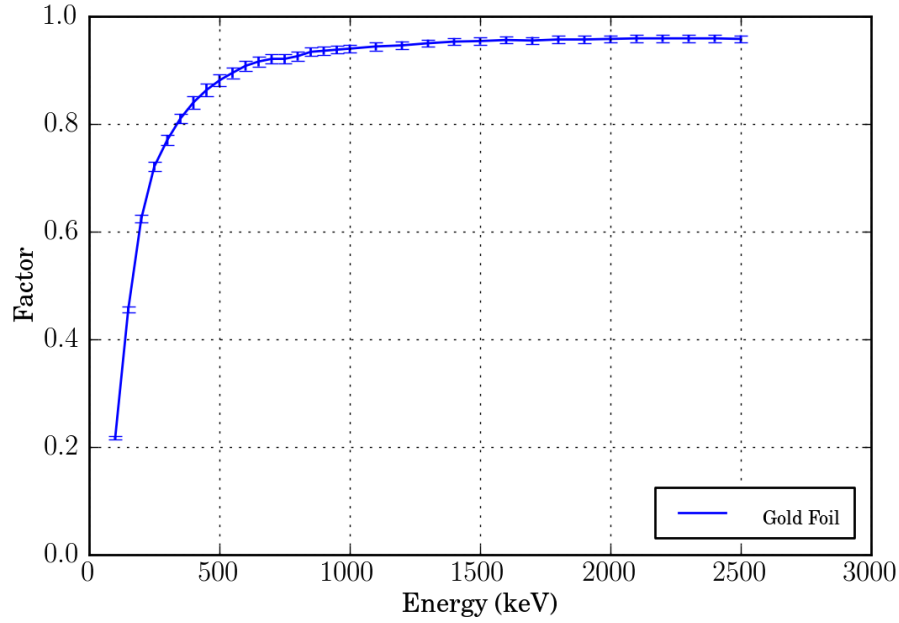
Figure C.5: Gamma-ray self-shielding factors for the gold foil listed in Table B.1. Error bars represent absolute standard error.

Gamma-ray Energy keV	Self-Shielding Factor	MCNPX RSE	Gamma-ray Energy keV	Self-Shielding Factor	MCNPX RSE
100	0.2169	0.016	950	0.9380	0.008
150	0.4553	0.013	1000	0.9400	0.008
200	0.6240	0.012	1100	0.9440	0.008
250	0.7210	0.011	1200	0.9460	0.008
300	0.7705	0.012	1300	0.9500	0.007
350	0.8100	0.011	1400	0.9530	0.007
400	0.8400	0.014	1500	0.9540	0.007
450	0.8630	0.013	1600	0.9560	0.007
500	0.8810	0.012	1700	0.9550	0.007
550	0.8950	0.011	1800	0.9570	0.007
600	0.9080	0.010	1900	0.9570	0.007
650	0.9160	0.010	2000	0.9580	0.007
700	0.9210	0.009	2100	0.9590	0.007
750	0.9210	0.009	2200	0.9590	0.007
800	0.9260	0.009	2300	0.9590	0.007
850	0.9340	0.008	2400	0.9590	0.007
900	0.9360	0.008	2500	0.9580	0.007

Table C.5: Gamma-ray self-shielding factors for the gold foil listed in Table B.1. Error bars represent absolute standard error.
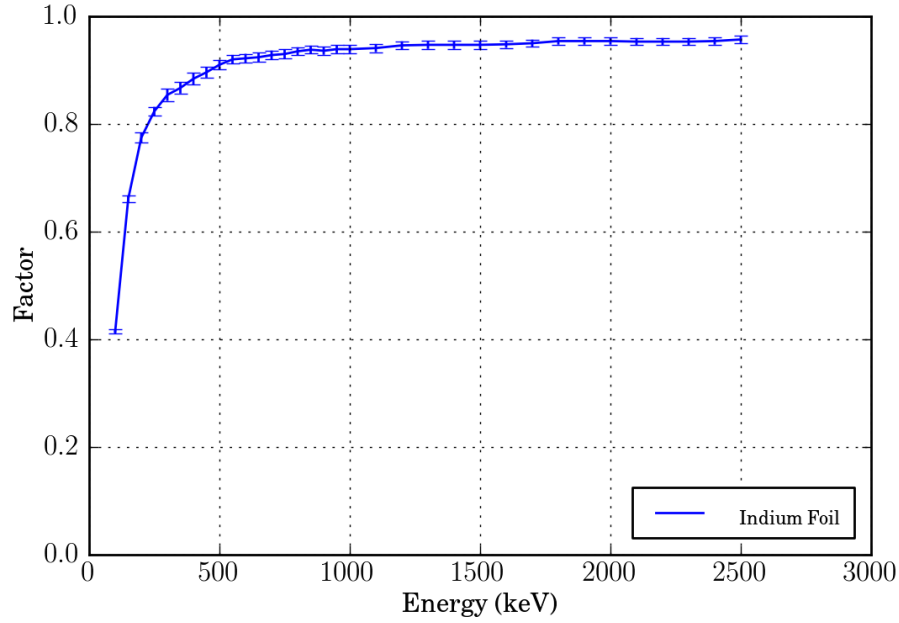
Figure C.6: Gamma-ray self-shielding factors for the indium foil listed in Table B.1. Error bars represent absolute standard error.

Gamma-ray Energy keV	Self-Shielding Factor	MCNPX RSE	Gamma-ray Energy keV	Self-Shielding Factor	MCNPX RSE
100	0.4147	0.010	950	0.9390	0.008
150	0.6608	0.010	1000	0.9390	0.008
200	0.7745	0.012	1100	0.9410	0.008
250	0.8235	0.010	1200	0.9460	0.008
300	0.8540	0.013	1300	0.9470	0.008
350	0.8670	0.012	1400	0.9470	0.008
400	0.8840	0.012	1500	0.9470	0.008
450	0.8960	0.011	1600	0.9480	0.007
500	0.9100	0.010	1700	0.9500	0.007
550	0.9200	0.009	1800	0.9540	0.007
600	0.9220	0.009	1900	0.9540	0.007
650	0.9240	0.009	2000	0.9540	0.007
700	0.9280	0.009	2100	0.9530	0.007
750	0.9300	0.009	2200	0.9530	0.007
800	0.9350	0.008	2300	0.9530	0.007
850	0.9380	0.008	2400	0.9540	0.007
900	0.9360	0.008	2500	0.9570	0.007

Table C.6: Gamma-ray self-shielding factors for the indium foil listed in Table B.1. Error bars represent absolute standard error.
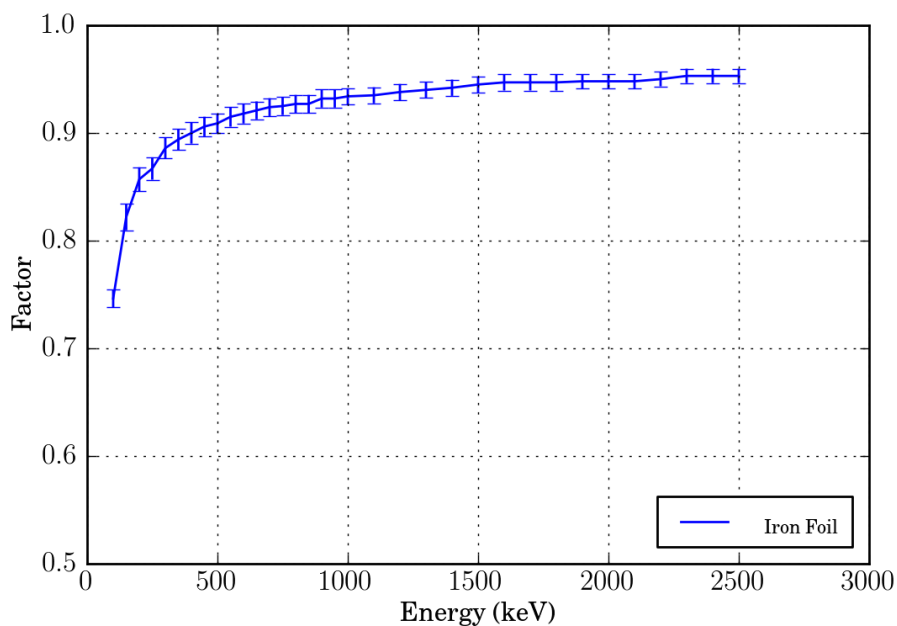
Figure C.7: Gamma-ray self-shielding factors for the iron foil listed in Table B.1. Error bars represent absolute standard error.

Gamma-ray Energy keV	Self-Shielding Factor	MCNPX RSE	Gamma-ray Energy keV	Self-Shielding Factor	MCNPX RSE
100	0.7463	0.011	950	0.9320	0.009
150	0.8220	0.015	1000	0.9340	0.008
200	0.8570	0.013	1100	0.9350	0.008
250	0.8670	0.012	1200	0.9380	0.008
300	0.8860	0.011	1300	0.9400	0.008
350	0.8940	0.011	1400	0.9420	0.008
400	0.9000	0.011	1500	0.9450	0.008
450	0.9060	0.010	1600	0.9470	0.008
500	0.9090	0.010	1700	0.9470	0.008
550	0.9150	0.010	1800	0.9470	0.008
600	0.9180	0.010	1900	0.9480	0.007
650	0.9210	0.009	2000	0.9480	0.007
700	0.9240	0.009	2100	0.9480	0.007
750	0.9250	0.009	2200	0.9500	0.007
800	0.9270	0.009	2300	0.9530	0.007
850	0.9270	0.009	2400	0.9530	0.007
900	0.9320	0.009	2500	0.9530	0.007

Table C.7: Gamma-ray self-shielding factors for the iron foil listed in Table B.1. Error bars represent absolute standard error.
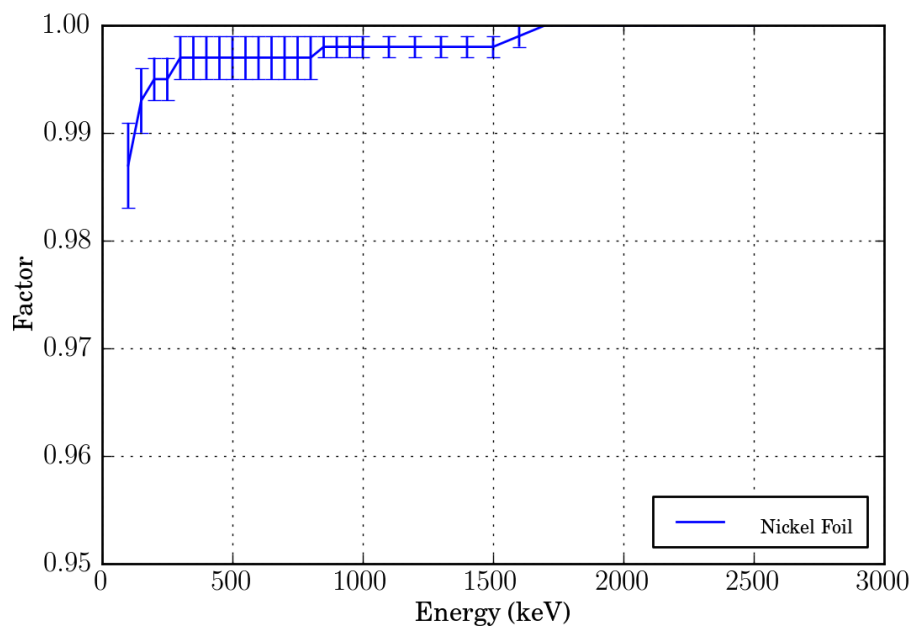
Figure C.8: Gamma-ray self-shielding factors for the nickel foil listed in Table B.1. Error bars represent absolute standard error.

Gamma-ray Energy keV	Self-Shielding Factor	MCNPX RSE	Gamma-ray Energy keV	Self-Shielding Factor	MCNPX RSE
100	0.9870	0.004	950	0.9980	0.001
150	0.9930	0.003	1000	0.9980	0.001
200	0.9950	0.002	1100	0.9980	0.001
250	0.9950	0.002	1200	0.9980	0.001
300	0.9970	0.002	1300	0.9980	0.001
350	0.9970	0.002	1400	0.9980	0.001
400	0.9970	0.002	1500	0.9980	0.001
450	0.9970	0.002	1600	0.9990	0.001
500	0.9970	0.002	1700	1.0000	0.000
550	0.9970	0.002	1800	1.0000	0.000
600	0.9970	0.002	1900	1.0000	0.000
650	0.9970	0.002	2000	1.0000	0.000
700	0.9970	0.002	2100	1.0000	0.000
750	0.9970	0.002	2200	1.0000	0.000
800	0.9970	0.002	2300	1.0000	0.000
850	0.9980	0.001	2400	1.0000	0.000
900	0.9980	0.001	2500	1.0000	0.000

Table C.8: Gamma-ray self-shielding factors for the nickel foil listed in Table B.1. Error bars represent absolute standard error.
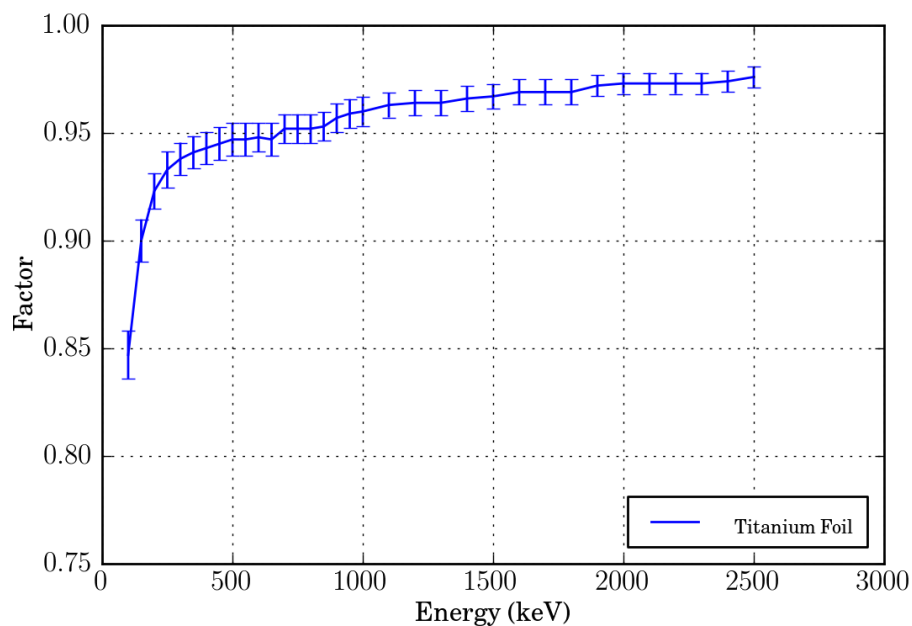
Figure C.9: Gamma-ray self-shielding factors for the titanium foil listed in Table B.1. Error bars represent absolute standard error.

Gamma-ray Energy keV	Self-Shielding Factor	MCNPX RSE	Gamma-ray Energy keV	Self-Shielding Factor	MCNPX RSE
100	0.8470	0.013	950	0.9590	0.007
150	0.9000	0.011	1000	0.9600	0.007
200	0.9230	0.009	1100	0.9630	0.006
250	0.9330	0.009	1200	0.9640	0.006
300	0.9380	0.008	1300	0.9640	0.006
350	0.9410	0.008	1400	0.9660	0.006
400	0.9430	0.008	1500	0.9670	0.006
450	0.9450	0.008	1600	0.9690	0.006
500	0.9470	0.008	1700	0.9690	0.006
550	0.9470	0.008	1800	0.9690	0.006
600	0.9480	0.007	1900	0.9720	0.005
650	0.9470	0.008	2000	0.9730	0.005
700	0.9520	0.007	2100	0.9730	0.005
750	0.9520	0.007	2200	0.9730	0.005
800	0.9520	0.007	2300	0.9730	0.005
850	0.9530	0.007	2400	0.9740	0.005
900	0.9570	0.007	2500	0.9760	0.005

Table C.9: Gamma-ray self-shielding factors for the titanium foil listed in Table B.1. Error bars represent absolute standard error.

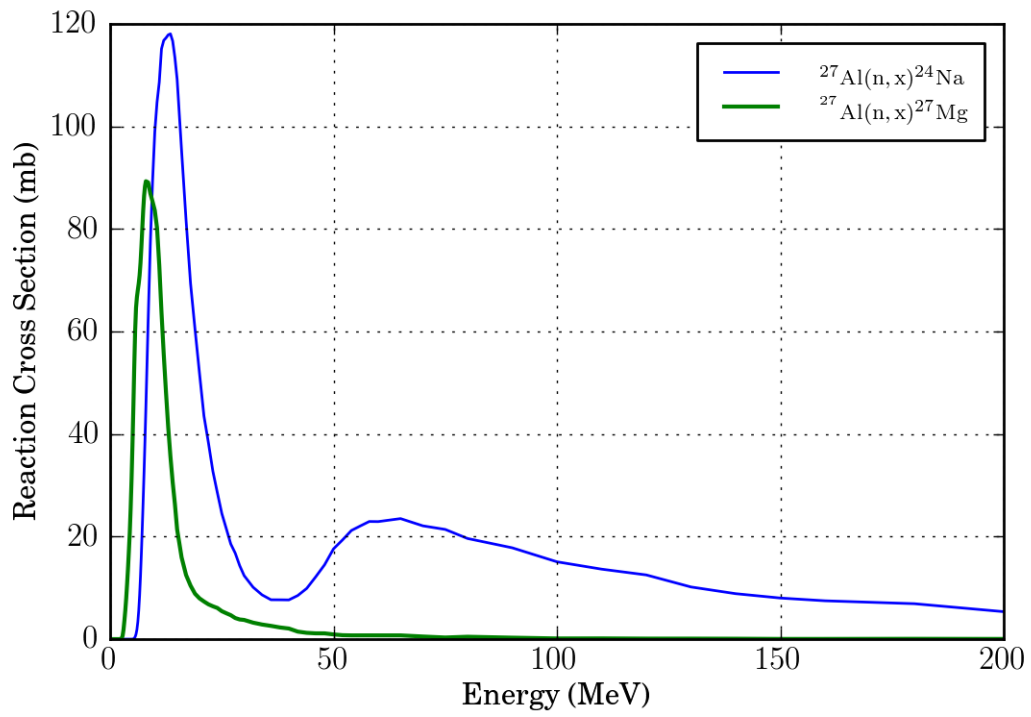# Appendix D

Reaction Cross Section Plots

Figure D.1: Threshold reaction cross sections from the TENDL-2010 library for aluminum.
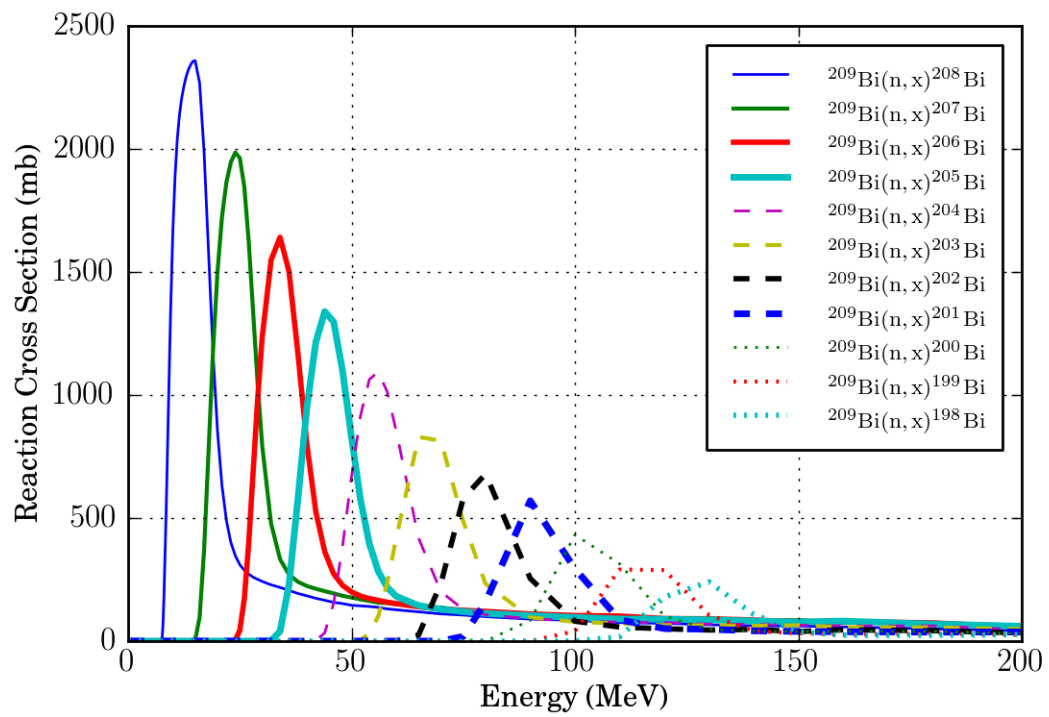
Figure D.2: Threshold reaction cross sections from the TENDL-2010 library for bismuth.
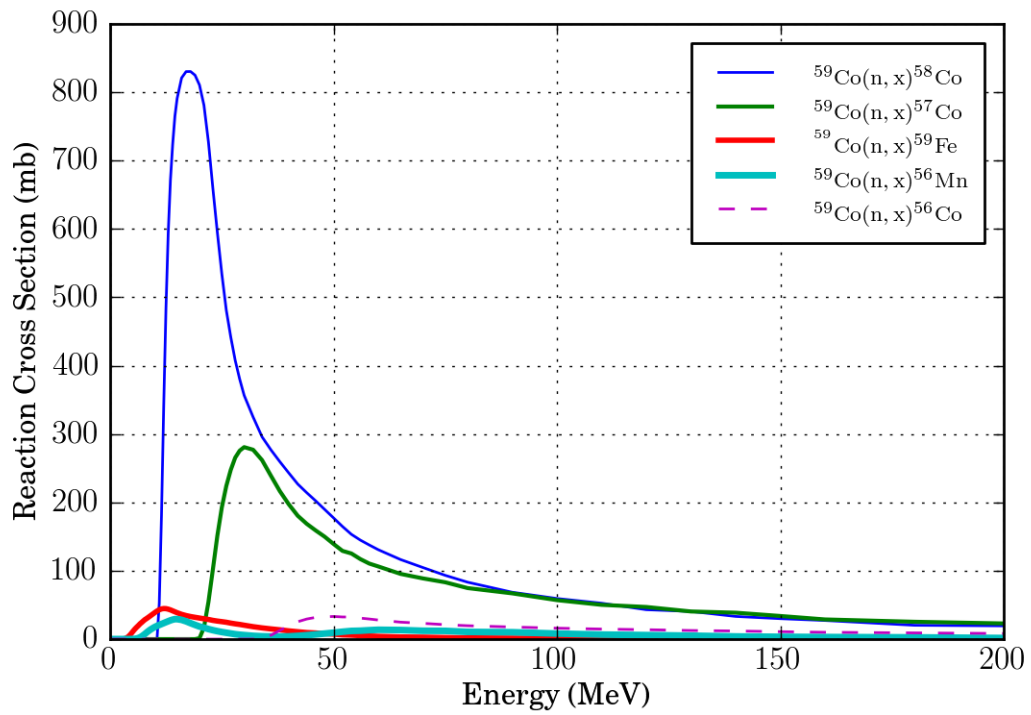
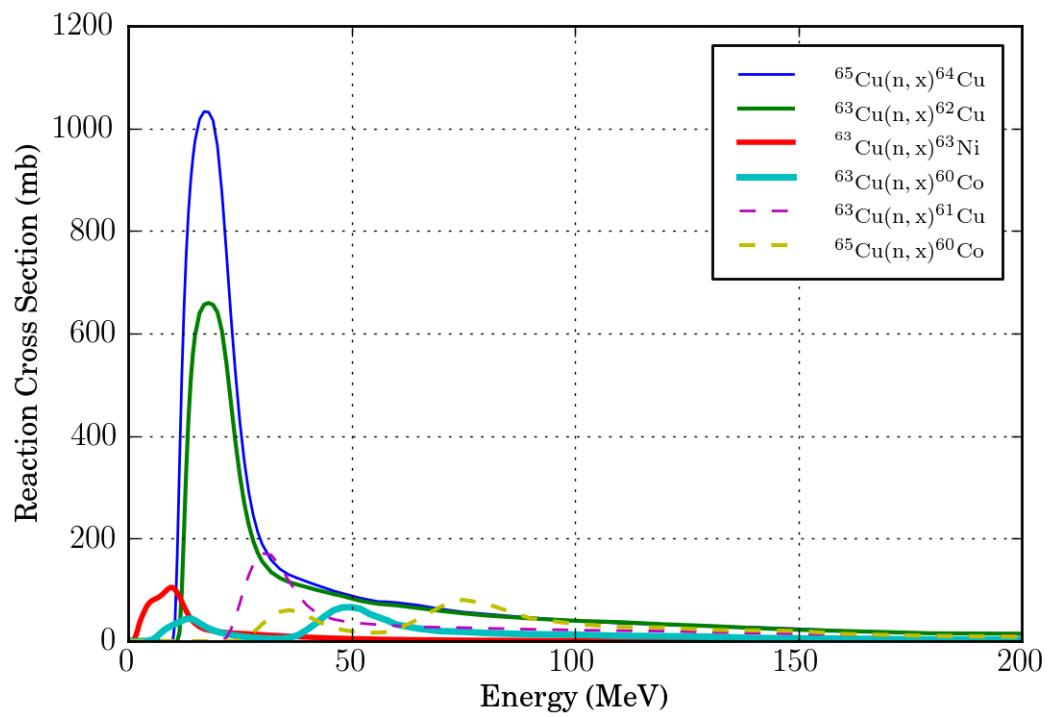Figure D.3: Threshold reaction cross sections from the TENDL-2010 library for cobalt.

Figure D.4: Threshold reaction cross sections from the TENDL-2010 library for copper.
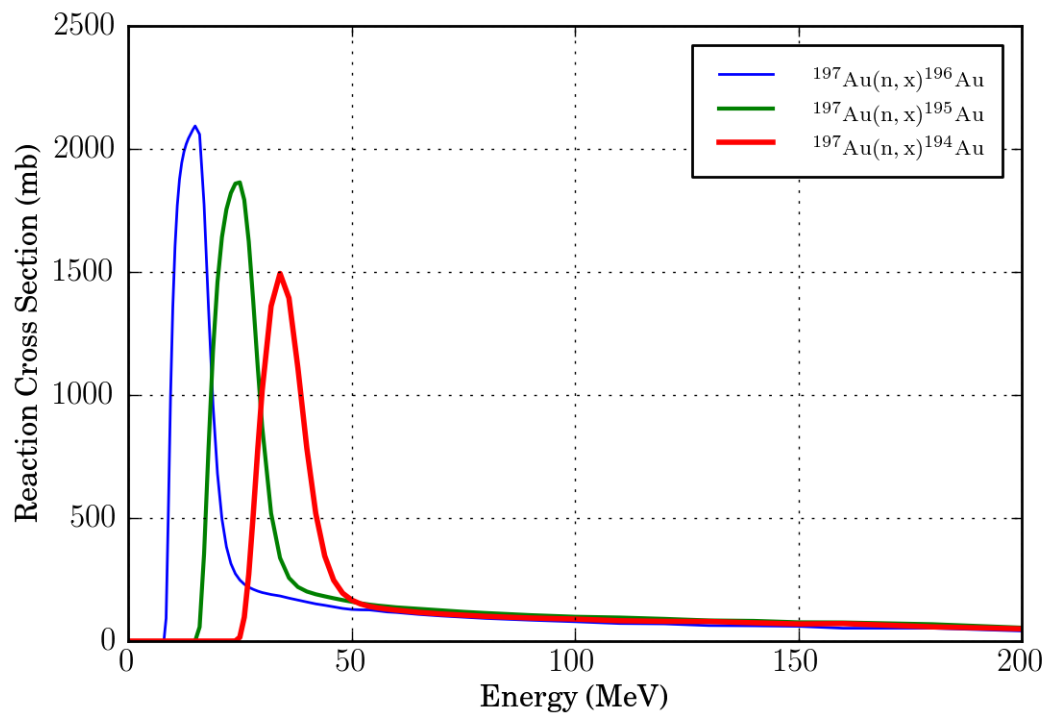
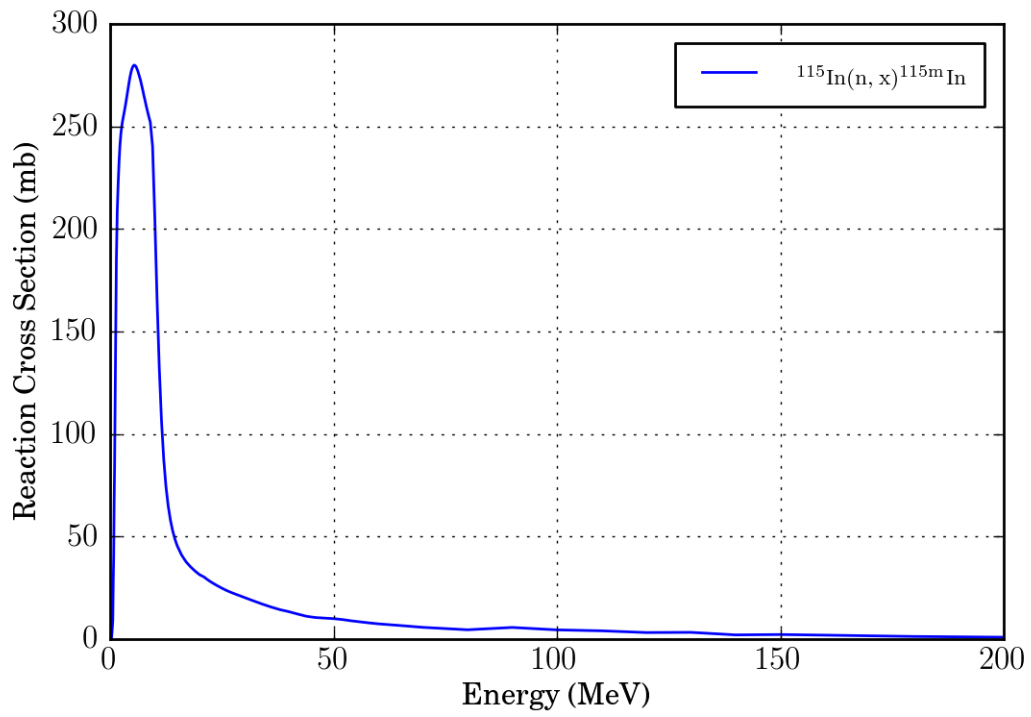Figure D.5: Threshold reaction cross sections from the TENDL-2010 library for gold.

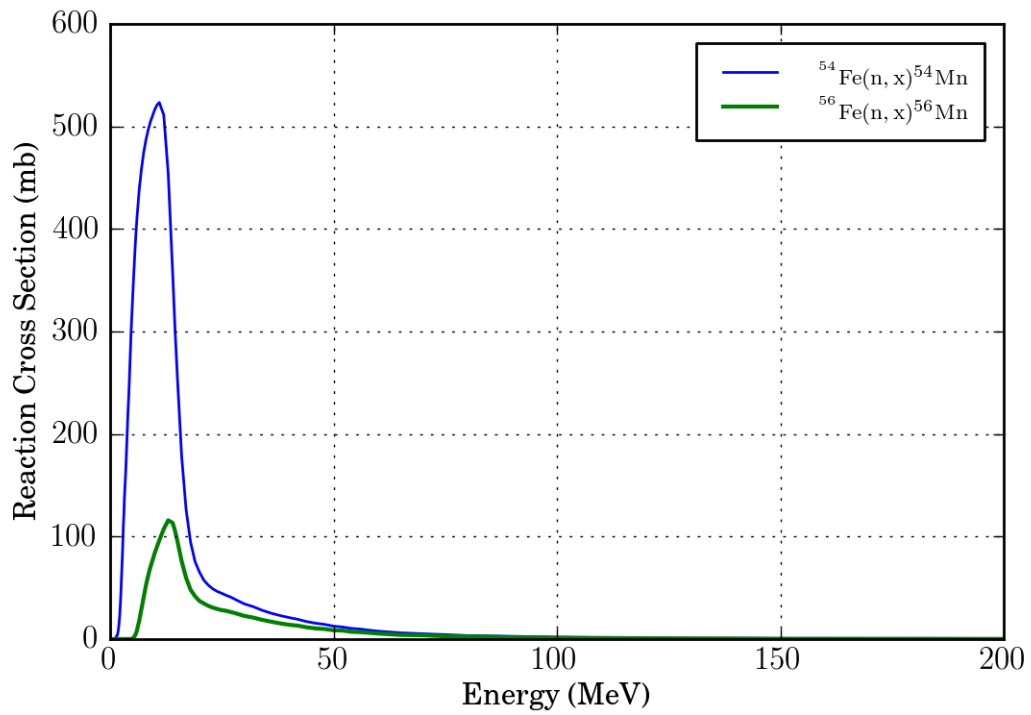Figure D.6: Threshold reaction cross sections from the TENDL-2010 library for indium.

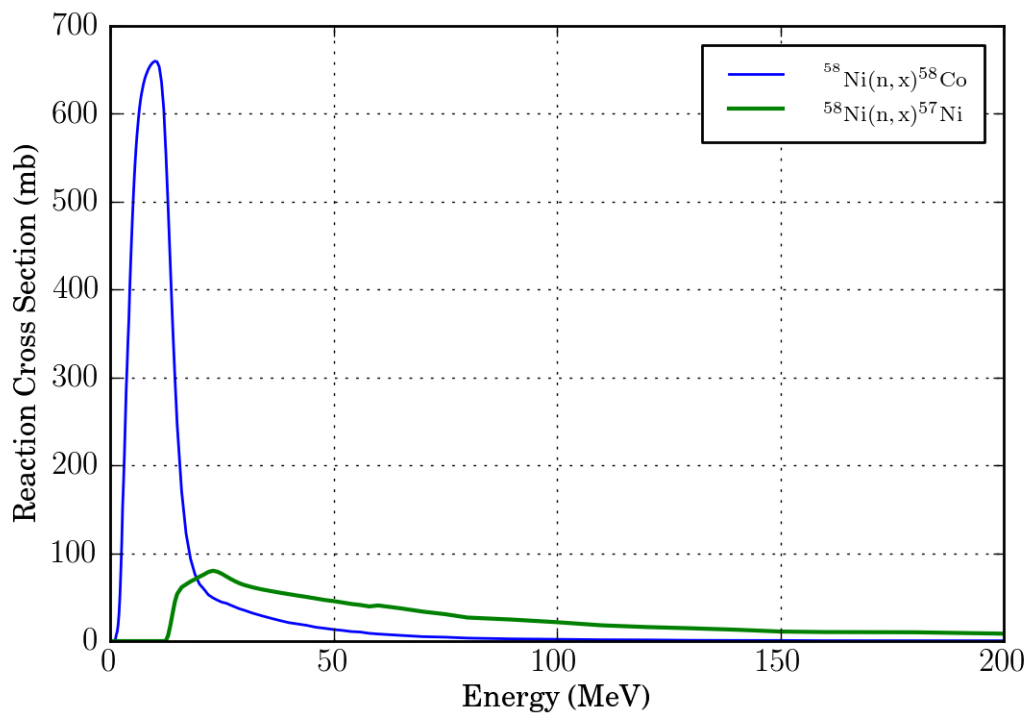Figure D.7: Threshold reaction cross sections from the TENDL-2010 library for iron.

Figure D.8: Threshold reaction cross sections from the TENDL-2010 library for nickel.
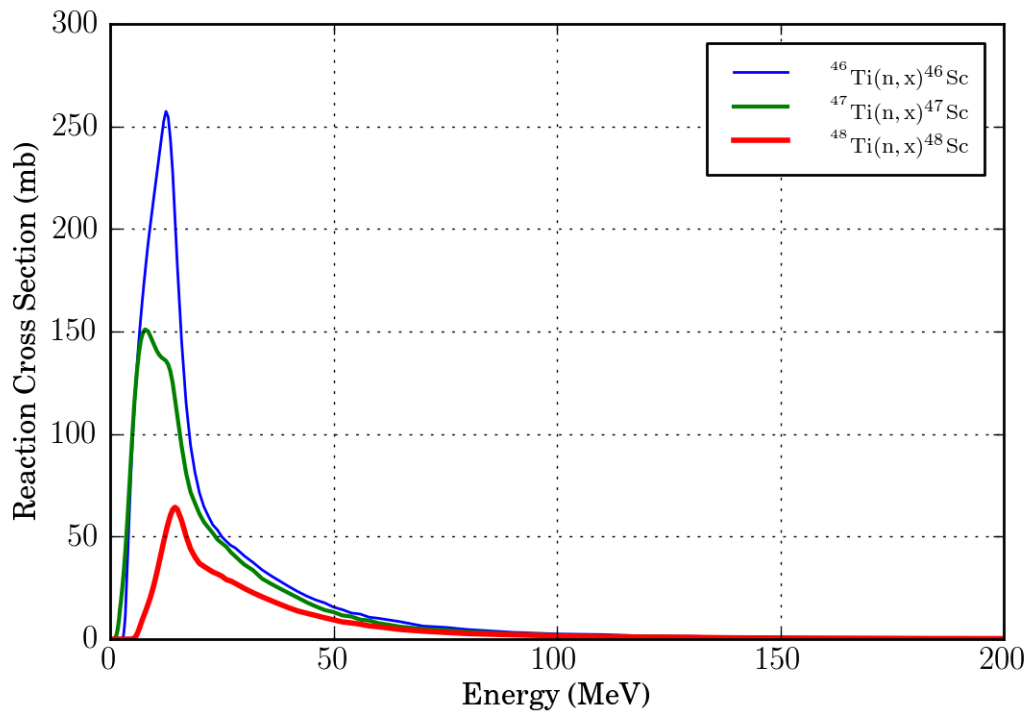
Figure D.9: Threshold reaction cross sections from the TENDL-2010 library for titanium.

Vita

Nicholas Luciano is from Englewood, Florida. His interest in nuclear engineering began when he was a student assistant at the Neely Nuclear Research Center at the Georgia Institute of Technology.

After he received his B.S. in Physics from Georgia Tech, he worked as a physics associate at the Collider-Accelerator Department at Brookhaven National Laboratory. In Brookhaven's main control room, Nick operated several particle accelerators, including the Relativistic Heavy Ion Collider and the Alternating Gradient Synchrotron, two of the world's largest hadron accelerators. It was in the main control room that he met his future fiancée, Jennifer Niedziela. He was also part of a team that built and tested a prototype hydrogen jet luminescence monitor for 100 GeV ion beam profile measurements.

In 2006, he joined the Spallation Neutron Source staff as a control room shift supervisor. While working at SNS, he assisted the ion source group in developing a new hydrogen ion extraction and transport system. Nick began taking part-time classes in nuclear engineering at the University of Tennessee, and soon after, Jennifer moved to SNS as a graduate student in physics at UT. In the fall of 2010, both Nick and Jen left their jobs at SNS to become full-time graduate students. They are engaged to be married in 2012. Nick is currently pursuing his Ph.D. in nuclear engineering at UT, and hopes to continue research after completing his degree.